IntechOpen

Calorimetry

Design, Theory and Applications in Porous Solids

Edited by Juan Carlos Moreno-Piraján

CALORIMETRY - DESIGN, THEORY AND APPLICATIONS IN POROUS SOLIDS

Edited by **Juan Carlos Moreno-Piraján**

Calorimetry - Design, Theory and Applications in Porous Solids
http://dx.doi.org/10.5772/intechopen.68244
Edited by Juan Carlos Moreno-Piraján

Contributors

Mohammad Rezwan Khan, Zhi-Cheng Tan, Liliana Giraldo, Paola Rodrigrez, Juan Carlos Moreno Piraján, Zulamita Zapata Benabithe, Poghos Vardevanyan, Armen Karapetyan

Notice

First published in London, United Kingdom, 2018 by IntechOpen
eBook (PDF) Published by IntechOpen, 2019
IntechOpen is the global imprint of INTECHOPEN LIMITED, registered in England and Wales, registration number: 11086078, The Shard, 25th floor, 32 London Bridge Street
London, SE19SG – United Kingdom
Printed in Croatia

British Library Cataloguing-in-Publication Data
A catalogue record for this book is available from the British Library

Additional hard and PDF copies can be obtained from orders@intechopen.com

Calorimetry - Design, Theory and Applications in Porous Solids
Edited by Juan Carlos Moreno-Piraján

p. cm.

Print ISBN 978-1-78923-438-1

Online ISBN 978-1-78923-439-8

eBook (PDF) ISBN 978-1-83881-294-2

Meet the editor

Juan Carlos Moreno-Piraján is a full professor in the Department of Chemistry at the Universidad de los Andes (Bogotá, Colombia) and director of the Research Group on Porous Solids and Calorimetry. He is a chemist and received his PhD in Chemistry in 1997 from the Universidad Nacional de Colombia (Bogotá, Colombia).

His research experience is within the general area of the surface chemistry of carbon with special emphasis on activated carbon, carbons for gas storage, carbon-supported catalysts, mesoporous carbons, carbon molecular sieves, aerogels, metal organic frameworks, carbon foams and slices. Professor Moreno-Piraján has also contributed to the area of instruments by designing and constructing Tian-Calvet calorimeters, which he has used in the characterization of the materials he prepares. Professor Moreno-Piraján has supervised several undergraduate and postgraduate theses and has been responsible for over 20 research projects. He has had more than 180 papers published in refereed journals and is the author of 1 book (*Thermodynamics*, Ed. Uniandes, 2005) and 7 book chapters. He has been a member of the editorial board and an associate editor of *Thermal Analysis and Calorimetry* since 2018.

Contents

Preface

When talking about calorimetry as a very important instrumental technique in thermodynamics, it is usually associated with Antoine Laurent Lavoisier, who is credited with the origin of direct and indirect calorimetry. In 1777, he published in the *Archives of the Academy of Sciences of Paris* the results of his tests on the respiration of animals, in which he showed the decrease in oxygen content of the air, the increase in carbon dioxide and the invariability of the volume of nitrogen with respiratory activity. His conclusions differed from the theory of phlogiston developed by Priestley in 1774, and also supported by Adair Crawford in 1779 as a result of the parallel investigations carried out in Scotland; however, these were more focused on the measurement of heat production of animals than on the study of the exchange of gases during respiration. A few years later, in 1780, together with the mathematician and physicist Pierre Simón de Laplace, Lavoisier published his famous *Memoire sur la chaleur*, in which he describes the adiabatic calorimeter designed by Laplace and the methods used for its calibration. The history of direct calorimetry begins with this first calorimeter.

With the passing of the decades and the development of technology, calorimetry has become more automatic, and the instruments are designed and constructed much more sensitively so that the spectrum of applications of this technique has been extended. It is therefore very common to find different types of calorimeters for diverse applications ranging from basic to applied sciences. This text presents samples in which scientists show in good detail the applications in various areas such as biochemistry, energy storage, materials development and characterization of porous solids. Calorimetry is a part of thermodynamics that is responsible for measuring the thermal effects of the processes that occur in nature. There are very varied types of processes in nature, which is why it is impossible to have a single calorimeter, so understanding the basic fundamentals of this art is necessary before addressing any measures and/or construction of a computer.

This book aims to illustrate the different applications of calorimetry in a wide spectrum of fields. Applications are presented in carbonaceous materials, and the results of the measures of the efficiency of batteries in electric vehicles through the use of isothermal calorimetry, the use of immersion calorimetry in the characterization of porous solids, the energetic characterization of the conformational transitions of DNA, and the construction of a high-precision adiabatic calorimeter and applications in functional materials are presented.

Within the development of the different chapters, the authors present various elements that are usually used as thermal sensors and their principles, as well as specific examples of applications of said technique.

Dr. Juan Carlos Moreno-Piraján
Universidad de Los Andes
Bogotá, Colombia

Chapter 1

Construction of High-Precision Adiabatic Calorimeter and Thermodynamic Study on Functional Materials

Zhi Cheng Tan, Quan Shi and Xin Liu

Additional information is available at the end of the chapter

http://dx.doi.org/10.5772/intechopen.76151

Abstract

In this chapter, a high-precision fully automated adiabatic calorimeter for heat capacity measurement of condensed materials in the temperature range from 80 to 400 K was described in detail. By using this calorimeter the heat capacity and thermodynamic properties of two kinds of function materials, ionic liquid and nanomaterials, were investigated. The heat capacities of IL [EMIM][TCB] were measured over the temperature range from 78 to 370 K by the high-precision-automated adiabatic calorimeter. Five kinds of nanostructured oxide materials, Al_2O_3, SiO_2, TiO_2, ZnO_2, ZrO_2, and two kinds of nanocrystalline metals: nickel and copper were investigated from heat capacity measurements. It is found that heat capacity enhancement in nanostructured materials is influenced by many factors, such as density, thermal expansion, sample purity, surface absorption, size effect, and so on.

Keywords: calorimetry, adiabatic calorimeter, calibration of calorimetric system, heat capacity, phase transition, thermodynamic properties, function materials

1. Introduction

Adiabatic calorimetry is one of the most important research methods in the fields of thermochemistry and thermophysics. Many results can be obtained from this method, such as, molar heat capacities over wide temperature range, standard entropy, standard thermodynamic functions; the temperature, enthalpy, entropy and mechanism of phase transition, and other important information concerned with the structure and energetics of substances, which have very significant guiding role for theoretical research and application development of various new substances or materials. But at present high-precision adiabatic calorimeter is not

available from commercial apparatus in the world. In this chapter, hence, we introduce a high-precision fully automatic adiabatic calorimeter constructed in our themochemistry laboratory, and report the thermodynamic property studies of two types of functional materials: ionic liquid and nanomaterials performed by this adiabatic calorimeter.

2. Construction of a fully automated high-precision adiabatic calorimeter used for heat capacity measurements of condensed materials in the range from 80 to 400 K

2.1. Introduction

Heat capacity is one of the fundamental thermodynamic properties of materials and is very important in many physical and chemical theoretical research programmes and engineering technology designs. Adiabatic calorimetry is the most reliable technique used to obtain heat capacity and other thermodynamic data of substances [1–9]. Research on adiabatic calorimetry has been conducted in our thermochemistry laboratory since 1960s and several adiabatic calorimetric apparatus have been constructed to obtain measurements over the temperature ranges of (4.2-90) K [10–12], (80-400) K [13–21], (70-580) K [18–19], (300-600 K) [20] and (400-700) K [22]. Traditional adiabatic calorimetric experiments have the disadvantages of complicated experimental procedures and large amounts of experimental data which needs to be treated in order to obtain high-precision heat capacity values. Therefore, we have constructed an adiabatic calorimeter which greatly simplifies experimental procedures (by using modern computerized technology together with control theory) which can be used to obtain measurements in the temperature range of (80-40) K. The design was based on our previously reported automated adiabatic calorimetric apparatuses [17, 19]. This new calorimetric instrument has the advantages of compact data acquisition and process system; advanced intellectual level resulting in the powerful processing ability of the software; better stability of measurement; and a higher reliability of data acquisition. For a long time, low temperature adiabatic calorimetry has been used to: determine the heat capacities of various condensed materials; investigate phase transitions of materials; and determine the standard thermodynamic properties of the materials.

2.2. The construction of the adiabatic calorimeter

2.2.1. The adiabatic calorimetric system

The calorimetric system includes a calorimetric cryostat, a data collection system, an adiabatic condition control system and a high vacuum pumping system. The calorimetric cryostat consists of a sample cell, inner and outer adiabatic shields and a high vacuum can. The data collection system consisted of a multi-channel data acquisition/switch unit (Agilent 34970A) [23] for electric energy collection, a 7 1/2 Digit nanovolt micro-Ohm meter (Agilent 34420A) [24] for acquisition of the temperature of the sample cell and a P4 computer equipped with a matched module and interface card GPIB (IEEE 488).The adiabatic condition control system consisted of a high-precision temperature controller (Lake Shore, Model 340) and two sets of six-junction chromel-copel (Ni-55%, Cu-45%) thermocouple piles that were installed between

the sample cell and the inner adiabatic shield and between the inner and outer adiabatic shield, respectively. The high vacuum pump system consisted of a combined rotational mechanical pump and oil diffusion pump (Edwards, Model NXK 333000). The block diagram of the adiabatic calorimetric system is shown in **Figure 1**.

2.2.2. Sample cell and adiabatic calorimetric cryostat

The sample cell (see **Figure 2A**) was made of 0.3 mm thick gold-plated copper, 20 mm long, 20 mm in diameter with inner volume of about 6 cm^3. Three sheaths were fixed at the bottom of the cell for inserting the platinum thermometer and thermocouples. Electric heating wires(insulated Karma wire of 0.12 mm in diameter, R = 120 Ω)were coiled on the outer wall of cell A small amount of silicone thermally conductive sealant (type HT916, produced by Shanghai Huitian New Chemical Material Company, Limited) was used to seal the lid to the main body of the cell. On the lid there was a section of copper capillary for pumping out the air in the cell and introducing the helium gas to promote thermal equilibrium inside the cell. The capillary was pinched off and the resultant fracture was soldered by solder to ensure the sealing of the cell.

The adiabatic calorimetric cryostat is shown in **Figure 2B**. Two sets of six-junction chromel-copel thermocouple piles were installed between the sample cell and the inner shield, and between the inner and the outer shield to detect the temperature differences between them. The junctions of the thermocouple piles were inserted in the sheath and fixed on the corresponding surfaces whose temperatures were to be measured. The detected signal of the thermal electromotive force (EMF) created by the temperature differences was fed into the temperature controller which controlled the current through the heating wires on the

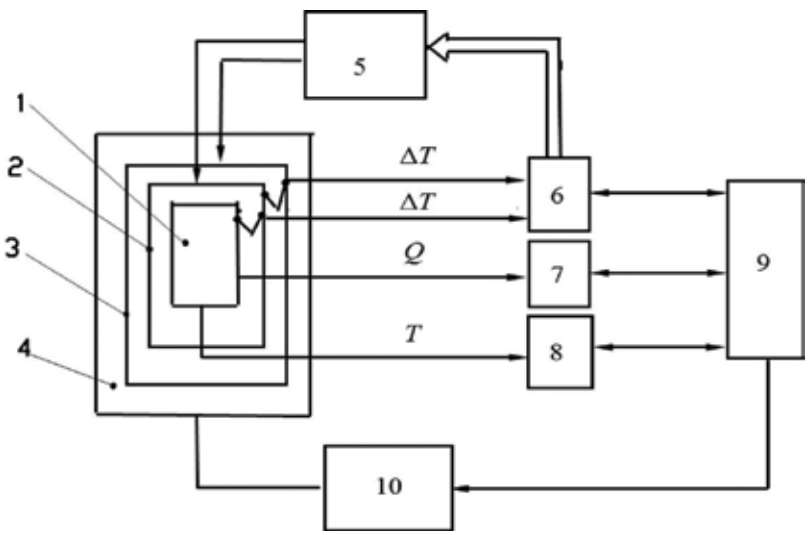

Figure 1. Block diagram of the adiabatic calorimetric system. 1, sample cell; 2, inner adiabatic shield; 3, outer adiabatic shield; 4, vacuum can; 5, silicon controlled regulator; 6, temperature controller (Lake shore 340); 7, data acquisition/switch unit (Agilent 34970A); 8, 71/2 digit nanovolt/micro-Ohm meter (Agilent 34420A); 9, computer; 10, combined rotational mechanical pump and oil diffusion pump (Edwards, model—NXK333000).

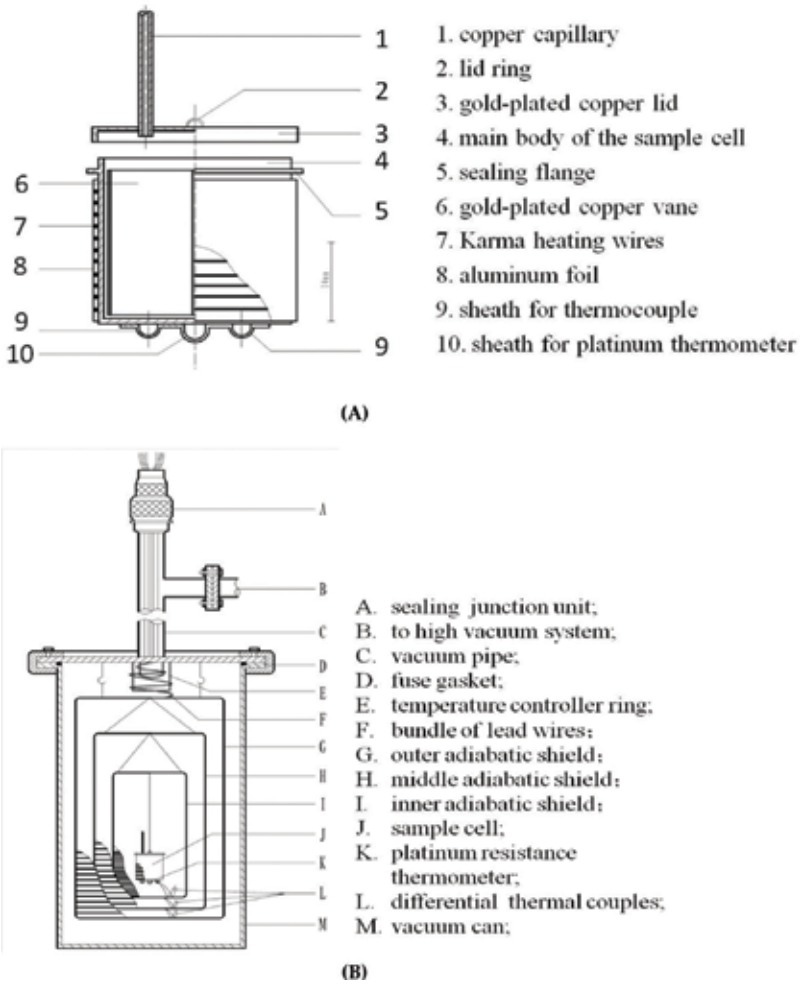

Figure 2. (A) Schematic diagram of sample cell of the adiabatic calorimeter. (B) Schematic diagram of main body of the adiabatic calorimeter.

inner and outer adiabatic shields, This heating was used to minimize the temperature difference between the sample cell and the shields thus maintaining a good adiabatic environment.

The sample cell and the adiabatic shields were placed in the high vacuum can to eliminate the heat loss of the cell caused by convection heat transfer. During the heat capacity measurements the vacuum can was evacuated to (10^{-3}~10^{-4}) Pa by the rotational and diffusion pump.

A precision miniature platinum resistance thermometer (produced by Shanghai Institute of Industrial Automatic Meters, 16 mm long, 1.6 mm in diameter) measured the temperature of the sample cell. The resistance of the thermometer was measured by the 7 1/2 Digit nanovolt/micro-Ohm meter (Agilent 34420A) with four-terminal resistance measurement circuit, and then inputted into the computer for processing after A/D conversion. Then the corresponding temperature was calculated according to the relationship between the resistance

and temperature of the thermometer, which was calibrated in terms of ITS-90 by Station of Low-Temperature Metrology and Measurements, Chinese Academy of Sciences. Here R_0 = 100.1384 Ω.

2.2.3. Computer, data collection unit and software

The data acquisition system used a P4 computer with Windows Operation System (OS), which had fast computing power and a parallel processing function. The computer collected and controlled data information through GPIB (IEEE 488) card with PCI interface. The interface card (Agilent 82350A) was used in the data exchange because this card has a transmitting speed of 750 kBs^{-1}, (here B refers to bytes) which guarantees the information exchanging speed during the experimental process of adiabatic control, collection and control of electrical heating and collection of sample temperatures. The software was programmed to run functions at designated times.

The A/D conversion of all the collected data was done by the data acquisition/switch unit (Agilent 34970A) [23] and 7 1/2 digit nanovolt/micro-Ohm meter, (Agilent 34420A) [24]. The Agilent 34970A had a high precision of data conversion and stability, and had a resolution of 100 nV at 100 mV measuring range, which varies within ±0.0090% over a year. Over the measuring range of our experiments, the resolution of the resistance measurement was 1 mΩ with a variation of ±0.0140%, thus guaranteeing the high precision of data collection. The Agilent 34,420 A nanovolt/ micro-ohm meter was a high-sensitivity multimeter optimized for performing low-level measurements. It combined low-noise voltage measurements with resistance and temperature functions, setting a new standard in low-level flexibility and performance. It has 7 1/2 digits resolution and 100 pV/100 nΩ sensitivity (equivalent to the temperature resolution of 2.5×10^{-5} K for the platinum thermometer with R_0 = 100 Ω).

The software of the system consisted mainly of three modules (**Figure 3**): data collection and control module, adiabatic environment control module and the module for the setting and revision of the experimental conditions and the data displaying.

The heat capacity measurement was done using an intermittent direct heating method, i.e., loading a certain number of moles (m) of sample in the sample cell of the calorimeter followed

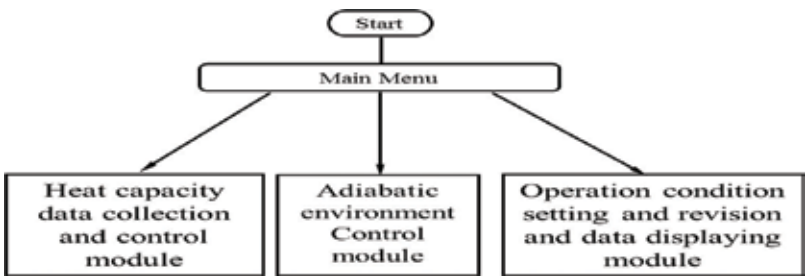

Figure 3. The block diagram of the software for calorimetric measurements programmed by computer.

by the input of an appropriate amount of electric energy (Q) to induce a temperature rise of the cell (ΔT). From the measured values Q and ΔT the heat capacity of the sample cell (C_p) was determined:

$$C_p = \frac{Q}{m \cdot \Delta T} \tag{1}$$

where

$$Q = IV\tau \tag{2}$$

and I, V and τ are current, voltage and duration of heating, respectively.

Accordingly, the heat capacity measurement was made as follows. First the temperature of the sample cell was kept stable under strict adiabatic conditions for a time which is called the temperature equilibrium period. During this period the temperature inside the sample cell was kept in equilibrium by the excellent thermal conductivity of the helium gas which fills the cell and two radial copper vanes fixed to the cell. When the temperature of the sample cell reached equilibrium, the computer system controlled (34970A) the input of an appropriate amount of current I and voltage V used to heat the sample cell to induce a temperature rise of ΔT. The computer system reads the I and V data at intervals (e.g., 30 s) during the heating process. The computer controlled the heating duration and calculated Q from Eq. (2). Following the heating period, the temperature T of sample cell was measured at the next temperature equilibrium period. The temperature increment of the sample cell, ΔT, caused by the energy input was calculated on the basis of the difference in temperatures between the neighboring two equilibrium periods. The heat capacity, C_p, was then obtained from Eq. (1). Through repetitions of the above procedures the heat capacity from low temperature to high temperature could be calculated. In order to ensure adequate precision of heat capacity measurements, some problems had to be solved, such as: the determination of the beginning of the equilibrium temperature during the thermal equilibrium period; the precise measurement of the equilibrium temperature of the sample cell; and the temperature correction resulted from the heat exchange between the sample cell and its environment under non-ideal adiabatic conditions.

Following the heating period, the temperature of the sample cell continued to change as a result of the uneven distribution of the temperature of the sample cell caused by the continuous transferring of heat energy and the heat exchange between the sample cell and its environment owing to the non-ideal adiabatic conditions. After some time, however, the temperature variation of the sample cell due to the transferring of heat energy decreased while the heat exchange between the sample cell and its environment continued. Under the condition that the temperatures of the inner and outer shields were keep stable, the heat exchange between the sample cell and its environment become stable and thus there was a linear relationship between the temperature of sample cell and the time of the experimental measurement. According to this principle, the computer fitted several collected temperature points of the sample cell versus time to get the lines l_i or l_{i+1} (see **Figure 4**), whose slope was the variance ratio of the temperature as a function of time. The temperature of the calorimetric system can be regarded as reaching equilibrium if the variance ratio become small enough, e.g., 0.001 K min^{-1}, where min refers to minutes.

http://dx.doi.org/10.5772/intechopen.76151

On the other hand, except for the temperature variation, the deviation of the data collection also influences the slope of the line. The effect can be evaluated from the correlation coefficient of the fitted line. The closer the correlation coefficient is to 1, and the more the temperature points are focused around the line, the smaller will be the data collection random error. The present system took the average of the absolute values of the differences between the measured values and the fitted values as the estimation criterion. When the average value was less than some value, e.g., 0.001 K, the random error of the data collection could be neglected.

The collected temperature data were processed automatically by the computer to determine the arrival of temperature equilibrium; when the above two criteria were satisfied the computer deemed that the temperature of the calorimeter had reached equilibrium. Otherwise the temperature measurement time would be prolonged and another temperature point would be collected and the last ten temperature points would be processed with the same method as mentioned above until the two criteria were met.

The precision of the temperature measurement of sample cell correlated with the random error of the temperature data collection. To avoid this kind of error, the system collected a number (e.g., 10) of temperature points after the temperature of sample cell reached equilibrium, ranking them according to the magnitude of the collected values, discarding the maximum and minimum values among them and correcting the error by the figure filter technique:

$$\overline{T} = \frac{1}{K}\sum_{i=1}^{n-2} T_i \tag{3}$$

in which $\overline{T}$ is the corrected temperature value, $K = n-2$, T_i is the collected temperature value, n is the times of the temperature data collection after the temperature equilibrium. The corrected temperatures are shown on l_i and l_{i+1} (see **Figure 4**).

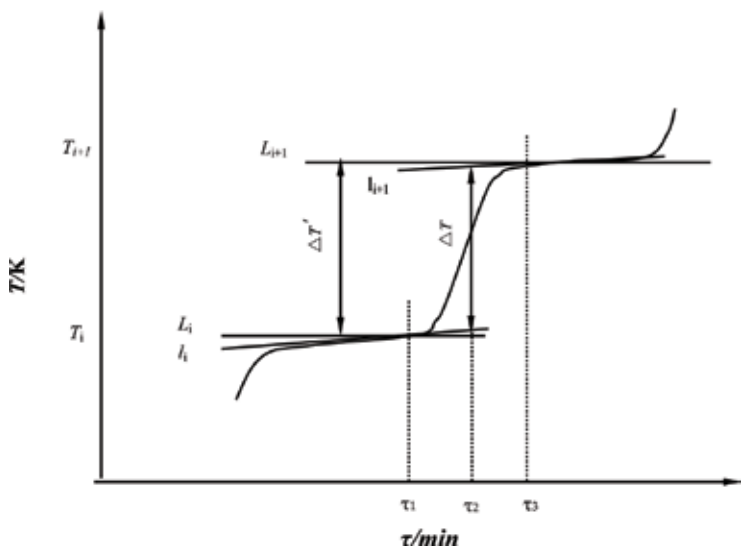

Figure 4. The principle diagram of the temperature rise correction.

The temperature rise during the heating period is the result of a combination of the heating of the sample cell by the introduced energy and the heat exchange between the sample cell and its environment caused by the non-ideal adiabatic condition; the latter will lead to some error in the measurement results. In order to correct this error, lines li and li + 1 are extrapolated to intersect with the vertical line of the time axis at the middle point between the beginning and the end of the heating time] (**Figure 4**, $\tau_2 = (\tau_1 + \tau_3)/2$). The distance between the two crossing points is the corrected temperature rise, ΔT, which is just the temperature rise caused by the heat energy introduced during the heating period. This correction is performed through extending lines l_i and $l_{i+1,}$ which are obtained when determining the start of the equilibrium temperature.

Introducing ΔT into Eq. (1) produces, $C_{p,}$ which is the heat capacity value at the temperature of (Ti + Ti$_{+1}$)/2 (see **Figure 4**). The processing procedures are shown in **Figure 5**.

2.2.4. Adiabatic environment control module

The premise of good adiabatic conditions is to keep the temperatures of the inner and outer adiabatic shields close to that of the sample cell. In order to do this the heating current introduced into the sample cell is gradually and smoothly increased in the initial period, keeping it at a constant value in the middle period and then decreasing it in the final period. If the temperatures of the inner and outer adiabatic shields are kept increasing synchronously with that of the sample cell, the temperature of sample cell will decrease after the heating period and the speed of the temperature decrease will vary with the species, mass, heat conductivity of the samples and the temperature range of the measurement because of the uneven distribution of the interior temperature of the cell during the heating period. As a result the temperature of the inner shield will become higher than that of the sample cell; this will influence the calculated heat capacity. This system can be considered as an intelligent control of the temperatures of the inner and outer adiabatic shields, that is, it corrects the heating current of the inner adiabatic shield during the latter heating period according to the thermal properties of the sample and the actual condition of the measurement in the corresponding temperature range and controls the temperature of the inner shield at a slightly lower temperature than that of the sample cell to avoid the over regulation of temperature of the inner adiabatic shield, especially for samples with small heat conductivities or samples with phase transitions.

2.2.5. The module of setting and revision of operation conditions and data displaying

This system refreshes the screen every time it collects data, displaying in real time the various parameters and states, such as, the electric energy introduced into the sample cell, the temperature of the sample cell, the adiabatic control condition and the environment temperature.

The measuring conditions can be set on the screen before the measurement and revised on the screen during the measurement. At the same time information can be displayed, such as, the heat capacity of the sample which might vary with the temperature and the occurrence of a phase transition, so as to understand the change of thermal properties of the sample at anytime. The parameters and states mentioned above can be displayed on the screen at the same time and can be processed because the software of the system is developed under a multi-file application program with a multi-channel module.

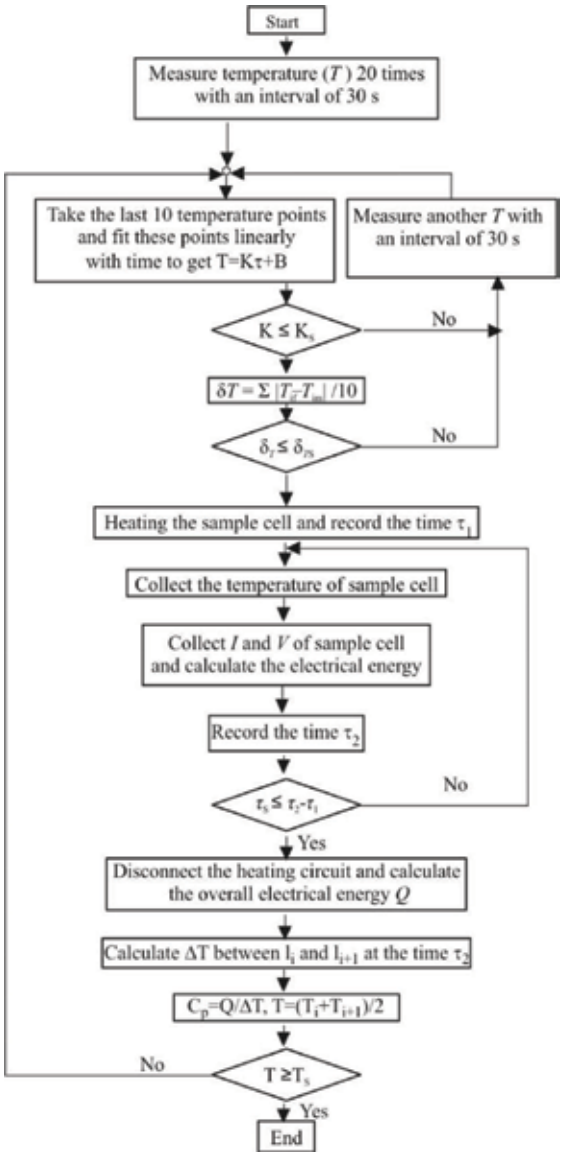

Figure 5. Block diagram of acquisition and processing for heat-capacity data controlled by computer.

2.3. Calibration of the calorimeter and discussion of results

The reliability of the constructed adiabatic calorimetric system was verified by measuring the molar heat capacities of synthetic sapphire (α-Al_2O_3, Standard Reference Material 720).The results are listed in **Table 1**. In order to compare the values with those recommended by NIST [25], we calculated the molar heat capacities of α-Al_2O_3 in the temperature range of (80–400) K at intervals of 10 K using a non-linear insert method based on the measured molar heat capacity data. The results are listed in **Table 2** and shown in **Figure 6**, from which it can be seen that

the deviations of our values from the recommended values are within ± 0.1%, which indicates that the performance of the constructed calorimetric apparatus has been improved compared with previous calorimeters.

Compared with the previous calorimetric system, the newly improved system has the advantages of: compaction; is a simplified device, exhibits great stability and precision; and operates at a higher intellectual level with greater software power than previous reported calorimeters. After operating and testing the equipment for one and a half years we can confirm that the calorimetric system is: easy to operate; performs in a stable manner; and is able to perform

T (K)	C_p (J K^{-1} mol^{-1})	T (K)	C_p (J K^{-1}mol^{-1})	T (K)	C_p (J K^{-1}mol^{-1})
78.636	6.377	159.716	35.898	280.221	74.988
79.621	6.725	163.370	37.371	283.636	76.003
80.914	7.105	166.940	38.836	286.970	76.623
82.612	7.649	170.434	40.202	289.848	77.225
84.261	8.043	173.857	41.462	292.652	78.015
85.868	8.526	177.215	42.745	295.379	78.494
87.435	9.002	180.512	43.985	298.106	79.019
88.968	9.467	183.752	45.191	301.288	79.646
90.466	9.920	186.939	46.442	304.545	80.502
91.933	10.366	190.075	47.587	307.229	80.953
93.370	10.812	193.163	48.720	309.918	81.498
94.780	11.264	196.591	49.964	312.585	82.032
96.163	11.722	200.349	51.294	315.238	82.527
97.522	12.178	204.043	52.561	317.878	83.033
98.858	12.627	207.679	53.872	320.502	83.476
100.171	13.065	211.258	55.055	323.493	84.108
101.464	13.501	214.781	56.284	326.855	84.726
102.736	13.952	221.677	58.482	330.201	85.325
103.990	14.438	225.053	59.618	333.529	86.152
106.588	15.363	228.384	60.716	336.818	86.670
110.464	16.756	231.671	61.722	340.706	87.329
114.184	18.093	234.923	62.690	345.119	88.148
119.983	20.085	238.140	63.684	349.510	88.825
120.933	20.668	241.288	64.568	353.864	89.563
123.067	21.594	244.470	65.503	358.182	90.249
126.341	22.851	247.582	66.492	362.435	90.734
129.520	24.083	250.679	67.275	366.655	91.608

T (K)	C_p (J K^{-1} mol^{-1})	T (K)	C_p (J K^{-1}mol^{-1})	T (K)	C_p (J K^{-1}mol^{-1})
132.614	25.297	253.746	68.197	370.843	92.381
135.628	26.489	256.786	69.051	374.999	93.160
138.569	27.649	259.773	69.865	378.887	93.546
141.441	28.771	262.804	70.671	383.002	94.013
144.251	29.854	265.768	71.443	387.425	94.611
147.308	31.010	268.706	72.194	391.816	95.131
149.304	32.036	271.620	72.936	396.207	95.735
152.497	33.269	274.509	73.667	400.363	96.183
155.971	34.693	277.377	74.360		

Table 1. Experimental molar heat capacities ofα-Al_2O_3 (M = 101.96 g.Mol^{-1}).

T (K)	C_p (Fit) (J K^{-1} mol^{-1})	C_p (NIST) (J K^{-1} mol^{-1})	δ* (%)	T (K)	C_p (Fit) (J K^{-1} mol^{-1})	C_p (NIST) (J K^{-1} mol^{-1})	δ* (%)
80	6.901	6.90	0.01	250	67.08	67.06	0.03
90	9.678	9.67	0.08	260	69.82	69.80	0.03
100	12.85	12.84	0.08	270	72.42	72.41	0.01
110	16.34	16.34	0.00	280	74.87	74.88	−0.01
120	20.07	20.07	0.00	290	77.20	77.23	−0.04
130	23.95	23.95	0.00	300	79.41	79.45	−0.05
140	27.93	27.93	0.00	310	81.51	81.56	−0.06
150	31.95	31.94	0.03	320	83.49	83.55	−0.07
160	35.95	35.94	0.03	330	85.37	85.44	−0.08
170	39.90	39.89	0.03	340	87.16	87.23	−0.08
180	43.75	43.74	0.02	350	88.84	88.92	−0.09
190	47.50	47.50	0.00	360	90.45	90.52	−0.08
200	51.12	51.12	0.00	370	91.97	92.04	−0.08
210	54.61	54.61	0.00	380	93.41	93.48	−0.07
220	57.95	57.95	0.00	390	94.91	94.84	0.07
230	61.14	61.14	0.00	400	96.18	96.14	0.04
240	64.18	64.17	0.02				

Table 2. Comparison of experimental molar heat capacities of α-Al_2O_3 with the recommended values by NIST, *δ = 100·(C_p (Fit) - C_p (NIST))/C_p (NIST). δ is the deviation of the fit value of the experimental molar heat capacities from the recommended values by NIST.

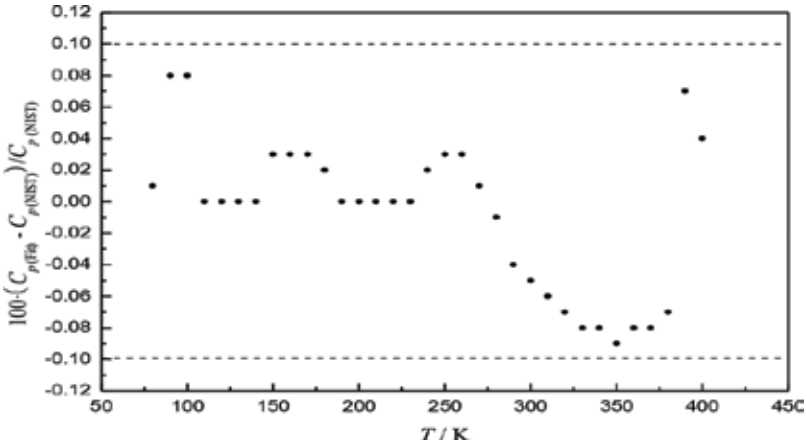

Figure 6. Plot of deviations 100·(C_p (fit) - C_p (NIST)))/C_p (NIST) of our results for the molar heat capacities ofα-Al_2O_3 from the recommended values by NIST, where C_p (fit) denotes the fit value of our experimental molar heat capacities, C_p (NIST) denotes the recommended values by NIST.

with complete automatic control which includes data processing. All the controlling and measuring procedures can be accomplished through the computer after the sample is loaded in the calorimeter cell. The calorimetric apparatus is now being commercially manufactured.

3. Thermodynamic study on functional materials by adiabatic colorimeter

3.1. Heat capacity and thermodynamic properties of novel ionic liquid 1-ethyl-3-methylimidazolium tetracyanoborate [EMIM] [TCB]

3.1.1. Introduction

During the past decade ionic liquids (ILs) have attracted increasing attention for several reasons. The most striking property is their very low vapor pressure, which suggests their applications as ideal solvents to replace conventional solvents in the frame of "green chemistry." Their highly polar character opens new ways for chemical reactions in homogeneous as well as in biphasic catalyst systems. Special selective solubility for particular components in fluid mixtures give them the potential for use in separation processes. Moreover, properties such as high inherent conductivities, good thermal stability and liquidity over a wide temperature range, opens the way for ILs to be considered as lubricants, thermofluids, plasticizer and electrically conductive liquids in electrochemistry [26] However, the focus by many scientists has been on synthetic, applications in organic chemistry, electrochemistry, and in catalysis, [27–33] while few researchers have worked on the fundamental thermodynamic properties of ILs [26], [34–41] We believe that this has limited the development of using ILs in industry and in the laboratory, and has led us to systematically investigate the thermodynamic properties of ILs.

The novel ionic liquid 1-ethyl-3-methylimidazolium tetracyanoborate ([EMIM] [TCB]) has one of the lowest reported viscosities among ILs. In response to the need for stable hydrophobic ionic liquids, as well as the continuing search for novel materials with technically-relevant properties, Merck KGaA has pursued the development of ionic liquid systems based on the tetracyanoborate (TCB) [42] and tris(pentafluoroethyl)trifluorophosphate (FAP) [43] anions. The resultant IL, [EMIM] [TCB], combines high electrochemical stability with low viscosity; thus providing an ideal ionic liquid for various kinds of electrochemical applications, especially in electrolyte formulations. In addition, its polar nature enables the selective extraction of small polar molecules from aqueous media, like butanol from a fermentation broth.31 Although the novel ionic liquid is very useful in many fields, some of its basic thermodynamic properties are unknown. [34]. As a continuation of our series of research on thermodynamic properties of ionic liquids [34, 38] we have investigated the thermodynamic properties of [EMIM][TCB] including the heat capacity, melting temperature, entropy and enthalpy of fusion, and thermostability by adiabatic calorimetry (AC) and thermogravimetric analytic technique (TG-DTG).

3.1.2. Material of the ionic liquid sample and TG analysis

The ionic liquid, 1-ethyl-3-methylimidazolium tetracyanoborate [$C_{10}H_{11}BN_6$, CAS No. 742099–80-5] was donated by Merck KGaA with labeled purity of 99.9% mass fraction and batch No.S5202031. The clear, colorless, adhesive, liquid sample was transported by an injector and dried under vacuum for 1 day at T = 343 K before the calorimetric measurements were made. The structural formula of the sample is shown in **Figure 7**.

The thermogravimetric (TG) measurements of the sample were carried out by a Thermogravimetric analyzer (Model: Setaram setsys 16/18, SETARAM, France) under high purity argon with a flow rate of 85 ml·min^{-1} at the heating rate of 10 K·min^{-1} from 300 to 1000 K. The sample mass of 45.65 mg was filled into alumina crucible with cover.

From the TG-DTG curve in **Figure 8**, it can be seen that the mass loss of the sample was completed in a single step. The [EMIM][TCB] sample was stable below 570 K. It begins to lose weight at 592.83 K, reaching a maximum rate of weight loss at 677.72 K and completely lost its weight when the temperature reached 791.03 K.

3.1.3. Heat capacity measurements

The heat capacity measurements were carried out in the high-precision automated adiabatic calorimeter mentioned above. The [EMIM] [TCB] sample mass used for the heat capacity measurement was 4.08282 g, which is equivalent to 18.062 mmol based on its molar mass of 226.047 g·mol^{-1}.

Experimental molar heat capacities of [EMIM][TCB] measured by the adiabatic calorimeter over the temperature range from 78 to 370 K are listed in **Table 3** and plotted in **Figure 9**. From the Figure, a phase transition was observed at the peak temperature of 283.123 K. According to its reported melting point 286.15 K (MerkK GaA, MSDS) this transition corresponds to a solid–liquid phase change.

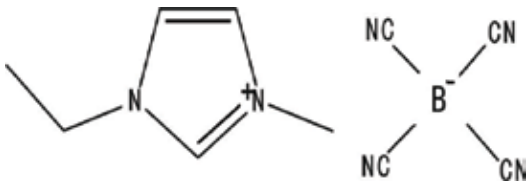

Figure 7. Structural formula of 1-ethyl-3-methylimidazolium tetracyanoborate ([EMIM] [TCB]) ionic liquid.

The values of experimental heat capacities were fitted to the following polynomial equations using least square method: [44–45]. For the solid phase over the temperature range 78 to 275 K:

$$C^0_{p,m}/\mathrm{J\cdot K^{-1}\cdot mol^{-1}} = 239.740 + 111.820\,x + 58.242\,x^2 - 65.454\,x^3 - 146.940\,x^4 + 88.433\,x^5 + 133.050\,x^6 \quad (4)$$

where x is the reduced temperature x = [T – (T max + T min) / 2] / [(T max – T min) / 2], T is the experimental temperature, thus, in the solid state (78 to 275 K), x = [(T / K) – 176.5] / 98.5, T max is the upper limit (275 K) and T min is the lower limit (78 K) of the above temperature region. The correlation coefficient of the fitting $R^2 = 0.9984$.

For the liquid phase in the temperature range from 285 to 370 K:

$$C^0_{p,m_l}\ \mathrm{J\cdot K^{-1}\cdot mol^{-1}} = 417.200 + 10.749\,x + 6.957\,x^2 - 0.848\,x^3 - 12.377\,x^4 + 0.277\,x^5 + 13.870\,x^6 \quad (5)$$

where x is the reduced temperature, x = [(T/K) − 327.5]/42.5, T is the experimental temperature, 327.5 was obtained from polynomial $(T_{max} + T_{min})/2$, and the 42.5 was obtained from the polynomial $(T_{max} - T_{min})/2$. Tmax and Tmin are the upper (370 K) and lower (285 K) limit temperature respectively. The correlation coefficient of the fitting $R^2 = 0.9872$.

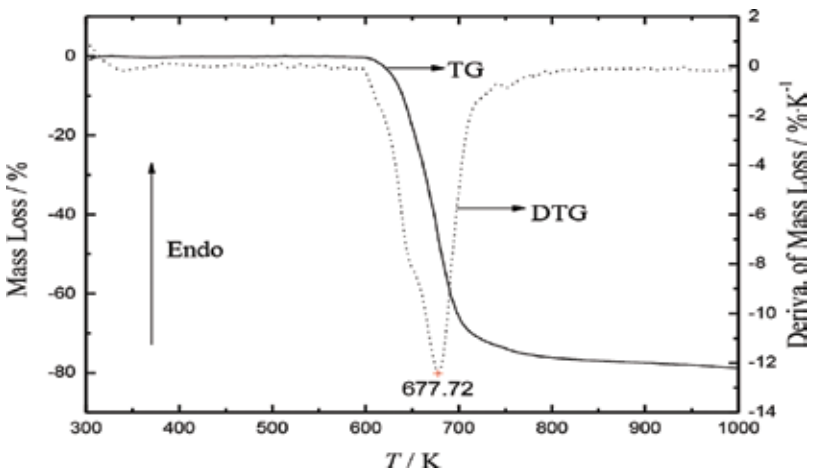

Figure 8. TG-DTG curve of [EMIM][TCB] under high purity argon.

T /K	$C_{p,m}^0$ /J·K^{-1}·mol^{-111}	T/K	$C_{p,m}^0$ /J·K^{-1}·mol^{-1}	T/K	$C_{p,m}^0$ /J·K^{-1}·mol^{-1}
Series 1 (from 78 to 370 K)					
77.927	146.085	177.977	241.097	277.4682	555.844
79.764	148.203	179.839	243.870	279.087	767.118
81.937	150.983	181.735	246.025	280.419	1202.296
83.884	152.847	183.669	246.969	281.389	1903.955
85.792	155.052	185.587	249.368	281.965	3018.912
87.718	157.914	187.499	252.239	282.399	5399.792
89.635	159.949	189.397	254.425	282.734	5575.762
91.542	161.869	191.284	256.181	282.874	7564.957
93.467	163.909	193.154	258.871	283.092	18761.467
95.387	165.461	195.014	260.989	283.252	7044.798
97.295	167.908	196.902	263.212	284.307	591.611
99.207	169.054	198.825	265.888	286.576	415.399
101.872	171.515	200.738	268.572	287.845	411.977
104.544	175.164	203.085	270.781	290.772	411.977
106.458	176.259	205.410	273.551	293.390	412.401
108.385	178.515	207.274	275.657	295.463	412.949
110.292	180.116	209.130	278.699	297.539	411.530
112.211	181.765	211.039	280.437	299.615	412.321
114.147	183.947	213.004	282.428	301.688	412.158
116.064	184.777	214.959	284.195	303.756	412.836
117.953	186.418	216.904	286.319	305.827	412.703
119.862	189.272	218.842	288.634	307.894	412.786
121.790	190.890	220.770	290.950	309.958	413.649
123.696	192.142	222.689	293.965	312.022	414.143
125.580	194.343	224.603	296.706	314.083	414.797
127.486	195.460	226.505	298.783	316.143	415.195
129.403	197.570	228.393	302.507	318.200	415.380
131.309	199.620	230.268	305.150	320.255	415.469
133.195	200.338	232.182	307.864	322.307	416.111
135.096	202.129	234.157	309.324	324.357	417.116
137.021	203.775	236.133	311.267	326.407	416.497
138.924	205.730	238.103	313.130	328.452	416.062
140.817	206.818	240.060	316.506	330.493	417.738

T /K	$C_{p,m}^{0}$ /J·K^{-1}·mol^{-111}	*T*/K	$C_{p,m}^{0}$ /J·K^{-1}·mol^{-1}	*T*/K	$C_{p,m}^{0}$ /J·K^{-1}·mol^{-1}
142.689	208.471	242.369	317.531	332.537	418.451
144.581	211.013	244.629	319.621	334.575	418.810
146.497	212.679	246.494	321.418	336.611	420.356
148.391	213.957	248.351	323.883	338.648	421.073
150.275	215.662	250.275	327.124	340.680	422.044
152.701	217.712	252.267	330.913	342.714	422.640
155.148	220.702	254.246	334.647	344.743	421.688
157.060	221.969	256.213	337.673	346.769	422.576
158.957	223.435	258.168	341.429	348.795	423.433
160.842	225.899	260.113	346.133	350.823	423.405
162.717	225.968	262.048	351.913	352.846	424.452
164.624	228.546	263.977	358.940	354.871	425.316
166.570	230.426	265.896	365.659	356.888	427.998
168.501	232.637	267.794	376.041	358.907	427.481
170.422	234.547	269.819	385.715	360.912	427.964
172.328	236.398	271.924	389.540	362.920	429.779
174.224	238.394	273.809	428.291	364.928	429.515
176.109	239.032	275.671	483.464	366.927	432.775
Series 2 (from 200 to 350 K)					
200.914	263.743	263.694	356.567	305.827	412.703
204.523	267.795	264.853	357.329	309.958	413.649
208.166	272.154	265.489	365.472	312.022	414.143
211.126	275.978	268.275	379.717	315.143	415.195
214.070	279.667	271.734	389.851	318.200	415.380
216.988	282.792	273.883	444.189	321.307	416.111
219.952	285.992	275.895	506.737	324.357	417.116
222.955	289.335	277.703	618.242	327.452	418.062
225.939	293.441	279.236	832.848	330.493	418.738
228.900	294.685	280.434	1224.335	333.575	418.810
231.807	298.703	281.294	1876.568	336.611	420.356
234.776	302.820	281.897	2768.224	339.680	421.044
237.799	304.937	282.310	3848.881	342.714	422.140
240.796	309.951	282.603	5161.454	345.769	422.576
241.316	312.567	282.820	6533.372	348.795	423.433
243.839	317.567	282.982	7973.548	351.846	424.452

T /K	$C_{p,m}^0$ /J·K^{-1}·mol^{-111}	*T*/K	$C_{p,m}^0$ /J·K^{-1}·mol^{-1}	*T*/K	$C_{p,m}^0$ /J·K^{-1}·mol^{-1}
246.762	321.567	283.106	9917.953	354.871	425.316
249.985	324.567	283.295	5149.314	357.907	426.481
251.862	330.829	284.559	409.393	360.912	427.964
254.943	336.749	286.799	411.977	363.928	429.015
257.427	339.322	290.762	411.976	366.927	432.975
259.972	342.567	294.390	411.989	369.927	435.075
261.233	347.567	297.539	411.530		
262.148	349.567	301.688	412.158		
Series 3 (from 200 to 340 K)					
198.627	222.413	249.208	255.056	288.134	347.592
202.314	221.805	252.242	273.365	292.152	371.843
206.065	216.489	255.264	277.024	295.213	332.434
209.052	224.270	258.244	268.206	298.368	419.994
212.132	231.179	261.148	266.542	301.254	419.994
215.313	174.192	264.050	273.986	305.664	382.918
217.887	199.884	266.864	294.272	309.117	265.313
220.719	245.593	269.792	307.914	312.366	277.570
223.749	232.252	272.608	317.557	315.485	259.491
226.696	240.415	275.334	390.096	318.765	223.573
229.815	243.594	278.062	510.599	321.536	285.323
232.774	255.469	280.873	462.126	324.117	471.394
235.826	269153	282.575	8988.111	328.883	200.130
238.890	260902	282.990	9847.518	331.993	462.769
242.563	262.842	283.172	10867.388	335.827	176.378
246.192	265.801	284.767	483.962		

Table 3. Experimental molar heat capacities of [EMIM][TCB] (M = 226.047 g·Mol^{-1}).

3.1.4. The temperature, enthalpy and entropy of solid: liquid phase transition

The standard molar enthalpies and entropies of the solid–liquid phase transition $\Delta_{fus}H_m^0$ and $\Delta_{fus}S_m^0$ of the compound were derived according to the following equations:

$$\Delta_{fus}H_m^0 = \frac{Q - n\int_{T_i}^{T_m} C_{p,m}^0(s)dT - n\int_{T_i}^{T_m} C_{p,m}^0(l)dT - \int_{T_i}^{T_m} H^0(s)dT}{n} \quad (6)$$

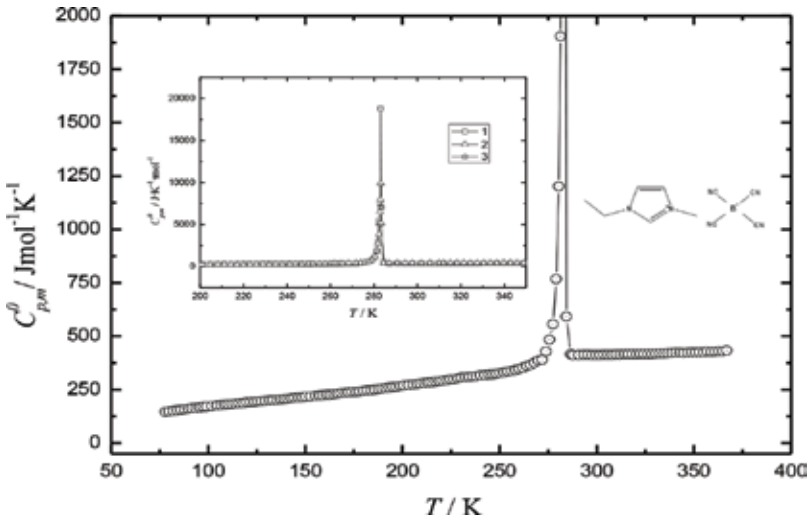

Figure 9. Experimental molar heat capacity of [EMIM][TCB] as a function of temperature: outer part from 78 to 370 K for the first series of measurements in the whole temperature range; inner part, from 200 to 350 K of three series of measurements in the melting process.

$$\Delta_{fus} S_m^0 = \frac{\Delta_{fus} H_m^0}{T_m} \tag{7}$$

where T_i is the temperature that is somewhat lower than the temperature of the onset of a solid–liquid transition and Tf is the temperature slightly higher than that of the transition completion. Q the total energy introduced into the sample cell from T_i to T_f, H_0 the standard heat capacity of the sample cell from T_i to T_f, $C_{p,m}^0$(s) the standard heat capacity of the sample in solid phase from T_i to T_m, $C_{p,m}^0$(l) the standard heat capacity of the sample in liquid phase from T_m to T_f and n is molar amount of the sample. The heat capacity polynomials mentioned above were used to calculate the smoothed heat capacities, and were numerically integrated to obtain the values of the standard thermodynamic functions above T = 298.15 K. The calculated results of molar enthalpy and entropy of fusion obtained from the three series of heat-capacity were listed in **Table.4**.

3.1.5. Thermodynamic functions

The thermodynamic functions of the [EMIM][TCB] relative to the reference temperature 298.15 K were calculated in the temperature range from 80 to 370 K with an interval of 5 K, using the polynomial equation of heat capacity and thermodynamic relationships as follows:

Before melting,

$$H_T^0 - H_{298.15}^0 = \int_{298.15}^{T} C_{p,m}^0(s)\, d\, T \tag{8}$$

No	Melting temperature T_m /K	$\Delta_{fus} H_m^0$/ kJ·mol^{-1}	$\Delta_{fus} S_m^0$/J·K^{-1}·mol^{-1}
1	283.092	12.957	45.770
2	283.106	12.985	45.867
3	283.172	12.976	45.825
Mean Value	283.123 ± 0.025	12.973 ± 0.008	45.821 ± 0.028

Table 4. The melting temperature, enthalpy and entropy of fusion of [EMIM][TCB] obtained from three series of heat-capacity measurements.

$$S_T^0 - S_{298.15}^0 = \int_{298.15}^{T} \frac{C_{p,m}^0(s)}{T} d\,T \tag{9}$$

After melting,

$$H_T^0 - H_{298.15}^0 = \int_{298.15}^{T_i} C_{p,m}^0(s)\, d\,T + \Delta_{fus} H_m^0 + \int_{T_i}^{T} C_{p,m}^0(l)\, dT \tag{10}$$

$$S_T^0 - S_{298.15}^0 = \int_{298.15}^{T_i} \left[\frac{C_{p,m}^0(s)}{T}\right] dT + \frac{\Delta_{fus} H_m^0}{T_m} + \int_{T_i}^{T} \left[\frac{C_{p,m}^0(l)}{T}\right] dT. \tag{11}$$

where T_i is the temperature at which the solid–liquid phase transition started; T_f is the temperature at which the solid–liquid phase transition ended; $\Delta_{fus} H_m^0$ is the standard molar enthalpy of fusion; T_m is the temperature of solid–liquid phase transition. The standard thermodynamic functions, $[H_T^0 - H_{298.15}^0]$, $[S_T^0 - S_{298.15}^0]$, are listed in **Table 5**.

3.2. Heat capacity and thermodynamic properties of nanostructured materials

3.2.1. Introduction

Nanostructured materials have attracted worldwide attention owing to their special properties. Due to their small grain size and large specific surface, nano materials exhibit many distinctive properties [46]. What are the special thermodynamic properties of nano materials? Can classical thermodynamic theories be used to explain the thermal behavior of nano- materials? These are some of the important questions that must be answered in order to understand the properties of nano- materials more thoroughly and broaden their application areas.

In this chapter we have reported the results of heat capacity measurements of several kinds of nanostructured oxides, metals and zeolites, obtained by low-temperature adiabatic calorimetry, and compared heat capacity enhancement in these materials with the corresponding coarse-grained materials. These data are discussed in the context of properties such as density, thermal expansion, sample purity, surface effect, and size effect. Synthesis of nano materials has been accompanied by adiabatic calorimetry measurements, and materials have been characterized with differential scanning calorimetry (DSC), thermogravimetric (TG) analysis,

T/K	$C^0_{p,m}$/ J·K^{-1}·mol^{-1}	$H^0_T - H^0_{298.15}$/kJ·mol^{-1}	$S^0_T - S^0_{298.15}$/ J·K^{-1}·mol^{-1}
80	150.104	−70.915	−360.705
90	158.233	−69.378	−342.560
100	169.437	−67.740	−325.218
110	180.604	−65.989	−308.533
120	190.456	−64.133	−292.444
130	198.919	−62.185	−276.919
140	206.588	−60.157	−261.921
150	214.303	−58.053	−247.393
160	222.826	−55.868	−233.258
170	232.631	−53.592	−219.424
180	243.784	−51.211	−205.797
190	255.944	−48.713	−192.298
200	268.461	−46.091	−178.874
210	280.574	−43.345	−165.506
220	291.727	−40.483	−152.208
230	301.977	−37.514	−139.010
240	312.513	−34.443	−125.924
250	326.284	−31.253	−112.889
260	348.719	−27.888	−99.696
270	388.568	−24.221	−85.874
280	Melting		
290	412.609	−5.282	−18.601
298.15	412.020	0.000	0.000
300	412.204	1.385	4.868
310	413.721	10.475	36.838
320	415.513	23.248	81.985
330	417.856	41.426	146.718
340	420.859	67.316	239.595
350	424.059	103.928	371.805
360	427.723	155.130	557.707
370	435.829	225.809	815.441

Table 5. Calculated thermodynamic functions of [EMIM][TCB].

thermal expansion coefficient measurements, X-ray diffraction (XRD), transitional electron microscopy (TEM), scanning electron microscopy (SEM), X-ray fluorescence (XRF) and infrared spectroscopy (IR). Full details about the synthesis and characterization of materials were published elsewhere [47].

3.2.2. Nanostructured oxides

Nano oxide materials constitute a rich source of materials. We selected five kinds of oxide materials, Al_2O_3, SiO_2, TiO_2, ZnO_2, and ZrO_2, which have been widely used, can be prepared by classical methods and obtained with confined size range and high quality.

3.2.2.1. Nano Al_2O_3

We studied molar heat capacity of nano Al_2O_3 in the temperature range from 78 to 370 K, and compared with the coarse-grained Al_2O_3 [48]. The nanopowder Al_2O_3 was processed by hydrolysis of pure aluminum sheet after activation, and the sample purity is more than 99%. The coarse-grained sample of α- Al_2O_3 is a commercial reagent purchased from Shanghai Chemical Reagent factory with the mass purity of 99.9%. **Figure 10** shows the experimental results indicating that no thermal anomaly took place over the investigated temperature range, but the heat capacities of the nano Al_2O_3 was larger than the coarse-grained one and increased with the size decreased. The nano Al_2O_3 has excess heat capacity from 6 to 23% as comparing with the coarse-grained one in the temperature range from 200 to 370 K. In the study of infrared spectra, we found that nano Al_2O_3 exhibited a blue shift in wave number. This shift indicates that energy structure of nano Al_2O_3 is higher than that in coarse-grained state, which is in agreement with the results of heat capacity measurement. To further study the enhancement of heat capacity in nano Al_2O_3, we measured the density of nano Al_2O_3 to be 89% of the coarse-grained one, and thermal expansion of nano Al_2O_3 has been reported to be twice as that of the conventional. All these suggest that the grain boundary of nano materials possesses an excess volume with respect to the perfect crystal lattice, so it seems that the heat capacity enhancement in nano Al_2O_3 results from the excess volume.

3.2.2.2. Nano amorphous SiO_2

The molar heat capacity of nano amorphous SiO_2 (na-SiO_2) was measured over the temperature range from 9 to 354 K. The samples used for experiment were synthesized by using the sol–gel route with hydrolyzing the ethyl tetrasilicate and controlling the chemical reaction conditions. Those samples possess a very high purity (>99.9%). The experimental results were plotted in **Figure 11** together with the molar heat capacity of coarse-grained SiO_2 (ca- SiO_2). The average grain size of two amorphous SiO_2 is also 20 nm and their specific surfaces resulted from BET measurement are 160 m^2/g (SiO_2–1) and 640 m^2/g (SiO_2–2) respectively. Significant difference in heat capacity between na-SiO_2 and ca- SiO_2 can be identified from **Figure 11**. The heat capacity enhancement from 150 to 350 K for na- SiO_2–1 and na-SiO_2–2 are about 2–7% and 4–10% higher than those of ca-SiO_2, respectively. The heat capacity values of na-SiO_2–2 with larger specific surface are higher about 3% than those of na-SiO_2–1. The heat capacity enhancements

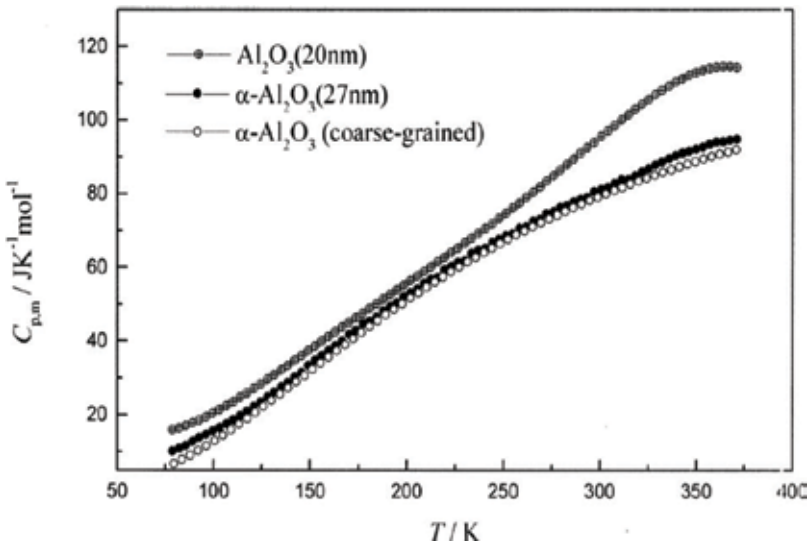

Figure 10. Heat capacity of nano and coarse-grained Al_2O_3.

in the nanomaterials are usually associated with an increase in the configuration and vibrational entropy of grain boundaries, and the boundaries with larger specific surface will have more configuration and vibrational entropy. So it agrees well with the experimental results that larger grain surface has much contribution to the heat capacity enhancement. We calculated the thermodynamic functions of na-SiO_2 based on the heat capacity data. The calculated results were plotted in the **Figure 12**. From the figure, we can conclude that the entropy,

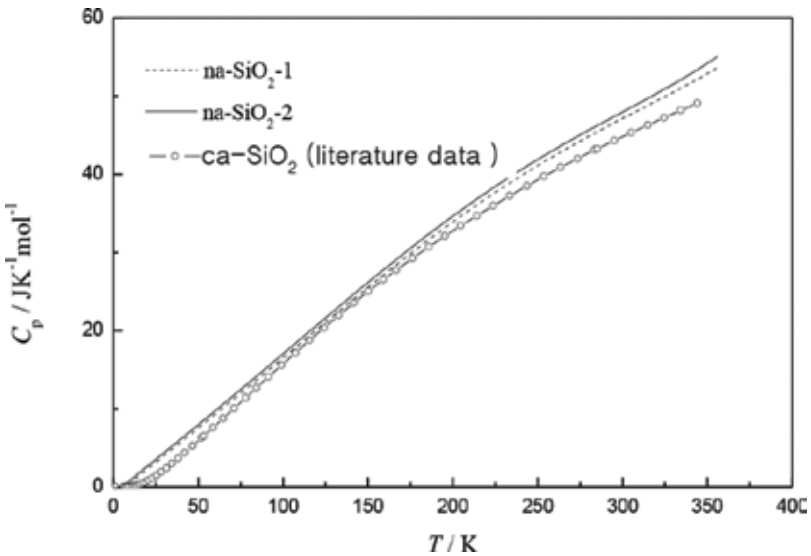

Figure 11. Heat capacity of nano amorphous and coarse-grained SiO_2 as functions of temperature.

enthalpy and Gibbs free energy of larger specific surface na-SiO_2 is higher than those of the small one, and the Gibbs free energy is lower, implying larger specific surface materials have complicated disorder, large potential energy and high activity.

3.2.2.3. Nanocrystalline ZnO

The two nanocrystalline forms of ZnO studied are ZnO-1 and ZnO-2 with grain size of 65 and 18 nm, respectively. The purity of both two samples is more than 99%. Heat capacity of nanocrystalline ZnO was compared with the literature data [49] of coarse-grained ZnO (c-ZnO) in **Figure 13**. It can be seen that the heat capacities of ZnO-1 is no obviously difference from that of c-ZnO. However, there is large excess heat capacity of 4–17% for ZnO-2 compared with c-ZnO. The similar result was also reported by other researchers. Heat capacity of a material is directly related to its atomic structure, or its vibrational and configurational entropy which is significantly affected by the nearest-neighbor configurations. Nanocrystals are structurally characterized by the ultrafine crystalline grains, and a large fraction of atoms located in the metastable grain boundaries in which the nearest-neighbor configurations are much different from those inside the crystallites. In other words, the grain-boundary possesses an excess volume with respect to the perfect crystal lattice. Therefore, heat capacities of nanocrystals are higher than those of the corresponding coarse-grained polycrystalline counterparts. Although slight impurity can enhance the heat capacity obviously [50], the impurity effect on those two specimens should be very slight. The samples were heated at temperature up to 570 K for 2 h and sample cells were evacuated to be high vacuum (10^{-5} Pa), which can remove the absorbed gas and vapor. So the main contribution of the excess heat capacity of nanocrystaliline ZnO-2

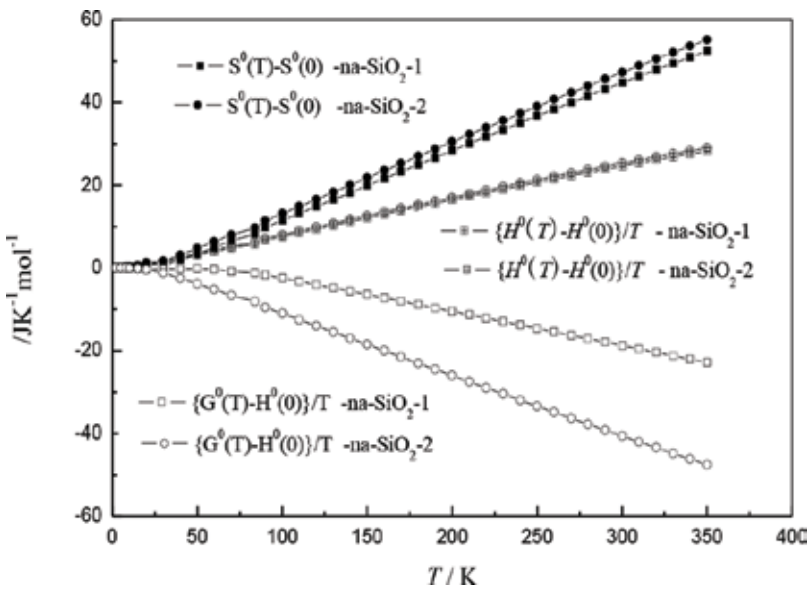

Figure 12. Entropy, enthalpy and Gibbs free energy of nano amorphous SiO_2 as functions of temperature.

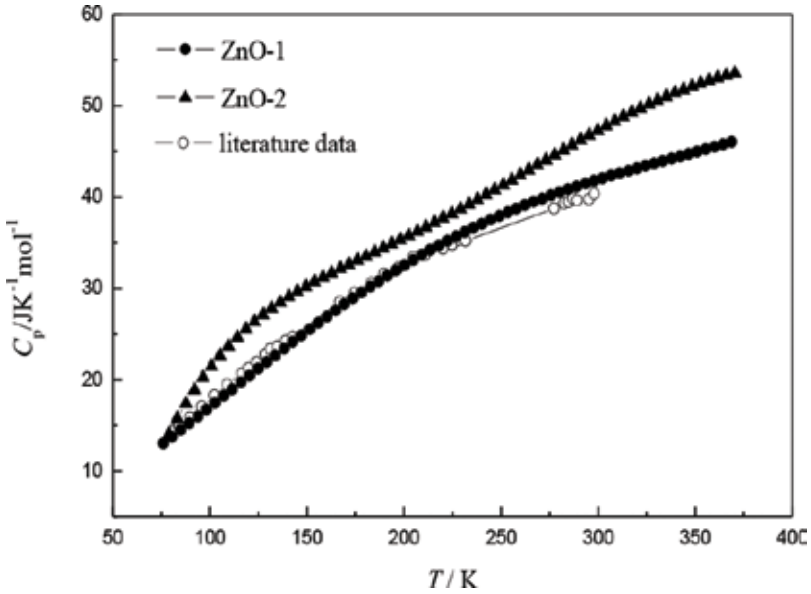

Figure 13. Heat capacity of nanocrystalline ZnO and the literature heat capacity data of coarse-grained crystalline ZnO.

should be introduced by vibrational and configurational entropy due to grain boundaries and lattice defects.

It seems to contradict our understanding of the above excess heat capacity, that nanocrystalline ZnO-1 and the more coarse-grained ZnO display very little difference. In fact, the grain size effect of nanocrystals on heat capacity has a size limit [50]. If the grain size is lower than the limit, the heat capacity will exhibit a great increase. Otherwise, heat capacity of nanocrystals and conventional polycrystals has little difference.

3.2.2.4. Nanocrystalline TiO_2

We measured heat capacity of nanocrystalline TiO_2 with three grain sizes by adiabatic calorimetry. TiO_2–2 and TiO_2–3 are anatase phase with the purity of 99% and TiO_2–1 is mainly anatase with a small amount of brookite phase. The experimental results were compared with reported heat capacity of coarse-grained anatase phase TiO_2 [51] in **Figure 14**. It is very obvious that the heat capacity of nanocrystalline was enhanced, and the heat capacities increase with grain size decreasing. The heat capacity enhancement of TiO_2–1 and TiO_2–2 was plotted in **Figure 14**. In the temperature range from 100 to 300 K, the heat capacity enhancement of TiO_2–1 and TiO_2–2 were 7–13% and 4–7%, respectively. The heat capacity enhancement of TiO_2–1 relative to TiO_2–2 was 3–6%, while the enhancement of TiO_2–2 relative to TiO_2–3 was only about 1%. Considered the size decreasing step is equal from TiO_2–3 to TiO_2–2 and from TiO_2–2 to TiO_2–1, the nanocrystalline size is not the main factor affected the heat capacity enhancement in this case. The sample of TiO_2–1 contains mainly anatase phase with a small amount of brookite phase and the samples of TiO_2–2 and TiO_2–3 are all anatase phase, so we can draw a conclusion that the small amount of heteromorphic

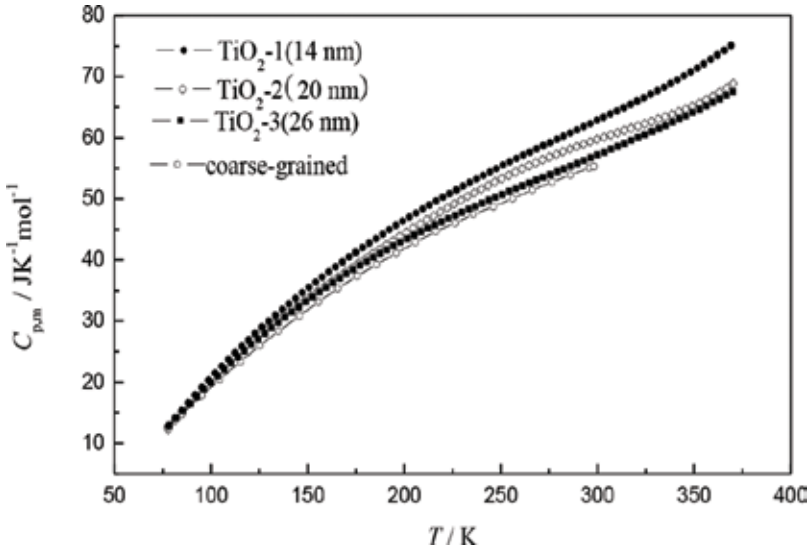

Figure 14. Heat capacity of anatase phase nanocrystalline TiO_2 with different grain sizes.

impurity makes more contribution to the heat capacity enhancement than the grain size. Recently research work by Boerio-Goats et al. reported that the water or other solvents absorbed on nanoparticle surfaces lead to heat capacity enhancement of anatase phase nanopartiles [52] (**Figures 15–17**).

3.2.2.5. Nanocrystalline ZrO_2

Nanocrystalline ZrO_2 with grain size of 18 nm was measured by adiabatic heat capacity calorimetry and compared with literature data of coarse-grained ZrO_2 [53]. The sample was prepared with the method of azeotropic distillation, and the purity is more than 99%. The heat capacity enhancement of nanocrystalline ZrO_2 was much larger than those of above nanostructured oxides. The enhancement was about 2–21% in the temperature range from 100 to 300 K, and exhibited a rising tendency with the temperature increasing. Many researchers theoretically explained the excess heat capacity of nano materials by excess volume, and some theoretical calculations have indicated that heat capacity enhancement sharply increases with the excess volume increasing when temperature rises [54]. We measured the density of the nanocrystalline ZrO_2 sample (5.2 g·cm^3) to be 93% of the coarse-grained ZrO_2 (5.6 g·cm^3). This difference in density is not very obvious and can hardly lead to 2–21% of heat capacity enhancement. We also measured the chemical purity of the nanocrystalline ZrO_2 to be 98.4%, so the contribution of impurity contained in the nanocrystalline to heat capacity enhancement cannot be neglected. We presume that heat capacity enhancement in the nanocrystalline ZrO_2 is mainly caused by impurity contained in it. Impurity in nano materials is not the general case of adulteration, since it is not avoided in the process of sample preparation, but it can bring activity to the materials. So nanocrystalline ZrO_2 has higher activity than coarse-grained one and is mostly used as a catalyst in some reactions.

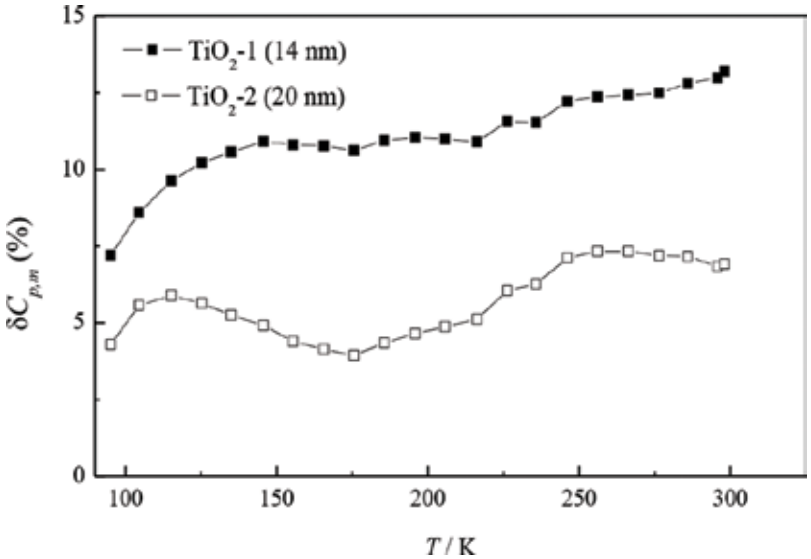

Figure 15. Heat capacity enhancement of nanocrystalline TiO_2 as a function of temperature, $\delta C_{p,m}$ (%) = 100%*[$C_{p,m(nano)} - C_{p,m(coarse)}$]/$C_{p,m(coarse)}$.

3.2.3. Nanocrystalline metal

Nanocrystalline metals are studied mostly in theory because its molecular structure is simple and easily calculated and explained. Those materials differ from glasses and crystals in the sense that they exhibit little short-range or long-range order. A series of novel physical

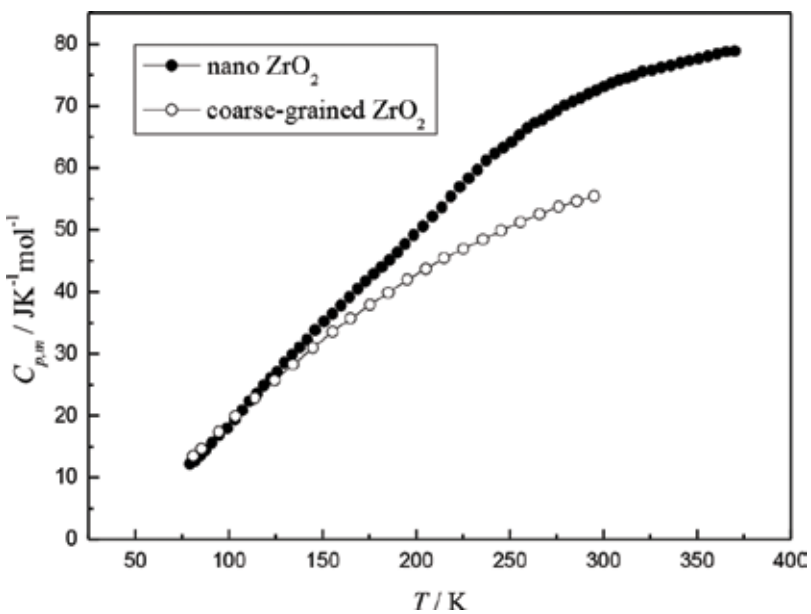

Figure 16. Heat capacity of nanocrystalline ZrO_2 and the literature heat capacity data of coarse-grained crystalline ZrO_2.

and chemical properties of the nanocrystals, such as high diffusivity and reactivity, great ductility, large thermal expansion, enhanced phonon specific heat, and a significant change in the magnetic susceptibility, relative to the corresponding coarse-grained polycrystals, have captured the attention of the scientists and engineers because of their potential application. We measured heat capacities of nanocrystalline nickel and copper in the temperature range from 78 K to 370 K, and studied the heat capacity enhancement relative to the corresponding coarse-grained metal crystal. The two samples were produced by Zhengyuan Nano-materials Engineering Corp. (Shandong, China). The labeled chemical purity is not less than 99%.

3.2.3.1. Nanocrystalline nickel

Heat capacity of 40 nm nanocrystalline nickel was plotted in **Figure 17** and compared with the literature data [55] of coarse-grained crystalline nickel. From insert in the figure we can see that heat capacity enhancement varies between 2 and 4% in the temperature range from 100 to 370 K. The heat capacity enhancement in nanocrystalline materials are usually associated with an increase in the configurational and vibrational entropy of the grain boundaries, which constitute a large volume fraction of the material. The atomic fraction of the grain-boundary component can be approximately estimated to be 3δ/d, where d is the average size of crystalline grain and δ is the average thickness of interfaces which is known to be on the order of three or four atomic layers. For the nanocrystalline nickel with d = 40 nm, about 10% atoms are on the grain boundaries. Thus, the grain-boundary configurations or the grain-boundary energy should be responsible for the heat capacity enhancement.

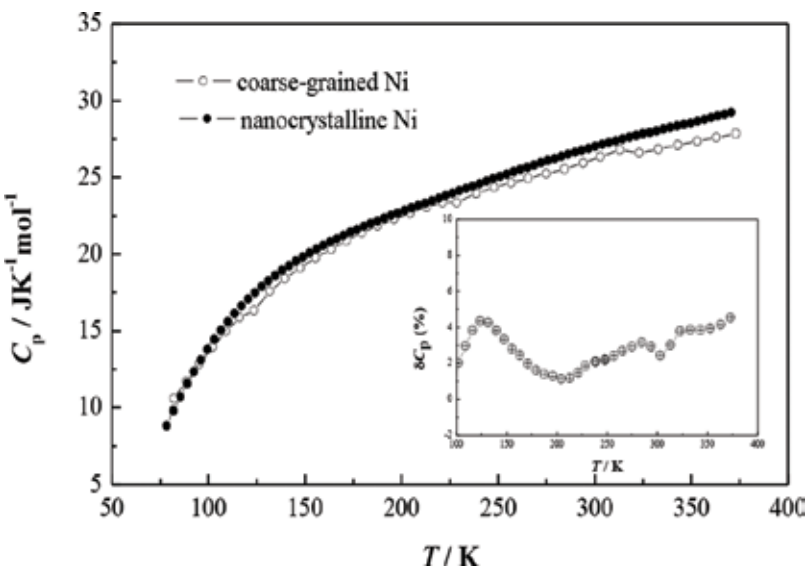

Figure 17. Heat capacity of nanocrystalline nickel and the literature heat capacity data of coarse-grained crystalline nickel, insert is heat capacity enhancement of nanocrystalline nickel.

3.2.3.2. Nanocrystalline copper

Figure 18 shows the heat capacity of 50 nm nanocrystalline copper and the literature data [56] of coarse-grained one. The heat capacity enhancement is about 3–6% in the temperature range from 100 to 370 K. The purity of nanocrystalline copper is more than 99%, so the contribution of impurity to the enhancement is almost negligible. The relative density of nanocrystalline copper to the coarse-grained is 51% indicating a more open atomic structure of the grain-boundary component than coarse-grained polycrystalline copper, so the interatomic coupling becomes weaker and enhances heat capacity. In the theoretical calculation by Fecht et al., [57], thermal expansion coefficient is related to heat capacity, and the larger thermal expansion coefficient becomes, the more heat capacity enhances. We measured thermal expansion coefficient of nanocrystalline copper (3×10^{-5} K^{-1}) to be about two times of the coarse-grained copper's (1.6×10^{-5} K^{-1}). Thus, we can also explain the heat capacity enhancement of nanocrystalline copper with the increasing thermal expansion coefficient.

3.2.4. Nanosized and microsized zeolite

Nanosized zeolite is only different from microsized zeolite in the size, but its properties have varied much in some aspects when it changes into microsized zeolite. We carried out adiabatic heat capacity measurement on nanoszied and microsized ZMS-5, and compared their thermodynamic properties. From **Figure 19** it can be clearly seen that the heat capacities of nanosized ZMS-5 are larger than the microsized one. The heat capacity enhancement in the low temperature is not very obvious, but becomes larger with the temperature increasing.

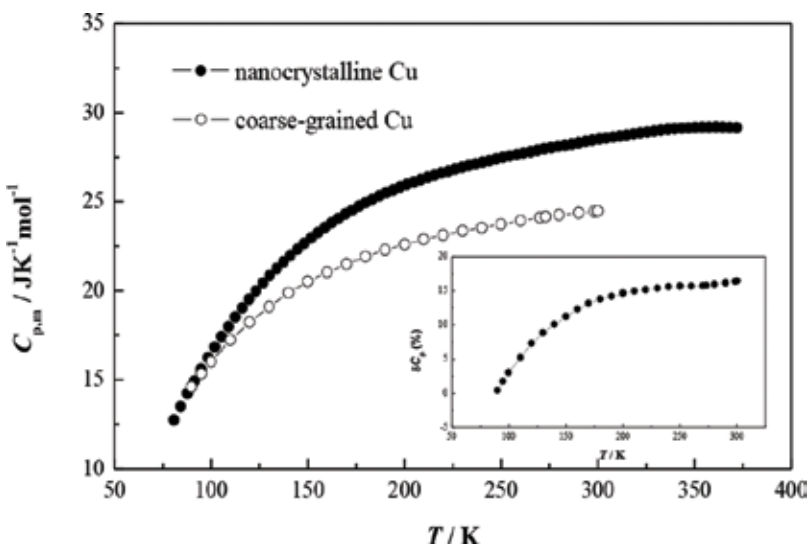

Figure 18. Heat capacity of nanocrystalline copper and the literature heat capacity data of coarse-grained crystalline copper, insert is heat capacity enhancement of nanocrystalline copper.

http://dx.doi.org/10.5772/intechopen.76151

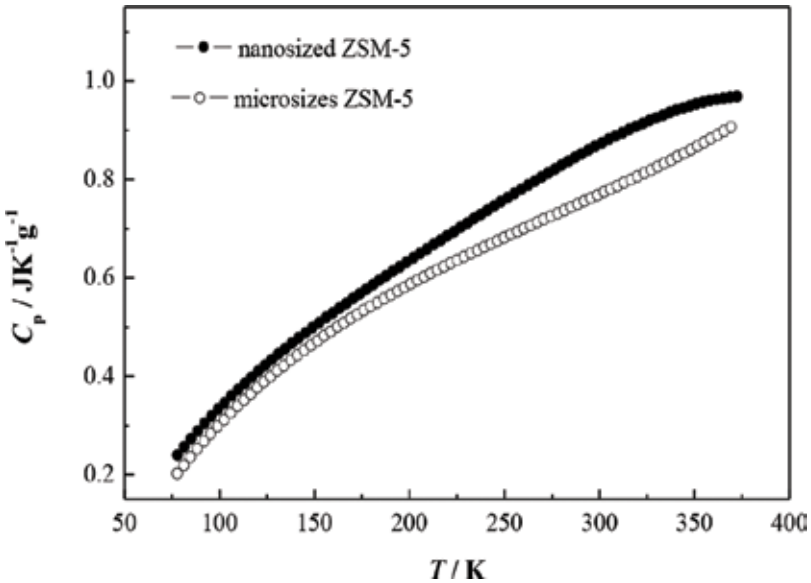

Figure 19. Heat capacity of nanosized and microsized ZSM-5.

Nanosized ZMS-5 possesses excess specific surface and behaves more activity than the microsized. This excess specific surface supplies more surface energy for nanosized ZMS-5 and enhances heat capacity.

4. Conclusions

A fully automated high-precision adiabatic calorimeter used for heat capacity measurement in the temperature range of 80–400 K was constructed. The reliability of the calorimeter was verified by measuring the heat capacities of synthetic sapphire (α-Al_2O_3), Standard Reference Material 720. The deviation of the data obtained by this calorimeter from those published by NIST was within ±0.1% in the temperature range from 80 to 400 K. The adiabatic calorimeter can be used for precise measurement of molar heat capacities of condensed materials with important scientific value.

The heat capacities of IL [EMIM][TCB] were measured over the temperature range from 78 to 370 K by the high-precision-automated adiabatic calorimeter. Based on the heat capacity measurement experiments, the thermodynamic properties of fusion were calculated, and the thermodynamic functions $[H_T^0 - H_{298.15}^0]$ and $[S_T^0 - S_{298.15}^0]$ were derived in the range from 78 to 370 K with temperature interval of 5 K. The melting temperature, standard molar enthalpy and entropy of fusion were determined to be (283.123 ± 0.025) K, (12.973 ± 0.008) kJ·mol^{-1} and (45.821 ± 028) J·K^{-1}·mol^{-1}, respectively. The IL was shown to be thermostable below 570 K and began to lose weight at 592.83 K.

Five kinds of nanostructured oxide materials, Al_2O_3, SiO_2, TiO_2, ZnO_2, ZrO_2, and two kinds of nanocrystalline metals: nickel and copper were investigated from heat capacity measurements. It is found that heat capacity enhancement in nanostructured materials is influenced by many factors, such as density, thermal expansion, sample purity, surface absorption, size effect, and so on. But the dominant factor affected heat capacity enhancement is different in different nanostructured materials. Only with careful and entire investigation on the particular properties of nanostructured materials, we can discuss and analyze the heat capacity enhancement. On the other hand, adiabatic calorimetry is the most direct method to measure heat capacity enhancement in nanostructured materials, however in order to set up thermodynamic theoretical model to describe and understand heat capacity enhancement, more theoretical calculation study and other experimental measurements should be further carried out.

Acknowledgements

This work was financially supported by the National Natural Science Foundation of China under the grant NSFC No.21473198 and No. 20073047. Some parts of this chapter are reproduced from authors' recent conference publication, work, etc.

Author details

Zhi Cheng Tan*, Quan Shi and Xin Liu

*Address all correspondence to: tzc@dicp.ac.cn

Thermochemistry Laboratory, Dalian Institute of Chemical Physics, Chinese Academy of Science, Dalian, China

References

[1] Tan ZC, Di YY. Review of modern low temperature adiabatic calorimetry. Progress in Chemistry. 2006;**18**:1234

[2] Lang BE, Boerio-Goates J, Woodfield BF. Design and construction of an adiabatic calorimeter for samples of less than 1 cm3 in the temperature range T = 15 K to T = 350 K. The Journal of Chemical Thermodynamics. 2006;**38**:1655

[3] Kobashi K, Kyomen T, Oguni M. Construction of an adiabatic calorimeter in the temperature range between 13 and 505 K, and thermodynamic study of 1-chloroadamantane. Journal of Physics and Chemistry of Solids. 1998;**59**:667

[4] Sorai M, Kaji K, Kaneko Y. An automated adiabatic calorimeter for the temperature-range 13 K to 530 K the heat-capacities of benzoic-acid from 15 K to 305 K and of synthetic sapphire from 60 K to 505 K. The Journal of Chemical Thermodynamics. 1992;**24**:167

[5] Matsuo T, Suga H. Adiabatic microcalorimeters for heat-capacity measurement at low-temperature. Thermochimica Acta. 1985;**88**:149

[6] Inaba A. An adiabatic calorimeter for use at intermediate and higher temperatures - the heat-capacity of synthetic sapphire (alpha-Al_2O_3) from 70 K to 700 K. Journal of ChemicalThermodynamics. 1983;**15**:1137

[7] Ditmars DA, Ishira S, Chang SS, Bernstein G, West ED. Enthalpy and heat-capacity standard reference material - synthetic sapphire (alpha-Al_2O_3) from 10 to 2250 K. Journal of Research of the National Bureau of Standards. 1982;**87**:159

[8] Andrews JTS, Norton PA, Westrum EF Jr. Adiabatic calorimeter for use at super-ambient temperatures - heat-capacity of synthetic sapphire (alpha-Al_2O_3) from 300K to 550K. The Journal of Chemical Thermodynamics. 1978;**10**:949

[9] Westrum EF Jr, Furukawa GT, McCullough JP. In: McCullough JP, Scott DW, editors. Experimental Thermodynamics, Vol. I Calorimetry of Non-reacting Systems. London: Butterworths; 1968. p. 133

[10] Tan ZC, Li FX. An automatic adiabatic calorimeter for heat capacity measurements of solids in the range 4.2-30 K. Thermochimica Acta. 1995:253,189

[11] Tan ZC, Yin AX, Cheng SX, Zhou LX. An automated adiabatic calorimeter for heat capacity measurements between 20 and 90 K. Thermochimica Acta. 1988:123,105

[12] Tan ZC, Yin AX, Cheng SX, Zhou LX. National Standard of heat capacity measurement of solids in the range of 4.2 - 90 K. Science in China, Series B. 1991;**34**:560

[13] Tan ZC, Zhou LX, Cheng SX, Yin AX, Sun Y, Ye JC, Wang X. An adiabatic calorimeter for heat capacity measurements from 80 to 400 K —Heat capacities of alpha-alumina and *n*-heptane. Scientia Sinica, Series B. 1983;**26**:1014

[14] Yin AX, Wang WB, Tan ZC. Construction of microcomputer control measurements of low temperature heat capacity. Computers and Applied Chemistry. 1990;**7**:176

[15] Tan ZC, Liu BP, Yan JB, Sun LX. Computers and Applied Chemistry. 2003;**20**:264

[16] Tan ZC, Sun GY, Sun Y. An adiabatic low-temperature calorimeter for heat capacity measurement of small samples. Journal of Thermal Analysis. 1995;**45**:59

[17] Tan ZC, Sun GY, Song YJ, Wang L, Han JR, Liu YS, Wang M, Nie DZ. An adiabatic calorimeter for heat capacity measurements of small samples, the heat capacity of nonlinear optical materials $KTiOPO_4$ and $RbTiOAsO_4$ crystals. Thermochimica Acta. 2000;**247**:352

[18] Tan ZC, Zhang JB, Meng SH, Li L. A small sample-size automated adibadic calorimeter from 70 to 580 K-Molar heat capacities of alpha—Al_2O_3. Science in China, Series B. 1999;**42**:382

[19] Tan ZC, Sun LX, Meng SH, Li L, Xu F, Yu P, Liu BP, Zhang JB. Heat capacities and thermodynamic functions of P-chlorobenzoic acid. The Journal of Chemical Thermodynamics. 2002;**34**:1417

[20] Tan ZC, Ye JC, Sun Y, Cheng SX, Zhou LX. An adiabatic calorimeter for heat capacity measurements in the temperature range 300-600 K and pressure range 0.1-15 MPa. Thermochimica Acta. 1991;**183**:29

[21] Tan ZC, Shi Q, Liu BP, Zhang HT. A fully automated adiabatic calorimeter for heat capacity measurement between 80 and 400 K. Journal of Thermal Analysis and Calorimetry. 2008;**92**:367

[22] Sun Y, Tan ZC, Yin AX. An automated adiabatic copper block calorimeter for enthalpy measurements in the range of 400-1700 K. Acta Metrologica Sinica. 1982;**3**:301

[23] AGILENT, HP. 34970A Data Acquisition/Switch Unit, User'S Guide. 2nd ed. Hewlett Packard; 1997

[24] AGILENT, HP. 34420A Nano Volt/Micro-Ohm Meter, User's Guide. 2nd ed. Hewlett Packard; 2003

[25] Archer DG. Thermodynamic properties of synthetic sapphire (alpha—Al_2O_3), standard reference material 720 and the effect of temperature-scale differences on thermodynamic properties. Journal of Physical and Chemical Reference Data. 1993;**22**:1411

[26] Heintz A. Recent developments in thermodynamics and thermophysics of non-aqueous mixtures containing ionic liquids. A review. The Journal of Chemical Thermodynamics. 2005;**37**:525

[27] Ikegami S, Hamamoto H. Novel Recycling System for Organic Synthesis via Designer Polymer-Gel Catalysts. Chemical Reviews. 2009:109,583

[28] Rogers RD, Seddon KR, editors. Ionic Liquids: Industrial Application for Green Chemistry, ACS Symposium Series 818. Washington DC: American Chemical Society; 2002

[29] Rogers RD, Seddon KR, editors. Ionic Liquids as Green Solvents: Progress and Prospects, ACS Symposium Series 856. Washington DC: American Chemical Society; 2003

[30] Gurkan BE, de la Fuente JC, Mindrup EM, Ficke LE, Goodrich BF, Price EA, Schneider WF, Brennecke JF. Equimolar CO_2 Absorption by Anion-Functionalized Ionic Liquids. Journal of the American Chemical Society. 2010;132:2116

[31] Wang SF, Chen T, Zhang ZL, Pang DW, Wong KY. Effects of hydrophilic room-temperature ionic liquid 1-butyl-3-methylimidazolium tetrafluoroborate on direct electrochemistry and bioelectrocatalysis of heme proteins entrapped in agarose hydrogel films. Electrochemistry Communications. 2007;**9**:1709

[32] Gordon CM. New developments in catalysis using ionic liquids. Applied Catalysis A-General. 2001;**222**:101

[33] Olivier-Bourbigou H, Magna L, Morvan D. Ionic liquids and catalysis: Recent progress from knowledge to applications. Applied Catalysis A-General. 2010;**373**:1-56

[34] Yan PF, Yang M, Liu XM, Wang C, Tan ZC, Welz-Biermann U. Activity coefficients at infinite dilution of organic solutes in the ionic liquid 1-ethyl-3-methylimidazolium etracyanoborate [EMIM][TCB] using gas–liquid chromatography. The Journal of Chemical Thermodynamics. 2010;**42**:817

[35] Verevkin SP, Vasiltsova TV. Bich E, Heintz A. Thermodynamic properties of mixtures containing ionic liquids. Activity coefficients of aldehydes and ketones in 1-methyl-3-ethyl-imidazolium bis(trifluoromethyl-sulfonyl) imide using the transpiration method. Fluid Phase Equilibria. 2004;**218**:165

[36] Heintz A, Kulikov DV, Verevkin SP. Thermodynamic properties of mixtures containing ionic liquids. Activity coefficients at infinite dilution of polar solutes in 4-methyl-N-butyl-pyridinium tetrafluoroborate using gas-liquid chromatography. Journal of Chemical Thermodynamics. 2002:341,1347

[37] Yang JZ, Jin Y, Xu WG, Zhang QG, Zang SL. Studies on mixture of ionic liquid EMIGaCl_{14} and EMIC. Fluid Phase Equilibria. 2005;**227**:41

[38] Tong B, Liu QS, Tan ZC, Welz-Biermann U. Thermochemistry of Alkyl Pyridinium Bromide Ionic Liquids: Calorimetric Measurements and Calculations. The Journal of Physical Chemistry. A. 2010;**114**:3782

[39] Verevkin SP, Emel'yanenko VN, Toktonov AV, Goodrich P, Hardacre C. Thermochemistry of Ionic Liquid Catalyzed Reactions. Experimental and theoretical study of chemical equilibria of izomerization and transalkylation of tert-amylbenzenes. The Journal of Physical Chemistry. B. 2009;**113**:12704

[40] Verevkin SP, Emel'yanenko VN, Toktonov AV, Leolko AS, Duwensee J, Kragl U, Sarge SM. Thermochemical and Ab initio studies of biodiesel fuel surrogates: 1,2,3-propanetriol triacetate, 1,2-ethanediol diacetate, and 1,2-ethanediol monoacetate. Industrial and Engineering Chemistry Research. 2009;**48**:7388

[41] Gomes de Azevedo R, Esperança JMSS, Szydlowski J, Visak ZP, Pires PF, Guedes HJR, Rebelo LPN. Thermophysical and thermodynamic properties of ionic liquids over an extended pressure range:bmim NTf_2 and hmim NTf_2. Journal of Chemical Thermodynamics. 2005;**37**:888

[42] Bernhardt E, Finze M, Willner H. An efficient synthesis for tetracyanoborates by sinter processes. Zeitschrift für anorganische und allgemeine Chemie. 2003;**629**:1229

[43] Ignat'ev NV, Welz-Biermann U, Kucheryna A, Bissky G, Willner H. New ionic liquids with tris(perfluoroalkyl)trifluorophosphate (FAP) anions. Journal of Fluorine Chemistry. 2005;**126**:1150

[44] Tong B, Tan ZC, Meng CG, Cui LJ, Xiao G, Liu RB. Thermodynamic investigation of several natural polyols (IV): Heat capacities and thermodynamic properties of adonitol. Thermochimica Acta. 2010;**499**:117

[45] Tong B, Tan ZC, Wang SX. Low Temperature Heat Capacities and Thermodynamic Properties of 2-Methyl-2-butanol. Chinese Journal of Chemistry. 2008;**26**:1561

[46] Rupp J, Birringer R. Enhanced specific-heat-capacity (*Cp*) measurements (150-300 K) of nanometer-sized crystalline materials. Physics Review. 1987;**B 36**:7888

[47] Wang L. Ph.D. Thesis. Thermochemistry study of nanostructured materials, supervised by Prof.Tan ZC. Dalian, China: Dalian Institute of Chemical Physics, Chinese Academy of Sciences; 2001

[48] Wang L, Tan ZC, Meng SH, Liang DB, Li GH. Enhancement of molar heat capacity of nanostructured Al_2O_3 Nanoparticle. Journal of Nanoparticle Research. 2001;**3**:483

[49] Millar RW. The heat capacity at low temperatures of zinc oxide and of cadmium oxide. Journal of the American Chemical Society. 1928;**50**:2653

[50] Tschöpe A, Birringer R. Thermodynamics of nanocrystalline platinum. Acta Metallurgica Materialia. 1993;**41**:2791

[51] Shimate CH. Heat capacities at low temperatures of titanium dioxide (rutile and anatase). Journal of the American Chemical Society. 1947;**69**:218

[52] Boerio-Goates J, Li G, Li L, Walker TF, Parry T, Woodfield BF. Surface water and the origin of the positive excess specific heat for 7 nm rutile and anatase nanoparticles. Nano Letters. 2006;**6**(4):750

[53] Kelley KK. Specific heat of ZrO_2 at low temperatures. Industrial and Engineering Chemistry. 1944;**36**:377

[54] Wagner M. Structure and thermodynamic properties of nanocrystalline metals. Physics Review, B. 1992;**45**:635

[55] Busey RH, Giauque WF. The heat capacity of nickel from 15 to 300 K - entropy and free energy functions. Journal of the American Chemical Society. 1952;**74**:3157

[56] Martin DL. Tray type calorimeter for the 15-300 K temperature-range - copper as a specific-heat standard in this range. The Review of Scientific Instruments. 1987;**58**:639

[57] Fecht HJ. Thermodynamics of nano-grain boundaries. Materials Research Society Symposia Proceedings. 1991;**206**:587

Chapter 2

Calorimetry of Immersion in the Energetic Characterization of Porous Solids

Liliana Giraldo, Paola Rodríguez-Estupiñán and Juan Carlos Moreno-Piraján

Additional information is available at the end of the chapter

http://dx.doi.org/10.5772/intechopen.71051

Abstract

In order to study and understand the adsorption process in a liquid-solid interface, it is necessary to know both textural and chemical properties of the adsorbent. It is also important to know the behavior of the solid in a liquid medium, considering that the interaction can produce some changes in the texture and the electrochemical properties when the adsorbent is immersed in a solvent or a solution. The study of the influence of these properties in the adsorption process with techniques like immersion microcalorimetry can provide direct information on particular liquid–solid interactions. The parameter that is evaluated by immersion microcalorimetry is the immersion enthalpy, ΔH_{im}. Immersion enthalpy is defined as the energy change at temperature and pressure constants when the surface of the solid is completely immersed in a wetting liquid in which the solid is insoluble and does not react. The immersion calorimetry can be a versatile, sensitive and precise technique that has many advantages for the characterization of porous solids. The versatility of immersion microcalorimetry is because changes in surface area, surface chemistry, or microporosity will result in a change in immersion energy. The interactions solid-liquid can be physical or chemical type, the physical present a lower amount of energy than that generated when exist chemical interactions.

Keywords: calorimetry, calorimeters type, immersion enthalpy, solids characterization, energetic change

1. Introduction

The calorimetric technique has been used in the last decades in the areas of thermodynamics, solutions, materials, biochemistry and biology, not only to obtain important thermodynamic parameters such as the enthalpy, ΔH, and the heat capacity, Cp, of the considered processes.

The calorimetry is a useful analytical tool, in the case of complex substrates such as those involved in the cited areas [1]. As many of these studies carried out in solution, it is interesting to know the interactions of different solutes with the solvent and in this way extend the results obtained to systems that are more complex. Then, it is interesting to analyze the calorimetric works in which water acts as a solvent, and the study of the interactions of this with the various solutes.

The transfer of energy in the form of heat is involved in all natural processes and this arouses interest in its quantitative determination. Cavendish built the first calorimeter in 1720 to determine the heat of vaporization of water and specific heats of various substances. Its appearance is the beginning of a great variety of designs of calorimetric equipment, which realized by the most important researchers of that time like Lavoisier, LaPlace, Black and Irvine, Bunsen, Dulong and Petit, Euken and Nernst among others [2].

Due to the large number of systems, processes and conditions of interest, there is no single calorimeter model, so the diversity of these is very wide. Since the very emergence of calorimeters, a variety of equipment has been generated.

Parallel with the development of calorimeters, it was necessary to improve data capture systems, which led to the production of peripheral systems of high sensitivity and precision. With the development of the peripheral equipment, calorimeters were designed whose basic characteristic was the detection of small amounts of energy, which were called microcalorimeters [3].

The purposes and applications of calorimeters have broadened the field of study and concepts of calorimetry, and therefore of thermodynamics: the enthalpies of solution, combustion, mixing and vaporization are just some of the determinations that performed with this technique. In modern calorimetry, instruments have been developed to allow studies in biological systems, in what has been called BioCalorimetry. It is possible to measure and advance in the field of knowledge, in subjects such as thermally induced transitions in proteins, lipids, nucleic acids, determination of heat production by living cells and microorganisms [4]. Calorimetric measurements have special validity in this subdiscipline.

Calorimetry is used in so-called Surface Science, with which it can have access to the chemistry itself and the interactions of the molecules that are exposed to the surface. The composition of the surface at the atomic level can be defined by instrumental methods including X-ray techniques, infrared spectroscopy, NMR, among others; however, the characterization of surface chemistry of the solids finds in microcalorimetry a valuable technique. Processes such as adsorption, desorption, immersion, solubilization or solvation, mixing, chelation and others can follow and interpret by means of calorimetric techniques, directly and without too much cost. Certain fields have advanced so autonomously that they have a proper name like Immersion Calorimetry.

Leslie [5] in 1802 directs his research to the determination of surface areas whose results have led to develop versatile methods for the characterization of porous solids, especially in activated carbons, with the possibility of obtaining very precise information of polarity, hydrophobicity, active sites and other properties [6–8]. It is also possible to establish

relationships between the thermal pretreatment to which the porous solids are exposed with the enthalpy of immersion [9, 10], as well as being a useful tool in the characterization of functional groups.

The immersion calorimetry is based mainly on the models developed by Dubinin [11] in Russia and Stoeckli and Kraehnbuehl [12] in Switzerland, with which it is possible to determine the total area of activated carbons and other solids.

A description of the type of calorimetric instrumentation used in the characterization of porous solids will be made, the most important relationships for the description of the surface of the solids by means of enthalpic determinations will be established, and some applications of the determination of the enthalpies of immersion as a solid characterization parameter will be shown.

2. The calorimetric technique

Calorimetry is a technique of thermodynamic character that allows knowing the amount of energy that is transferred as heat in a certain process and is related to the energy content of the studied system. The determination of the amount of energy absorbed or produced by a system has been carried out for several centuries, so that the calorimetry is one of the oldest measurement procedures, which is associated with the change of a system [13].

With the increase in sensitivity and precision of the methods for measuring small amounts of energy, in the order of 10–100 mJ, such as those produced in the solid-gas and solid-liquid interaction the calorimetric techniques used with higher frequency. Calorimetry used too in different fields since they supply information complementary to the extensive studies of gas-phase adsorption isotherms (vapor) and in liquid phase.

Due to the wide number of systems, processes and conditions does not exist a unique calorimeter model. The calorimeters diversity is wide and its classification depends on different factors like: the form in which the measurement is carried out and the type of sensors that are used, the change that takes place in the calorimetric cell, the way in which the energy transport is performed and the system-surroundings operating conditions.

Taking into account the surrounding system operating condition, the calorimeters are classified commonly in adiabatic calorimeters, isoperibolic calorimeters, isothermal calorimeters and differential scanning calorimeters [14]. The aspects to be taken into account to perform the calorimetric determination are: the required precision, the working temperature, the amount of sample available, the magnitude of the energy involved, the duration of the experiment and the cost of the instrument.

2.1. Adiabatic calorimeter

Ideally, adiabatic calorimeters do not allow heat exchange between the cell and the surroundings. Three ways can be considered to achieve this goal:

1. When the heat generation is so fast, no appreciable amount can enter or leave the cell during the period in which the measurement is carried out.
2. In the case of separating the cell from the surroundings with a thermal resistance, R_T, infinitely large, so that the measuring system is as isolated as possible.
3. By means of external electronic controls that make the surrounding temperature as close as possible to that of the cell.

During the calorimetric experience, any heat generated or consumed in the cell lead to a temperature change, which is evaluated from a plot of temperature as a function of time. The heat can be calculated from the measurement of the temperature difference ΔT:

$$Q = Cp\Delta T \tag{1}$$

The heat capacity is easily determined by calibration with the use of electrical energy [15].

2.2. Isoperibolic calorimeter

An isoperibolic calorimeter keeps constant the surrounding temperature by using a thermostat, while the temperature of the measuring system may vary over time. There is a thermal resistance, R_T, of magnitude defined between the surroundings and the cell where the measurement is made, so that the heat exchange depends on its temperature difference.

T_A is the surrounding temperature and T_C is the cell temperature and measurement system. Since T_A is constant then the heat flux is a C_T function.

The decrease in T_C depends on the insulation of the cell that defines the thermal leakage constant, Kft, calorimeter's parameter and also a function of the temperature gradient.

The amount of heat for the process under consideration is equal to:

$$Q = Cp\,\Delta T_{corrected} \tag{2}$$

where Cp is the heat capacity of the studied system plus the heat capacity of the cell, $\Delta T_{corrected}$ is the temperature difference on which a correction is made for small but existing heat leaks [16].

2.3. Isothermal calorimeter

Another way of performing the measurement of the energy involved in a process is in which there is a large exchange of heat that is produced in the cell with the surroundings; this is an isothermal nature method, in which the surroundings and the cell have the same constant temperature ($T_A = T_C$ = constant).

The isothermal calorimeter has a small thermal resistance R_T, and the heat capacity of the surroundings is infinitely large. If these requirements are taken into account, in strictly

isothermal conditions, T_A and T_C can remain constant in time and space, but then no heat flow occurs. In real cases, there is a heat flow between the cell and the surroundings, a flow that is detected by means of the thermal sensors placed between them. The flow is due to the generally small temperature difference between T_A and T_C during the occurrence of the observed process; the magnitude of this temperature difference depends on the amount of heat released per unit time, the thermal conductivities, the cell geometry and the type of insulation that the thermal sensors possess. In spite of these limitations, the isothermal designation is commonly used for calorimeters where the temperatures T_A and T_C may be different from each other, but each of them considered separately is constant throughout the time of occurrence of the process that generates the heat flow [17]. In **Figure 1**, a temperature curve as a function of time obtained with an isothermal calorimeter is presented, the conduction of heat to the surroundings is observed by the drop in temperature after the supply of a heat pulse to the cell.

The cell is connected to the surroundings by means of a thermal resistance R_T, which is an interesting parameter because it relates the heat flow dQ/dt to the temperature difference. The temperature difference in the thermal resistance is:

$$\Delta T = T_c - T_A \tag{3}$$

and in the steady state this relation is presented:

$$\frac{dQ}{dT} = \frac{\Delta T}{R_T} \tag{4}$$

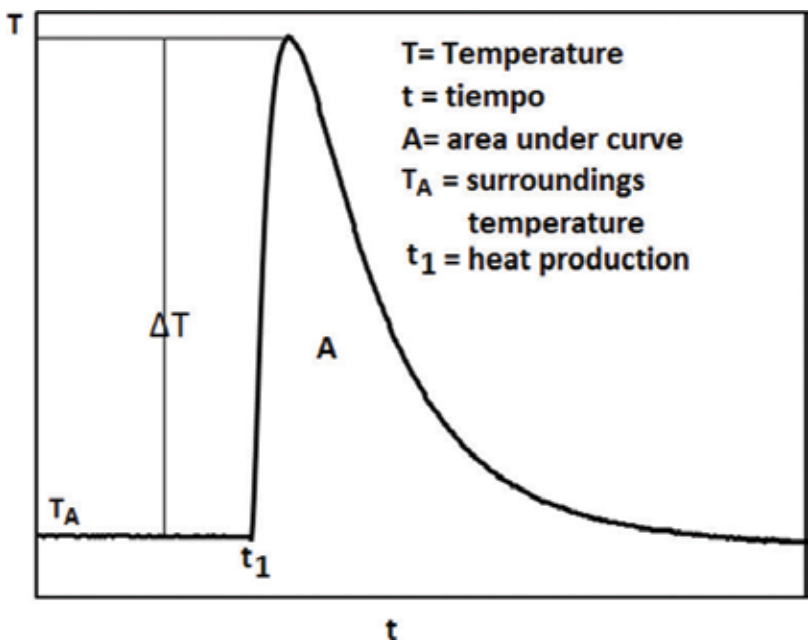

Figure 1. Temperature curve as a function of time for an isothermal calorimeter.

integrating Eq. (4) is obtained:

$$Q = \frac{1}{R_T}\int \Delta T(t)dt \tag{5}$$

For the same amount of heat:

$$\int \frac{\Delta T(t)dt}{R_T} = constant \tag{6}$$

Due to the complex nature of the heat conduction within a real instrument, it is generally impossible to calculate the R_T resistance, which quantitatively connects the measured temperature difference with the corresponding heat flow; for this reason, the resistance must be determined by calibration. The reciprocal value of the thermal resistance is the calibration factor K (t)

$$Q = K\int \Delta T(t)dt \tag{7}$$

In many cases, the calibration factor K can record as constant in the temperature range in which carry out the process.

2.4. Temperature scanning calorimeter

In this type of calorimeter, a constant temperature change of the surroundings is carried out which is reflected in the measuring cell with a certain delay that depends on the magnitude of the thermal resistance R_T between the system and the surroundings.

The surrounding temperature will be equal to:

$$T_S = T_{S_{init}} + \beta t \tag{8}$$

where T_S and T_{Sinit} are the surrounding temperature and the initial surrounding temperature respectively, β is the rate of change in temperature and t is the time. This form of operation is the one used in differential scanning calorimeters [18].

3. Application of the enthalpy of immersion in the characterization of activated carbon

The work that shown below uses an isothermal heat conduction calorimeter with thermopiles as heat flux sensors and measures the interaction energy that occurs when activated carbon immersed in water and in aqueous solutions of Cd (II) and Ni (II) [19].

3.1. Relationship between the enthalpy of immersion and the porous solid surface

The immersion calorimetry is a technique of thermodynamic character that allows to evaluate the thermal effects that result to put in contact a solid with a liquid and thus to know the heat involved in the interactions that are established and express it like the enthalpy of immersion ΔH_{im}. [20]. The interactions may be of specific or non-specific type and the magnitude of the heat generated depends on the intensity of the interaction [21].

The thermal effects resulting from immerse a solid in a non-polar solvent such as benzene are related to the formation of a layer of molecules on the solid and therefore with surface parameters, as shown by the model developed by Dubinin and Stoeckli, that for a microporous solid, defines the enthalpy of immersion as [22]:

$$\Delta H_{im}(T) = \int_0^1 q^{ne}(T, \theta) d\theta \tag{9}$$

where q^{net} is the heat of adsorption.

Stoeckli established the relationship between the enthalpy of immersion of activated carbon in various organic liquids and the parameters obtained by the adsorption of vapors of the same liquids on the solid. This relation is described by the equation of Stoeckli and Krahenbüehl [23]:

$$-\Delta H_{im} = \frac{\beta E o W o \sqrt{\pi}(1 + \alpha T)}{2Vm} \tag{10}$$

where ß is the affinity coefficient of the adsorbate, E_o is the characteristic free energy for the adsorption of the reference vapor, W_o is the total volume of micropores of the solid, α is the thermal expansion coefficient of the adsorbate at temperature T and V_m is the molar volume of the liquid.

When the above equation is applied directly to activated carbons, which have a small external surface, the experimental enthalpy, ΔH_{exp}, also contains a contribution due to the external surface (S_{ext}).

$$\Delta H_{exp} = \Delta H_{im} + h_i S_{ext} \tag{11}$$

where h_i, is the specific immersion enthalpy to non-porous open surface. From the above equation, the total area can be calculated as:

$$A_{Total} = A_{microp} + S_{ext} \tag{12}$$

Stoeckli et al. use this technique to characterize the porous structure of a wide variety of carbonaceous materials taking a non-porous carbon black as a reference, assuming that the immersion enthalpy per surface area is proportional to the available surface to the immersion liquid [24].

The immersion enthalpy of a solid in different liquids is usually different, therefore the magnitude of the immersion enthalpy will depend on [25]:

1. The extent of the surface area of the solid, thus for a solid–liquid system, the immersion energy is increased with the surface area of the solid. If calorimetry of immersion is performed with liquids of different molecular size but similar chemical nature, it is possible to obtain an approximation to pore size distribution.
2. The chemical nature of the surface and the immersion liquid: if the liquid is polar the immersion energy increases with the polarity of the chemical functions on the surface of the solid. This information is useful to evaluate the influence of modification treatments of the surface chemistry, such as oxidation and heat treatments, the polarity and the hydrophobic character of the surface.

Water immersion calorimetry allows evaluate the polarity of the activated carbon surface under the assumption that water molecules interact mainly with the oxygenated surface groups located at the polar sites at the edges of the graphene layers [26]. It has even been found that the enthalpy of immersion increases linearly with the concentration of the acidic sites present on the surface of the solid [27].

3.2. Application: Activated carbons modified in their surface chemistry. Immersion in water and aqueous solutions of Cd (II) and Ni (II)

A granular activated carbon prepared from coconut shell (CAG), is modified in its surface chemistry to obtain seven solids with different characteristics. Immersion enthalpies in water and aqueous solutions of Ni (II) and Cd (II) were determined, this with the purpose of establishing the differences in the energetic interactions of the solids with the liquids and the influence that shows the superficial chemistry of the activated carbons in the values of the enthalpies of immersion.

3.2.1. Materials and methods

A series of activated carbons are obtained of a granular activated carbon prepared from coconut shell (CAG) which is oxidized with a solution of 6 M nitric acid (CAGoxN) and 10 M hydrogen peroxide (CAGoxP). Two portions of each oxidized activated carbon were treated at 450°C (CAGoxN450 and CAGoxP450) and 750°C (CAGoxN750 and CAGoxP750) under nitrogen atmosphere and a final activated carbon was obtained by heating the starting activated carbon at 900°C (CAG900) [28].

3.2.1.1. Textural characterization

Textural parameters of surface area and pore volume of the activated carbons evaluate by physical adsorption of N_2 at −196°C and CO_2 at 0°C in an Autosorb 3B automatic equipment, Quantachrome. The apparent surface area and the micropores volume determine by the Brunauer-Emmet-Teller (BET) and Dubinin-Radushkevich models respectively.

3.2.1.2. Chemical characterization

3.2.1.2.1. Total acidity and basicity

The total acidity and basicity of the activated carbons evaluate by the Boehm method [29]. 1000 g of each sample weighed and 50 mL of a 0.1 M NaOH solution was added to determine the acidity, or 50 mL of a 0.1 M HCl solution to determine the basicity, considering that in each mixture the acid and basic groups present on the surface of the activated carbon are neutralized. The mixtures maintained at a temperature of 298 K and constant agitation for 5 days, at the end of this equilibrium time taken a 10 mL aliquot of each supernatant liquid and titrated with a previously standardized NaOH or HCl solution, as appropriate.

3.2.1.2.2. Point of zero charge

The determination of the pH at the point of zero charge, pH_{PZC}, evaluated by the mass titration method [30], by weighing different amounts of activated carbon between 10 and 600 mg,

placed in glass containers with 10 mL of a 0.1 M solution of NaCl. The mixtures were maintained at 298 K and constant stirring for 2 days. The pH of each solution was then measured with a Schott pH 840B pH meter.

3.2.1.2.3. Determination of immersion enthalpies

The enthalpies of immersion of the activated carbons in water and aqueous solutions of Ni (II) and Cd (II) of 500 mg L^{-1} were determined in a heat conduction microcalorimeter that has thermopile as heat flow sensors and a cell in stainless steel with a capacity of 15 mL, in which 10 mL of the immersion liquid is placed.

Weighed 100 mg of each activated carbon in a glass ampoule fitted in the calorimeter cell and captured the electric potential of the thermopiles for about 40 minutes until obtained a stable baseline. Then the immersion of the sample is performed recording the potential increase caused by the wetting of the solid, it is waited until it is returned to the baseline and the electrical calibration is carried out [31].

3.2.2. Results and discussion

Table 1 shows the results obtained for the textural characterization of the obtained carbons, which indicates the changes that occur in these characteristics by the chemical and thermal treatments that were made to the solids.

The results presented are: the surface area calculated by the BET model, the micropore volume (W_o) estimated by the DR model and the mesopore volume (Vmeso). The narrow microporosity (V_n) of the materials was evaluated by applying the DR model to the experimental data obtained from the CO_2 adsorption isotherm.

The results obtained show that the activated carbon exposed to the oxidation treatment with nitric acid, CAGoxN, presents a decrease in the surface area and in the micropore volume (Wo), with respect to the starting activated carbon. This behavior is due to the treatment of oxidation, which favors the formation of oxygenated surface groups that are located at the edges of pore apertures, which limits the accessibility of the nitrogen molecule to porous structures [32].

Activated carbon	N_2			CO_2
	Surface area BET (m^2 g^{-1})	V_0 (cm^3 g^{-1})	V_{Meso} (cm^3 g^{-1})	V_n (cm^3 g^{-1})
CAG	842	0.34	0.04	0.35
CAG900	876	0.35	0.05	0.28
CAGoxN	816	0.32	0.05	0.38
CAGoxN450	903	0.35	0.05	0.37
CAGoxN750	935	0.37	0.05	0.35
CAGoxP	873	0.35	0.04	0.36
CAGoxP450	783	0.31	0.03	0.32
CAGoxP750	888	0.35	0.04	0.34

Table 1. Textural characteristics of the activated carbons determined from the N_2 and CO_2 isotherms at −196 and 0°C.

According to studies reported the groups developed are acid carboxylic and carbonyl type, besides in the solids modification with solutions of HNO_3 occurs the collapse of porous structures, this latter effect explains the increase in the mesoporosity volume.

In the oxidized activated carbon with hydrogen peroxide, an increase in the surface area near 7.0% with respect to the sample CAG is observed, since in addition to the process of oxygenated surface formation there is also the opening of porous structures [33].

The thermal treatments on the activated carbon, which produce the decomposition of oxygenated groups, show changes in the surface area values, an increase for the CAGoxN sample a decrease for CAGoxP, and an increase for the higher temperature.

Table 2 presents the results obtained for total acidity and basicity and for pH at the point of zero charge, which reflects the changes that occur in the surface of the activated carbon with the different processes.

Oxidation with HNO_3 and H_2O_2 solutions produces the formation of surface functional groups, with regard to the oxidation process with nitric acid is more effective in the formation of acid groups on the surface of the activated carbon [34], the increase of these groups is close to triple, with respect to the original sample. Hydrogen peroxide has a smaller effect on the reduction of the basic character of the surface, this leads to an increase in pH_{PZC}, which is 6.2 for the CAGoxP sample.

Once the activated carbon is characterized, the immersion calorimetry is carried out in order to obtain the enthalpies of immersion, ΔH_{im}, of the activated carbon in water. This solvent interacts with the surface oxygenated groups of the solids and it has wanted to show how the differences obtained in the surface chemistry of the solids are reflected in the thermal curves of electric potential as a function of time for each set of activated carbons. **Figure 2** shows the thermal curves obtained for the immersion of CAG and CAG900 activated carbons in water.

As the area under the potential as a function of time curve is proportional to the heat generated in the immersion of the solid in the liquid. It is observed that the activated carbon

Activated carbon	Total acidity (molecules/nm^2)	Total basicity (molecules/nm^2)	pH_{PZC}
CAG	0.141	0.065	5.4
CAG900	0.032	0.191	8.9
CAGoxN	0.290	0.036	3.4
CAGoxN450	0.179	0.069	7.9
CAGoxN750	0.039	0.172	8.2
CAGoxP	0.204	0.073	6.2
CAGoxP450	0.126	0.197	7.2
CAGoxP750	0.058	0.201	8.7

Table 2. Chemical characterization of activated carbons.

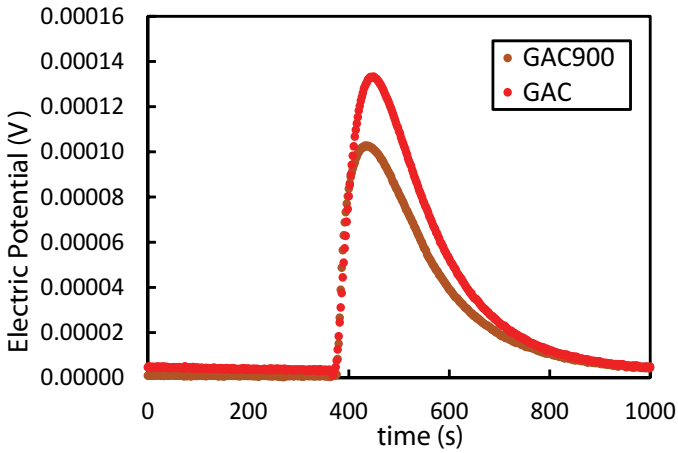

Figure 2. Thermal curves of the immersion of CAG and CAG900 activated carbons in water.

CAG900, that has been exposed to a thermal process at 900°C in which a large part of the surface groups are removed and with respect to the starting carbon shows an increase in pH_{PZC}, exhibits a smaller peak because the interactions of the water with the surface of this activated carbon decrease.

In immersion calorimetry, benzene is the reference solvent because its affinity coefficient, β, is defined as 1. The benzene to be a non-polar solvent presents different energetic behavior with activated carbons compared to water, by showing a greater interaction with the activated carbon that has a lower content of surface oxygenated groups and a smaller interaction with the solids that have been oxidized. **Figure 3** presents the curves obtained for the immersion of activated carbon CAG900 and CAGoxN in benzene.

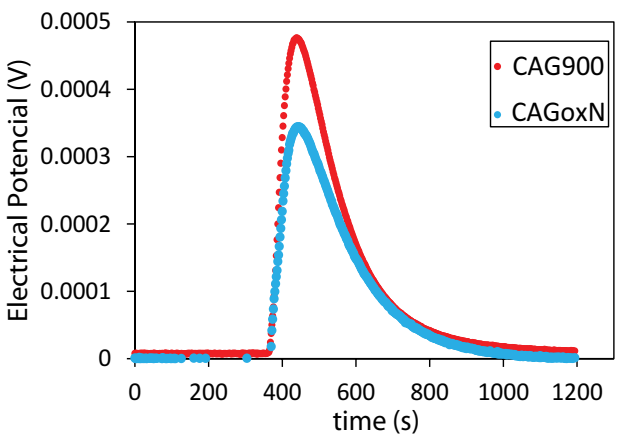

Figure 3. Thermal curves of the immersion of CAG900 and CAGoxN activated carbons in benzene.

Figure 4 shows the electrical potential as a function of time curves obtained when CAGoxN, CAGoxN450 and CAGoxN750 are immersed in water. This Figure show the following trend: the highest peak occurs for activated carbon oxidized with nitric acid, which has the uppermost content of oxygen groups and therefore the highest interaction with water and provides information of the energy manifested between the surface and the polar molecules of water.

Oxidized activated carbons with nitric acid solution and subsequently exposed to thermal treatments selectively lose oxygenated groups, as is known by some works about surface chemistry of activated carbons [35], and therefore the interactions with water are smaller as may be observed in thermograms.

In **Figure 5**, present the themal curves for the other group of activated carbons oxidized. These solids were oxidized with hydrogen peroxide solution and heat treatment at 450 and 750°C.

The result obtained is comparable, in the trend, to the previous one since the oxidized activated carbon shows the highest interaction and it's followed by the activated carbon treated at the intermediate temperature and finally the lowest effect is obtained for the sample being treated at the highest temperature.

Observe that the group of activated carbons oxidized with HNO_3 solution present greater effects than those oxidized with H_2O_2 solution and it makes a difference in how the oxygenated groups are generated on the surface of the activated carbon.

The activated carbons obtained are used for the adsorption of Ni (II) and Cd (II) ions from aqueous solution, the ions adsorption on the surface of the activated carbons also produces a thermal effect that can be evaluated by calorimetry. Calorimetry allows calculating the total amount of heat generated in the process. For case of the activated carbon immersion in the aqueous solutions of the ions, the thermal effect obtained corresponds to the summation of several interactions as the wetting of the surface by the solvent, the solvent the interaction

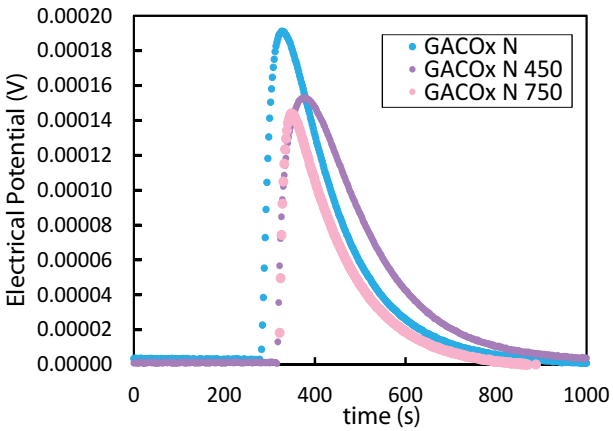

Figure 4. Thermal curves of the immersion in water of activated carbons of the oxidized series with nitric acid solution.

with the chemical groups of the surface, the interaction of the ions with the surface and their groups, among others.

Figure 6 shows the thermal curves obtained for the immersion of the activated carbon in aqueous solutions of Ni (II) ion, for the solids with the lowest and the highest adsorption of the ion. The CAGoxN activated carbon has a higher peak in the potential curve as a function of time when it is brought into contact with the 500 mg L^{-1} solution, indicating that the ion present in the liquid produces a greater thermal effect. Tis effect relates the interaction of the ions with the oxygenated groups of the surface, since in the immersion of the activated carbon CAG900 in which diminished the content of surface groups, the thermal effect is considerably smaller.

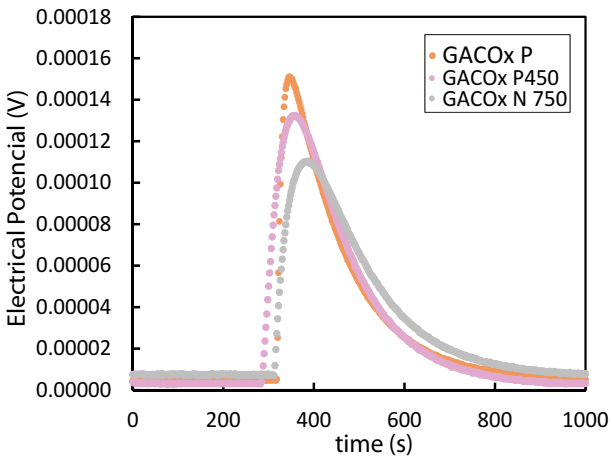

Figure 5. Thermal curves for the immersion of the activated carbon group oxidized with hydrogen peroxide solution in water.

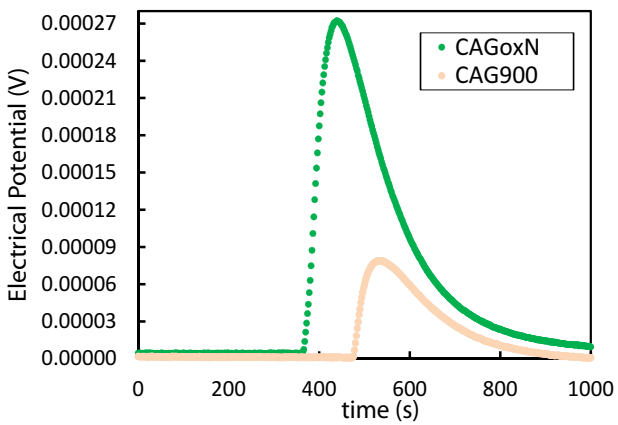

Figure 6. Thermal curves for the immersion of the activated carbon CAG900 and CAGoxN in aqueous solution of 500 mg L^{-1} of Ni (II).

Figure 7 shows the thermal curves obtained for the immersion of the CAGoxP and CAG900 activated carbons in a solution of 500 mg L^{-1} of Cd (II), for these activated carbons the highest and lowest adsorption of the Cd (II) ion are obtained, respectively. For the immersion of CAGoxP, a larger peak is observed indicating that there is a greater effect between the solid and the solution, and that the surface chemistry of activated carbon has an influence on the generation of a quantity of heat produced by the interaction between them.

Once the immersion calorimetry of the different activated carbons into the described immersion liquids is carried out, the enthalpies of immersion are calculated. The results present in **Table 3**, which shows the enthalpies in water and aqueous solutions of 500 mg L^{-1} of Ni (II) and Cd (II) for the original activated carbon, the reduced and the two oxidized activated carbons.

It is interesting to observe the values of the immersion enthalpies obtained, since they can related to the change that was caused to the surface chemistry of the activated carbon. Because the two oxidizing agents and the interaction of the two ions with the surface is different, it

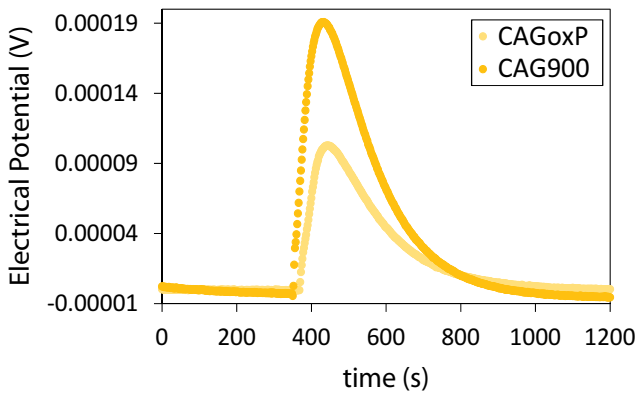

Figure 7. Thermal curves for the immersion of CAG900 and CAGoxN activated carbons in aqueous solution of 500 mg L^{-1} of Cd (II).

Activated carbon	$-\Delta H_{im}$ in H_2O (J g^{-1})	$-\Delta H_{im}$ in Ni (II) solution (J g^{-1})	$-\Delta H_{im}$ in Cd (II) solution (J g^{-1})
CAG	49.65	49.96	34.42
CAG900	32.39	37.50	34.40
CAGoxN	66.59	67.17	52.96
CAGoxP	56.42	45.64	57.73

Table 3. Enthalpies of immersion of activated carbons in different liquids.

opens the possibility of conducting studies between immersion enthalpies into the solutions of ions and contents of specific groups produced on the surface.

Immersion enthalpies can relate to the textural and chemical characteristics of the activated carbon. **Figure 8** shows the relationship between the enthalpy of immersion of activated carbons in benzene and the micropore volume, that is one of the frequent representations for these characterization parameters, and for microporous activated carbons is directly proportional [36].

Observe, as a general trend, that when the micropore volume increases the immersion enthalpy increases too. As made a modification on the surface chemistry of the solid, several of the activated carbons keep the micropore volume and the values obtained for the enthalpies of immersion of the activated carbons in benzene are consistent with the chemical changes that occur.

Can to say for the activated carbon CAG900 with a micropore volume of 0.35 $cm^3\ g^{-1}$ that the greater immersion enthalpy value is generated because this is the most hydrophobic solid. Then it will have a greater interaction with benzene, and the activated carbon CAGoxN450, which has the same micropore volume value has the lower value of enthalpy of immersion in benzene since it has a higher content of oxygenated groups.

Finally, the immersion enthalpies of the set of activated carbons in the non-polar solvent benzene, and the polar solvent water, with the pH of each solid at the point of zero charge are reported, which is shown in **Figure 9**.

It is observed that when pH_{PZC} increases, the immersion enthalpy in benzene increases because when the content of oxygenated groups decreases the basicity of the activated carbons increases as well as its hydrophobic character; in contrast, when the content of oxygenated groups increases, so does the acidity and the interactions with water manifested in the enthalpy of immersion.

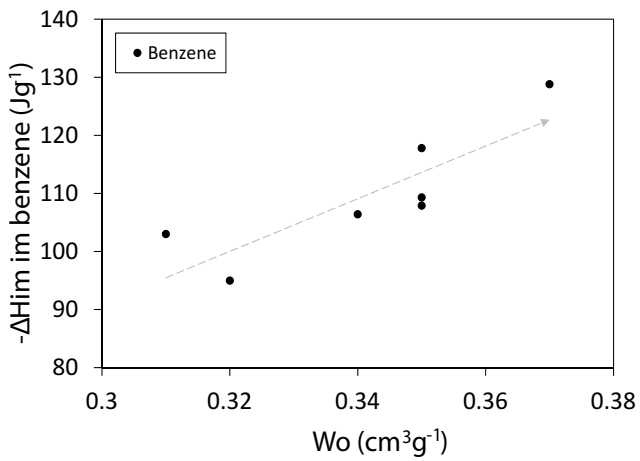

Figure 8. Enthalpy of immersion of the activated carbons in benzene as a function of the micropore volume.

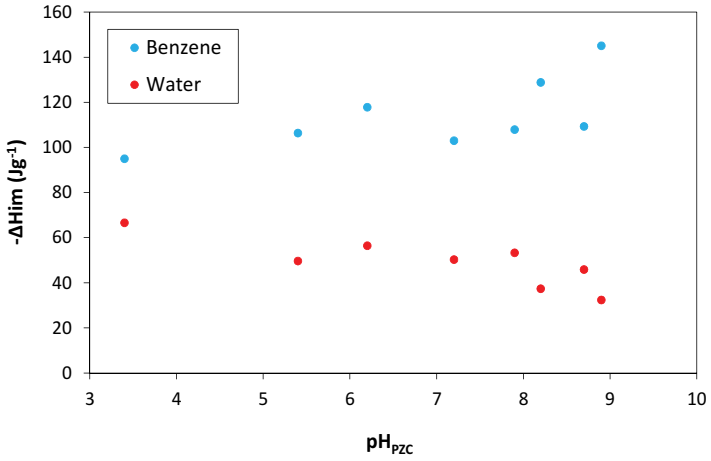

Figure 9. Enthalpy of immersion of activated carbons in benzene and water as a function of pH at the point of zero charge.

4. Conclusions

Activated carbons obtained from a granular activated carbon by oxidation of its surface with solutions of nitric acid and hydrogen peroxide and subsequent heat treatment, the solids obtained have surface areas between 783 and 935 $m^2\ g^{-1}$.

The treatment with nitric acid mainly favors the formation of acidic groups, specifically carboxylic groups, obtaining a density of these groups of 0.197 molecules/nm^2. In addition, it causes a decrease in the parameter of basicity, in contrast, the treatment with hydrogen peroxide favors the formation of phenolic groups (0.075 molecules/nm^2) and its effect on the decrease of the basicity parameter is smaller.

Modified the point of zero charge of the solids by the change in the concentration of the surface groups promoted by each treatment, a greater amount of acid groups as in the case of the sample GACoxN produces an acid pH_{PZC}, in this case 3.4.

The immersion enthalpies in water and the total acid and basic surface groups content present a relation and show that these values are influenced by the interactions of the oxygenated surface groups and basic groups free of oxygen.

The enthalpies of immersion of the activated carbons in the solutions of the electrolytes show that these enthalpies were larger for the GACoxN-Ni (II) and GACoxP-Cd (II) systems, evidencing the affinity and selectivity of the solids by the respective ions.

Acknowledgements

The authors thank the Framework Agreement between the Universidad de los Andes and the Universidad Nacional de Colombia and the act of agreement established between the Chemistry Departments of the two universities.

The authors also thank the Faculty of Sciences of Universidad de los Andes for the partial funding through the call "short projects / additional product." and to DIEB of Universidad Nacional de Colombia Project 37348.

Author details

Liliana Giraldo[1]*, Paola Rodríguez-Estupiñán[2] and Juan Carlos Moreno-Piraján[2]

*Address all correspondence to: lgiraldogu@unal.edu.co

1 Faculty of Sciences, Department of Chemistry, Research Group on Porous Solids and Calorimetry, Andes University, Bogotá, Colombia

2 Faculty of Sciences, Department of Chemistry, National University of Colombia, Bogotá, Colombia

References

[1] Rouquerol J, Rouquerol F. Adsorption at the liquid–solid interface: Thermodynamics and Methodology. In: Adsorption by Powders and Porous Solids Principles, Methodology and Applications. 2nd ed. Oxford: Academic Press; 2014. p. 106-132. DOI: 10.1016/B978-012598920-6/50002-6

[2] Wilhoit RC. Recent developments in calorimetry. Part 1. Introductory survey of calorimetry. Journal of Chemical Education. DOI: 10.1021/ed044pA571

[3] Bäckman P, Bastos M, Hallén D, Wadsö I. Heat conduction calorimeters: time constants, sensitivity and fast titration experiments. Journal of Biochemical and Biophysical Methods. DOI: 10.1016/0165-022X(94)90023-X

[4] Türker M. Development of biocalorimetry as a technique for process monitoring and control in technical scale fermentations. Thermochimica Acta. DOI: 10.1016/j.tca.2004.01.036

[5] Bansal RC, Goyal M, editors. Activated Carbon Adsorption. London: Taylor & Francis Group; 2005. p.164. DOI:10.1201/9781420028812

[6] Rodríguez RF, Molina-Sabio M. Textural and chemical characterization of microporous carbons. Advances in Colloid and Interface Science. DOI: 10.1016/S0001-8686(98)00049-9

[7] Tansel B, Nagarajan P. SEM study of phenolphthalein adsorption on granular activated carbon. Advances in Environmental Research. DOI: 10.1016/S1093-0191(02)00126-0

[8] Burg P, Cagniant D. Characterization of carbon surface chemistry. In: Chemistry and Physics of Carbon. New York: Taylor & Francis Group; 2008. p. 29-172. DOI: 10.1201/9781420042993

[9] Vargas DP, Giraldo L, Moreno JC. Calorimetric study of the CO_2 adsorption on carbon materials. Journal of Thermal Analysis and Calorimetry. DOI: 10.1007/s10973-014-3909-x

[10] Dıaz E, Ordonez S, Vega A, Coca J. Evaluation of adsorption properties of zeolites using inverse gas chromatography: Comparison with immersion calorimetry. Thermochimica Acta. DOI: 10.1016/j.tca.2005.01.014

[11] Dubinin MM, Polyakov NS, Kataeva LI. Basic properties of equations for physical vapor adsorption in micropores of carbon adsorbents assuming a normal micropore distribution. Carbon. DOI: 10.1016/0008-6223(91)90111-U

[12] Stoeckli HF, Kraehnbuehl F. The enthalpies of immersion of active carbons, in relation to the Dubinin theory for the volume filling of micropores. Carbon. DOI: 10.1016/0008-6223(81)90059-2

[13] Wadso I. Isothermal microcalorimetry near ambient temperature: An overview and discussion. Thermochimica Acta. DOI: 10.1016/S0040-6031(96)03136-X

[14] Sarge SM, Hohne GWH, Hemminger W. Calorimetry. Fundamentals, Instrumentation and Applications. Winheim. Germany: Wiley-VCH; 2014. p. 9-18. DOI: 10.1002/97835 27649365

[15] Wadso I, Goldberg RN. Standards in isothermal microcalorimetry. Pure and Applied Chemistry. DOI: 10.1351/pac200173101625

[16] Moreno JC, Giraldo L. Influence of thermal insulation of the surroundings on the response of the output electric signal in a heat conduction calorimetric unit. Instrumentation Science & Technology. DOI: 10.1081/CI-200063709

[17] Zielenkiewicz W. Comparative measurements in isoperibol calorimetry: Uses and misuses. Thermochimica Acta. DOI: 10.1016/S0040-6031(99)00425-6

[18] Hohne GWH, Hemminger W, Flammersheim HJ. Differencial Scanning Calorimetry. An Introduction for Practitioners. 1st ed. Berlin: Springer; 1996. DOI: 10.1007/978-3-662-03302-9

[19] Rodríguez-Estupiñán P, Gómez F, Giraldo L, Moreno-Piraján JC. Immersion enthalpies in different liquids of activated carbons modified by surface chemistry. Materials Express. DOI: 10.1166/mex. 2015.1235

[20] Moreno-Pirajan JC, Giraldo L. Determination of the immersion enthalpy of activated carbon by microcalorimetry of the heat conduction. Instrumentation Science and Technology. DOI: 10.1081/CI-100100970

[21] Taraba B, Zelenka T. Study of micropores accessibility in coals and activated carbon using immersion heats with C1–C4 alkanols. Journal of Thermal Analysis and Calorimetry. DOI: 10.1007/s10973-016-6041-2

[22] Stoeckli F, Centeno TA. On the characterization of microporous carbons by immersion calorimetry alone. Carbon. DOI: 10.1016/S0008-6223(97)00067-5

[23] Moreno JC, Giraldo L. Instrumentación calorimétrica aplicada a la determinación de entalpias de inmersión de sólidos porosos. In: Sólidos porosos preparación, caracterización y aplicaciones. Bogotá: Ed. Uniandes; 2007. p. 281-297. DOI: 101007/s 10973-006-7524-3

[24] Barroso-Bogeat A, Alexandre-Franco M, Fernandez-Gonzalez C, Gomez-Serrano V. Physico-chemical characterization of activated carbon-metaloxide photocatalysts by immersion calorimetry in benzene and water. Journal of Thermal Analysis and Calorimetry. DOI: 10.1007/s10973-016-5337-6

[25] Madani SH, Silvestre-Albero A, Biggs MJ, Rodríguez-Reinoso F, Pendleton P. Immersion calorimetry: Molecular packing effects in micropores. ChemPhysChem. DOI: 10.1002/cphc.201500580

[26] Madani SH, Hu C, Silvestre-Albero A, Biggs MJ, Rodríguez-Reinoso F, Pendleton P. Pore size distributions derived from adsorption isotherms, immersion calorimetry, and isosteric heats: A comparative study. Carbon. DOI: 10.1016/j.carbon.2015.10.072

[27] Rodríguez P, Giraldo L, Moreno JC. Modified surface chemistry of activated carbons. Correlation with immersion enthalpy. Journal of Thermal Analysis and Calorimetry. DOI: 10.1007/s10973-012-2932-z

[28] Rodríguez P, Giraldo L, Moreno-Piraján JC. Energetic changes in the surface of activated carbons and relationship with Ni (II) adsorption from aqueous solution. Applied Surface Science. DOI: 10.1016/j.apsusc.2013.09.085

[29] Boehm HP. Some aspects of the surface chemistry of carbon blacks and other carbons. Carbon. DOI: 10.1016/0008-6223(94)90031-0

[30] Mohamed FS, Khater WA, Mostafa MR. Characterization and phenol sorptive properties of carbons activated by sulfuric acid. Chemical Engineering Journal. DOI: 10.1016/j.cej.2005.10.015

[31] Giraldo L, Moreno-Pirajan JC. Calorimetric determination of activated carbons in aqueous solutions. Journal of Thermal Analysis and Calorimetry. DOI: 10.1007/s10973-006-7524-3

[32] Bandosz T, Ania C. Surface chemistry of activated carbons and its characterization. In: Activated Carbon Surfaces in Environmental Remediation Activated Carbon Surfaces in Environmental Remediation. New York: Elsevier; 2006. p. 75. DOI: 10.1016/j.jcis.2006.03.032

[33] Ridder DJ, Verliefde ARD, Schoutteten B, Van der Linden B, Heijman SGJ, Beurroies I, Denoyel R, Amy GL, Van Dijk JC. Relation between interfacial energy and adsorption of organic micropollutants onto activated carbon. Carbon. DOI: 10.1016/j.carbon.2012.10.042

[34] Vocciante M, Trofa M, Rodríguez-Estupiñán P, Giraldo L, D'Auria T, Moreno-Piraján JC, Erto A. A rigorous procedure for the design of adsorption units for the removal of cadmium and nickel from process wastewaters. Journal of Cleaner Production. DOI: /10.1016/j.jclepro.201312.001

[35] Mezohegyi G, Van der Zee F, Font J, Fortuny A, Fabregat A. Towards advanced aqueous dye removal process: A short review on the versatile role of activated carbón. Journal of Environmental Management. 2012;**102**:148-164

[36] Giraldo L, Moreno-Piraján JC. Relation between immersion enthalpies of activated carbons in different liquids, textural properties, and phenol adsorption. Journal of Thermal Analysis and Calorimetry. DOI: 10.1007/s10973-014-3940-y

Chapter 3

"Tie Calorimetry" as a Tool for Determination of Thermodynamic Parameters of Macromolecules

Armen T. Karapetyan and Poghos O. Vardevanyan

Additional information is available at the end of the chapter

http://dx.doi.org/10.5772/intechopen.71313

Abstract

Determination of free energy of double helix formation from two single-stranded polynucleotides and estimation of energetics of different low-molecular compounds binding to nucleic acids provide valuable tools for understanding of mechanisms that govern noncovalent binding of ligands to their receptor targets. In order to completely understand the molecular forces that drive and stabilize double helix formation and its complexes with ligands, thermodynamic studies are needed to complement the structural data. Structural characterization of a number of DNA-ligand complexes by X-ray and high-resolution NMR method provides key insight relating to the properties of complex formation, but structural data alone, even when coupled with the most sophisticated current computational methods, cannot fully define the driving forces for binding interactions (or interac-tions) or even accurately predict their binding affinities. Thermodynamics provides quantitative data of use in elucidating these driving forces and for evaluating and understanding at a deeper level the effects of substituent changes on binding affinity.

Keywords: free energy, double helix, helix-coil transition, transition thermodynamic parameters, DNA-ligand complexes, binding parameters

1. Introduction

The 3D structure of solids by the change of environmental conditions may convert to a phase with quite different physical parameters describing the resulting state of matter. Transitions from one phase to another are accompanied by absorption or release of heat and sharply defined changes of energetic characteristics of the matter. At the fifties of last century, the biologically important molecules, nucleic acids and proteins, have been discovered — the structures of which were like one-dimensional linear aperiodic crystals [1]. The phase transition

in linear crystals was theoretically treated at the twenties of last century [2]. According to this theory, the thermodynamic equilibrium is impossible for two homogeneous phases sharing common frontiers. Proper demonstration of the theorem efficacy was given much later, when the linear crystal to coil (helix-coli) transition of proteins and nucleic acid was investigated [3].

The unique feature of nucleic acid chains is their folding manner that encloses functional groups, i.e., purine and pyrimidine bases, so as to protect them inside a rigid and monotonous double-helix structure. At present, it is well established that DNA, the "major" molecule in the living cells, is polymorphous, and while functioning, the biopolymer may be in several forms: B-, A-, Z-, coil, etc., of which only Z-form was found to be a left-handed helix [4, 5]. There are two different types of structural transitions in DNA one of which (helix-coil, A-coil, Z-coil) is accompanied by unwinding of double helix (translation and replication, etc.). The second type of transitions (B-B^1, B-Z, B-A, A-Z, etc.) is realized by certain structural changes in sugar-phosphate backbone and base-pairs (bp) of DNA without unwinding the helix of the biopolymer. To understand the biological role of the existence of various forms of DNA, it is important to know the thermodynamic parameters of the phase transitions, particularly the value of free energy changed (ΔF), which is very difficult to obtain directly from the experiment. To estimate the ΔF value, enthalpy (ΔH) and entropy (ΔS) of transitions as usual are experimentally determined that are the constituents of free energy. We shall discuss below the experimental ways of estimating the values of these major thermodynamic parameters.

2. Main body

2.1. Theory

Along with genetic information realization in vivo (replication, transcription, translation), the molecule of DNA is being subjected to different conformational transitions. Moreover, there are no conformational transitions in "pure" molecule: it is always surrounded and interacts with huge number of various low-molecular compounds, which in turn, interacting with DNA, can stabilize or destabilize different conformational states of polymer molecule. To judge if this or other ligands stabilize or not different conformations of DNA, DNA conformational transition in the complex under any external factor inducing this transition should be studied (temperature, pH, chemical effect, etc.) and compared with the pure molecule transition.

Nowadays, it may be strictly established that these transitions (B-coil, A-coil, B-A, B-Z, Z-A, etc.) carry a cooperative character. The transition cooperativity is a direct consequence of the fact that the transition occurs in quasi-one-dimensional aperiodic crystal: in this case, the real phase transition is excluded.

Analysis of numerous experimental data, as well as some general representations about helix-coil transition, condition the possibility to formulate DNA main model, which is applied for theoretical observation of its melting. The model is sufficiently simple – DNA is one dimensional system that forms pairs of bases and each of them may be only in two states: helical and coil-like. Lengthening of the helical region per pair is accompanied by free energy value change ΔF. The value of ΔF determines the constant of this process:

$$\sigma = \frac{[\sigma_{i+1}]}{[\sigma_i]} = \exp(\Delta F/RT) \tag{1}$$

where R is gas constant, T is temperature, and σ_I and σ_{i+1} are concentrations of molecules containing helical regions from i and i + 1 pairs of bases, respectively. In the transition point T_0 σ =1, consequently, ΔF turns to zero. In the vicinity of this point, ΔF linearly depends on the temperature:

$$\Delta F = \Delta H + T\Delta S \tag{2}$$

where ΔH and ΔS are changes of enthalpy and entropy, respectively.

Formation of new melted region in helical part is connected to appearing of additional boundaries between helical and melted regions and requires additional changes of free energy.

Value of ΔF determines the cooperativity of the system and

$$\sigma = \exp(-F_0/2RT) \tag{3}$$

is called a cooperativity factor. If $F_0 = 0$, the cooperativity is absent. When $F_0 \to \infty$, the system is exposed to phase transition. At $0 < F_0 < \infty$, the transition carries a cooperative character and the higher is F_0, the more favorable are long helical and melted regions and correspondingly the melting interval decreases.

Observed model, known in statistical physics as Ising model, physically corresponds to a case of single-stranded homopolymer. Let us observe this model applying the method of more probable distribution [6].

It is known that equilibrium values of physical magnitudes are corresponded to their most probable values at the given energy of the system. They can be found from the condition of "nonequilibrium" free-energy minimum:

$$F = E - T\ln W \tag{4}$$

where W is the number of states corresponding to the given energy of E.

Linear homopolymer consisting of N rings is observed. Each of these rings may be in one of these two states: melted – coil-like and helical. Macroscopic state of such system at the certain T temperature is given by three parameters: N_2 is number of helical rings (in the second state), N_1 is the number of rings in coil-like state (1), and n is the number of regions consisting of rings 1 or 2. It is clear that $N_1 + N_2 = N$; moreover, the case of infinite homopolymer is observed $N \to \infty$. If F_1 and F_2 are free energies of rings being in melted and helical states, respectively, $F_0/2$ is the free energy of boundary between helical and coil-like rings, the whole energy of the system is:

$$F = F_1N_1 + F_2N_2 + F_0n \tag{5}$$

Number of microstates corresponding to given values of N_1, N_2, and n will be equal to

$$W = W_1 - W_2 \tag{6}$$

where W_2 and W_1 are numbers of modes by which helical and coil-like (melted) rings at the given values of N_1, N_2, and n may be distributed:

$$W_1 = \frac{(N_1 - 1)!}{(n-1)!(N_1 - n)!} \tag{7}$$

$$W_2 = \frac{(N_2 - 1)!}{(n-1)!(N_2 - n)!} \tag{8}$$

In the observed case in Eqs. (7) and (8), the unit can be neglected (N→∞). In this case,

$$W(N_1, N_2, n) = \frac{N_1! N_2!}{n!(N_1 - n)! n! (N_2 - n)!} \tag{9}$$

Replacing (5) and (9) in (4) and applying Stirling's formula, we will obtain

$$\begin{aligned} F = F_1 N_1 + F_2 N_2 + F_0 n - T[N_1 \ln N_1 - (N_1 - n) \ln (N_1 - n) \\ + N_2 \ln N_2 - (N_2 - n) \ln (N_2 - n) - 2n \ln n \end{aligned}] \tag{10}$$

Equilibrium values of N_1, N_2, and n are determined from conditions

$$\left|\frac{\partial F}{\partial n}\right|_{N_1 N_2} = 0 \tag{11}$$

and

$$\left|\frac{\partial F}{\partial N_1}\right|_{n} = 0 \tag{12}$$

If to mark $\xi = \exp(-F_\sigma/RT)$ and $\sigma = \exp(\Delta F/RT)$, where $\Delta F = F_1 - F_2$ is a free energy change at helix-coil transition, from Eqs. (11) and (12), we will obtain

$$\frac{1}{\xi} = \left(\frac{N_1}{n} - 1\right)\left(\frac{N_2}{n} - 1\right) \tag{13}$$

$$\sigma = \frac{1 - \frac{n}{N_2}}{1 - \frac{n}{N_1}} \tag{14}$$

at the condition of total ring number constancy ($N_1 + N_2 = N$):

The obtained equations have dependences of N_1, N_2, and n on σ. Jointly solving Eqs. (13) and (14), the equation of ring part being in helical state $\theta = N_2/N_1$ is

$$\frac{1 - 2\theta}{\sqrt{(1-\theta)\theta}} = \frac{1}{\sqrt{\xi}} \cdot \frac{1 - \sigma}{\sqrt{\sigma}} \tag{15}$$

The Eq. (15) describes the helix-coil transition curve.

From definition of the transition interval width, we will obtain:

$$\Delta T = 4\sqrt{\xi}\frac{T_0^2}{\Delta H} \tag{16}$$

where ΔH is enthalpy and T_0 is the transition temperature.

T_0 is determined from the condition that in transition point, the free energy change is equal to zero

$$\Delta F = 0 \tag{17}$$

From the Eq. (2), we will obtain

$$T_0 = \frac{\Delta H}{\Delta S} \tag{18}$$

where ΔS is the difference of entropy in melted and helical states.

It should be mentioned that in the case of $F_0 = 0$, i.e., at the absence of interaction between rings (ξ=1), the formula (16) transmits to Boltzmann's distribution. This case responds to cooperativity absence. At boundary energy increasing (decreasing of ξ) the system "becomes" cooperative; the melting interval decreases Eq. (16). In the threshold case when $\xi \to 0$, the system is entirely cooperative, but the transition is sharp: $\Delta T \to 0$.

One of the fundamental predictions is that in the transition interval, polynucleotide chain is divided into alternate helical and coil-like regions, the length of which depends on the value of ξ. The average length of the helical region is equal to

$$\nu_2 = \frac{N_2}{n} = \frac{1}{\sqrt{\xi}} \cdot \sqrt{\frac{\theta}{1-\theta}} \tag{19}$$

In the transition point, $\theta = 1/2$ and the average length of helical (and coil-like) region is equal to:

$$\nu_0 = \frac{1}{\sqrt{\xi}} \tag{20}$$

One of the first attempts to estimate the cooperativity factor value was presented in [7] by comparison of experimentally obtained value of ξ for homopolymer to the theory. It was shown that the value is in interval 10^{-4}–10^{-5}. For heteropolymer, the estimation is less precise since the melting interval width dependence on ξ in this case is logarithmic [6]. Uncertainty in values of ΔT depending on the cooperativity factor in the cases of different models shows that it is necessary to calculate and compare to experiment such characteristics of the helix-coil transition, which do not depend on ξ in wide change interval of this parameter.

Such invariant values are changes of melting temperature and melting interval width invoked by DNA binding to low-molecular compounds (ligands) [6, 8–11]. From the point of view of the effect on DNA double-helix stability, ligands that are able to form complexes with polymers may be divided into stabilizers and destabilizers. Comparison of the melting curves of

"pure" and ligands bound to >DNA can give information about the character of ligand binding to DNA: if the complex melting temperature (T_m) is higher than T_0 for pure DNA, stabilization occurs, and if T_m decreases, then, destabilization occurs. Independently on the chosen model, molecules, possessing high affinity to double-helical polynucleotide, will stabilize the native structure and molecules, well binding to coil-like DNA — destabilize polymer double helix. What concerns to the melting interval, in both cases it increases as compared to that of pure polymer.

One of the predictions of the theory is that the melting interval width dependence on ligand concentration should have bell-like shape. It is explained by the fact that at small concentrations of ligands, ΔT of complexes increases due to the redistribution of ligands between helical and coil-like regions, which takes place during denaturation process with ligand concentration enhancement in accordance to their affinity to those regions. This redistribution results in additional stabilization of remained helical (or formed denatured) regions, and the melting process is extended. Due to confinement of number of the binding sites on DNA, the further increasing of concentration of ligands leads to difficulties of redistribution process and the melting interval width again decreases. In the boundary case when all binding sites are occupied by ligands, the melting interval width increment tends to zero. In the observed case, it is assumed that each pair of bases in polymer may be a binding site for ligand [12].

It is followed from the above-mentioned case that maximum of bell-like curve of the melting interval width increment dependence on ligand concentration corresponds to concentration of the ligand on DNA equal to half of the binding sites. The treated theory was compared with the experiment of complex melting, where as a ligand acridine dyes and actinomycin [13], native (destabilizer) and denatured (stabilizer), RNAase, heavy metal ions were used.

The effect of ligands on the helix-coil transition in polynucleotide in the case of random number of the binding sites has been studied. The chosen model in [14] is the following. We will assume that in solution, there are polymer molecules with fixed values of N_1 (number of rings in coil-like state) and N_2 (number of helical regions), the total number of rings N remains constant:

$$N_1 + N_2 = N \tag{21}$$

Let add ligands into solution with polymer that can bind both with coil-like and with native regions of DNA and can be in solution in nonbound state as well. If K_2 and K_1 are numbers of ligands bound to helical and coil-like regions, respectively, and K_0 is the number of nonbound ligands, it is obvious that total number of ligands K per molecule satisfies the condition:

$$K_1 + K_2 + K_0 = K \tag{22}$$

Let us mark the number of pairs of bases per binding site for denatured and native parts of the molecules as r_1 and r_2, respectively. In this case, the number of binding sites for the respective regions will be equal to N_1/r_1 and N_2/r_2. Taking this fact into consideration for nonequilibrium free energy, we will have:

$$F = F_1N_1 + F_2N_2 + F_0n + \psi_1K_1 + \psi_2K_2 + \psi_0K_0 - TS_0 + \ln W_1\left(\frac{N_1}{r_1}, K_1\right) + \ln W_2\left(\frac{N_2}{r_2}, K_2\right) + \ln W_0(N_0, K_0) \quad (23)$$

where Ψ_1 and Ψ_2 are free energies of ligand bond with coil-like and helical parts of polymer, Ψ_0 is the free energy, N_0 is the number of binding sites in solution for free, nonbound ligand to polymer, $S_0(N_1, N_2, n)$ is the entropic member bound to pure polynucleotide, W(N, K) function is determined by:

$$W(N, K) = \frac{(N-1)!}{(K-1)!(N-K)!} \quad (24)$$

Taking into account the Eq. (24) and neglecting the unit (when N→∞ case is observed) for additional entropic member in (23) responsible for redistributing entropy of ligands, we will obtain:

$$S_{add.} = \frac{\frac{N_1}{r_1}!\frac{N_2}{r_2}!N_0!}{K_1!\left(\frac{N_1}{r_1} - K_1\right)!\left(\frac{N_2}{r_2} - K_2\right)!K_2!(N_0 - K_0)!K_0!} \quad (25)$$

It is obvious that the equation obtained from the condition $(\partial G/\partial n) = 0$ remains as it was in the absence of ligand. It means that the average length of helical region $\nu_2 = N_2/n$ at given denaturation degree does not change when the ligand is added. In its turn, it means that ligand does not change the boundary energy. On the other hand, the equation obtained from $\partial G/\partial N_1 = 0$ condition does not change:

$$\frac{1 - \frac{n}{N_2}}{1 - \frac{n}{N_1}} = \sigma\frac{(1 - c_1r_1)^{1/r_1}}{(1 - c_2r_2)^{1/r_2}} \quad (26)$$

where $c_1 = K_1/N_1$, $c_2 = K_2/N_2$ are concentrations of ligands for denatured and coil-like parts of polymer, respectively.

The developed theory gives dependencies of the experimentally observed transition parameters (the melting interval width ΔT and melting temperature T_m) on the binding parameters of a ligand with DNA (the binding constant K and the binding site r_q) and the concentration of ligands [15].

$$\delta\frac{1}{T_m} = \frac{1}{\Delta H}\ln\left[\frac{\prod_{j=l+1}^{m}\left(x_0 + p_j\right)^{1/r_j}}{\prod_{i=1}^{l}\left(x_0 + p_i\right)^{1/r_i}}x_0^{\left[\sum_{i=1}^{l}\frac{1}{r_i} - \sum_{j=l+1}^{m}\frac{1}{r_j}\right]}\right] \quad (27)$$

$$\delta\frac{\Delta T}{T_m^2} = \frac{1}{x_0\Delta H}\left[\sum_{j=l+1}^{m}\frac{p_j}{r_j\left(x_0 + p_j\right)} - \sum_{i=1}^{l}\frac{p_i}{r_i\left(x_0 + p_i\right)}\right]\frac{\partial x}{\partial\theta}|\theta = 1/2 \quad (28)$$

where

$$\delta\frac{1}{T_m}=\frac{1}{T_m}-\frac{1}{T_0}\quad \delta\frac{\Delta T}{T_m^2}=\frac{\Delta T}{T_m^2}-\frac{\Delta_0 T}{T_0^2} \tag{29}$$

where T_0 and $\Delta_0 T$ are the melting temperature and melting interval width for DNA in the absence of the ligand, T_m and ΔT are the same parameters for DNA-ligand complexes; ΔH is the enthalpy of the transition; $p_q = K_q/K_1$, where K_1 is the binding constant for the first type (arbitrary chosen) of interaction of the ligand with one of the DNA forms; K_q is the binding constant for the q-th binding type (q = 2,…,m), which is expressed by the following equation:

$$K_q=\frac{c_q\cdot r_q}{c_0\left(1-c_q\cdot r_q\right)},\ (q=1,\ldots,m) \tag{30}$$

$c_i=\frac{k_i}{N_1}\ (i=1,\ldots,1), c_j=\frac{k_j}{N_2}\ (j=l+1,\ldots,m)$ are the concentrations of the ligand bound to the corresponding forms of DNA and $c_0 = k_0/N_0 < < 1$ is the concentration of unbound ligand, where x_0 is the equation solution at q = 0.5 ($q = N_f/N$ *(f = 1, 2)* is the fraction of either forms of the polynucleotides (B, Z, A, coil, etc.) within the melting interval).

$$(1-\theta)\sum_{i=1}^{l}\frac{p_i}{r_i\left(x+p_i\right)}+\theta\sum_{j=l+1}^{m}\frac{p_j}{r_j\left(x+p_j\right)}=c \tag{31}$$

c = 2D/P, where D is the total concentration of ligand in solution and P is that of bases of DNA.

2.2. Experiment

DNA is a one-dimensional aperiodic crystal [1]. Therefore, as it was mentioned above, the true phase transition in such molecules could not occur. The two phases formed during the transition will tend to be mixed as continuously decreasing parts of the system. Such conversion is known as cooperative phase transition, two thermodynamic parameters of which are characterized by temperature of transition T_0 and width of transition ΔT, on the contrary of real phase transition, which is realized at fixed temperature.

2.2.1. Helix-coil transition

All nucleotides in the native state of DNA are in helix form, which has much lower free energy, i.e., high stability, than any other states that DNA assumes to be at room temperature and other ordinary physiological conditions. In the nonbound state, the nucleotide chain to which the nucleotide base pains are attached has freedom of motion. The bound or nonbound states may be classified in terms of "helix" and "coil" states, respectively, and the transition from one phase to another is called helix-coil transition or melting.

Unfolding of the double helix of DNA is produced as an effect of temperature (T), pH, ionic strength (μ), and denaturants [16, 17]. The process is accompanied by the transition of the bound state of bp to nonbound state, which propagates from more stable to less stable groups.

It has been found experimentally that the transition of DNA occurs in a very sharp manner (the transition is highly co-operative), which is characterized by two physical parameters: the melting temperature, T_0 and the width of transition, ΔT. The sharpness of the transition depends on the value of junction free energy, F_j. The true phase transition (transition of crystal structures) occurs only at the case of $F_j \rightarrow \infty$ (the junction energy is infinitely large). These parameters change for complexes of DNA with "low-weight" compounds (ligands). Integration of the structural, kinetic, and thermodynamic data of ligand-nucleic acids interaction is necessary to clearly understand the mechanisms of ligand-nucleic acid complex formation. Such investigations are much important to characterize the binding mode, sequence specificity, and understanding in detail designing new generation of drugs affecting the gene expression. Structural data obtained by X-ray crystallography and NMR for many drug-nucleic-acid complexes were successfully used for estimating ligands that attempt to correlate structure with binding affinity. It was established that upon binding, the ligands interact with substrate as a rigid compound, which is advantageous for revealing thermodynamic contribution from structural data [18]. Data of the structures of ligand-DNA complexes obtained by X-ray crystallography and NMR methods showed the more possible way to much ligand shape with the receptors of substrates and represent only one aspect of the complex formation. That is, the binding site will be occupied by ligand complemented it in terms of shape, charge, and other binding components [19], neglecting the energetic characteristics of binding process. So, the structural data alone cannot define the driving forces for binding and predicting the binding affinities. To understand the molecular mechanism and energetics of ligand-nucleic acid interaction, knowledge of thermodynamic parameters provide data elucidating the driving forces of complex formation process [20]. A complete thermodynamic profile for a system of interest requires determination of the free energy, enthalpy, and entropy.

The free energy ΔG is the key thermodynamics parameter, dictating the direction of biomolecular equilibria. If its sign is negative, the binding reaction or conformational transition will proceed spontaneously to an extent governed by the magnitude of ΔG. If its sign is positive, the magnitude of ΔG specifies the energy needed to drive the reaction to form product. The free energy is a balance between enthalpy and entropy. The enthalpy change reflects the amount of heat energy required for achievement a particular state, and the entropy measures how easily that energy might be distributed among various molecular energy levels. For binding reactions, negative enthalpy values are common (but not omnipresent), reflecting a tendency for the system to fall to lower energy levels by bond formation. Positive entropy values are common for binding reactions, reflecting a natural tendency for disruption of order. All binding reactions must overcome inescapable entropic penalties resulting from the loss of rotational and translational degrees of freedom.

The binding enthalpy (ΔH) can be detected using isothermal titration calorimetric (ITC) or differential scanning calorimetric (DSC) methods [18–21]. The methods have several advantages for measuring binding energetic parameters at the same time having distinct difficulties, the dominant of which is high concentration of nucleic acids that require large quantities of expensive products, and besides, the possible aggregation makes very difficult to explain the experimental results [21–23]. DSC and ITC are laborious and time-consuming methods that often relegate calorimetric ones to be used as a secondary screening method. To overcome these limitations, several attempts have been made to improve the throughput of calorimetric

and thermodynamic measurements. Mentioned difficulties for detecting the thermodynamic parameters of ligand-nucleic acid interaction may be overcome by applying methods, which are experimentally easy to perform, where very low concentrations of nucleic acids are used, which exclude the very unwanted process of aggregation [24].

The quantitative analyses of the effect of different substances (ligands) such as ions, antibiotics, dyes, proteins, etc. made it possible to suggest a simple method named "tie calorimetry" to estimate ΔH of conformational transitions [25–28]. It has been shown that the enthalpy of helix-coil transition or melting (per base pair) could be determined from the experiments on DNA melting with ligands by the following general formula (32) (This formula is valid for all known types of conformational transition in one-dimensional crystals and for all types of ligands):

$$\Delta H = R \cdot \lim_{c \to 0} \left\{ (\delta \Delta T / \delta T_m)^2 T_0^2 \right\} \cdot c, \tag{32}$$

where $\delta T_m = T_m - T_0$ and $\delta \Delta T = \Delta T - \Delta_0 T$, T_m and ΔT are the melting temperature and width of transition for DNA when the ligand is added to the solution, T_0 and $\Delta_0 T$ are the same quantities for DNA without ligand, c = 2D/P is the total number of ligand molecules in solution (D) divided by the total number of DNA base pairs (2P), and R is the gas constant. Eq. (32) is absolutely general, and its validity does not depend on the values of the thermodynamics parameters of complexes such as binding constants of ligand with DNA, the number of binding sites on the biopolymer, etc. This was covered comprehensively in [25–28]. On the other hand, obtained data showed that if the ligand complexes preferably bind with one of the conformations of DNA, the calculations become very simple [21–23], and for calculations, it is enough to compare the theoretical formula with the experiment either for δT_m or $\delta \Delta T$ [29]. Ethidium bromide, a very well-known ligand, binds preferably with the helix DNA [26, 27]. This enabled us at very low ligand concentration (c→0) with the combination of the area method [28, 29] to estimate ΔH for DNAs of two different GC contents at different Na^+ concentrations with very high accuracy.

It was shown that at very small concentration of the ligand, the shift of the melting temperature (δT_m) and widening of the melting curve ($\delta \Delta T$) are represented by the following equations:

$$\delta T_m = \Lambda \frac{R T_0^2 c}{\Delta H} \tag{33}$$

$$\delta \Delta T = \Lambda^2 \frac{R T_0^2 c}{\Delta H} \tag{34}$$

For the coefficient A, the following formula is obtained:

$$\Lambda = 2 \frac{(r_1/r_2)p - 1}{(r_1/r_2)p + 1} \cdot \frac{(K_1/r_1)P + (K_2/r_2)P}{4 + (K_1/r_1)P + (K_2/r_2)P} \tag{35}$$

where r_2 and r_1, are the number of binding sites on the duplex and single-stranded DNA, respectively, K_2 and K_1 are the binding constants of ligand with helix and coil states of DNA, respectively, and P is the concentration of phosphate groups of DNA: $p = K_2/K_1$.

The only condition for validity of Eqs. (33) and (34) is c→0.

From Eq. (35), it follows that if

$$(K_1/r_1)P << 4 \quad (K_2/r_2)P >> 4 \tag{36}$$

$$\delta T_m = 2\frac{RT_0^2 c}{\Delta H} \tag{37}$$

$$\delta \Delta T = 4\frac{RT_0^2 c}{\Delta H}. \tag{38}$$

These formulas show that if $\delta \Delta T$ is twice greater than δT_m, the binding constant of ligand with one of the conformation of DNA is much greater than that of the other conformation. In this case, ΔH may be estimated on by Eqs. (34) or (35). The accuracy of ΔH value depends on the accuracy of experimental estimations of the $\delta \Delta T$ and δT_m values at different concentrations of ligand (different c). Therefore, the error is large (1.5–2 kcal/mol) when ΔH is calculated by Eq. (32) [28].

The accuracy of ΔH estimation is much higher if the "area" method is used for obtaining δT_m. The method may be explained as following. The DNA melting temperature T_0 may be defined as the first moment of the differential melting curve ($-d\vartheta/dT$):

$$T_0 = \int_{T_{AT}}^{T_{GC}} \left(-\frac{d\vartheta}{dT}\right) T dT \tag{39}$$

After integration, we have the following expression:

$$T_0 = T_{GC} - \int_{T_{AT}}^{T_{GC}} (1-\vartheta) dT \tag{40}$$

Here,

$$s = \int_{T_{AT}}^{T_{GC}} (1-\vartheta) dT \tag{41}$$

is numerically equal to the square limited by the melting curve $(1\text{-}\vartheta)$, the temperature axis, and the $T = T_{GC}$ vertical line. It follows from Eq. (39) that T_0 varies if the shape and place of melting curve change. Both the shape and the place of the melting curve change if ligand is added to the DNA solution. In this case, melting temperature of the complex T_m is found as:

$$T_m = T_{GC} - \int_{T_{AT}}^{T_{GC}} (1-\vartheta^*) dT, \tag{42}$$

where T_m is the temperature and $(1\text{-}\vartheta^*)$ is the melting curve of DNA-ligand complex.

It follows from Eqs. (39) and (40) that the variation in temperature can be expressed as:

$$\delta T = \delta s = \int_{T_{AT}}^{T_{GC}} (1 - \vartheta) dT - \int_{T_{AT}}^{T_{GC}} (1 - \vartheta^*) dT, \tag{43}$$

where δs is the area limited by melting curves of DNA (left curve) and DNA-ligand complex (right curve) (**Figure 1**).

Substituting Eq. (43) to Eq. (36) for the enthalpy of helix-coil transition, one gets:

$$\Delta H = 2 \frac{RT_0^2 c}{\delta s} \tag{44}$$

It should be noted that measuring of δs should be done at very small concentrations of ligand ($c < 3 \cdot 10^{-2}$) [23], where ΔH is independent of the chosen concentrations of ligand. The dependence of ΔH (in kcal/mol) on Na^+ is shown in **Figure 2**.

The values of ΔH obtained here agree excellently with calorimetric data [30]. The ΔS value may be calculated taking into account that at the transition mid-point (T_0), the free energies of the phases (for example, helix and coil) are equal to each other. Therefore,

$$\Delta G = \Delta H - T_0 \Delta S = 0. \tag{45}$$

Knowing the value of transition point T_0, one can calculate the value of ΔS by equation

$$\Delta S = \frac{\Delta H}{T_0}. \tag{46}$$

The averaged values of ΔH, T_0, ΔS at different concentrations of Na^+ are presented in **Table 1**.

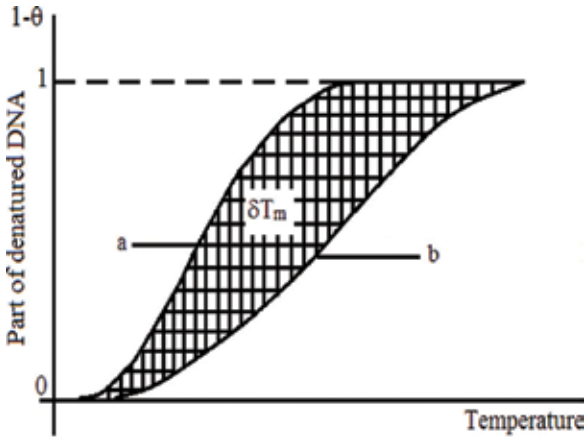

Figure 1. The area limited by melting curves (δs) of DNA (left curve) and DNA-ligand complex (right curve) is numerically equal to the shift of the melting temperature (δT_m).

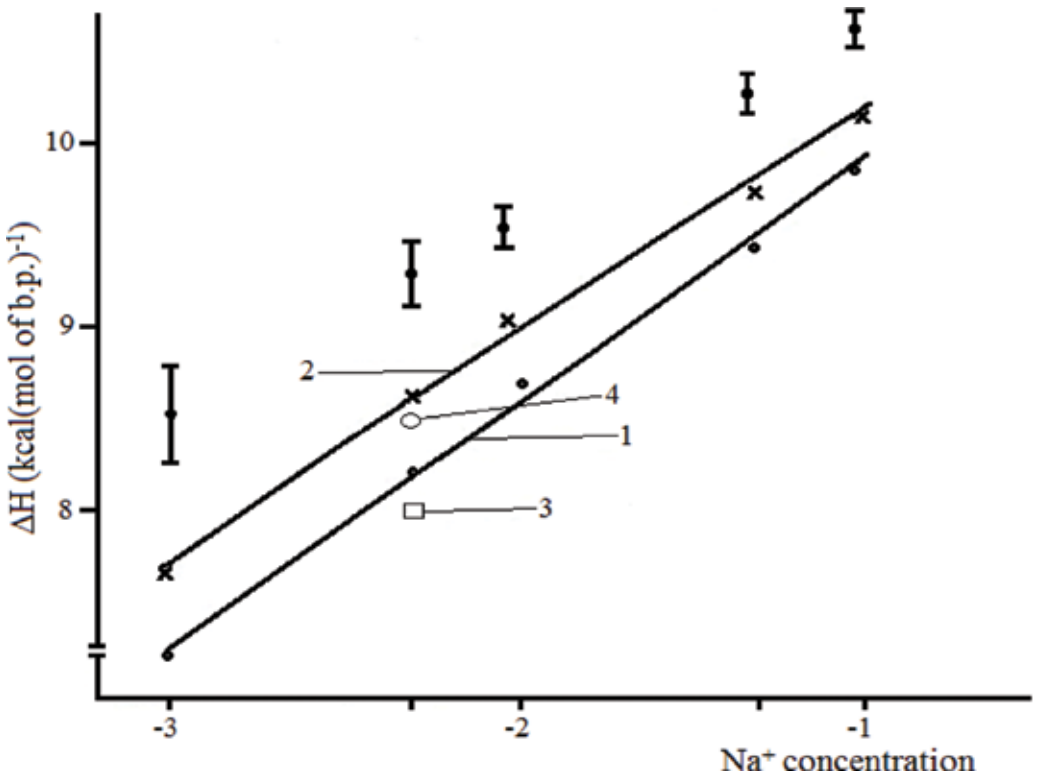

Figure 2. Dependence of ΔH on concentration of Na^+. 1,3 Cl.Perfringens DNA; 2,4 M. lysodeikticus DNA. 1 and 2 are our data. 3 and 4 data are of Klump and Ackermann [30]. Error bars are shown separately above the experimental points.

	Na^+ M	$-lgNa^+$	T_0 °C	Cl.perfr. ΔH kcal/mol	ΔS ent. unit	T_0 °C	M. Lysod. ΔH kcal/mol	ΔS ent. unit
1	10^{-3}	3.0	45.1	7.2 ± 0.5	22.6	68.4	7.7 ± 0.4	22.5
5	10^{-3}	2.3	56.3	8.2 ± 0.3	24.9	77.6	8.6 ± 0.3	24.5
1	10^{-2}	2.0	61.0	8.7 ± 0.2	26.0	81.8	9.0 ± 0.2	25.4
5	10^{-1}	1.0	77.3	9.8 ± 0.2	28.0	94.9	10.1 ± 0.2	27.4

Table 1. The averaged values of ΔH, T_0, ΔS at different concentrations of Na^+.

2.2.2. B-A transition

Investigations show that B-A conformational transition is cooperative, and it is realized in big amount of nucleotides conversion from B-form to A-form. Since the transition is independent of temperature and GC content of biopolymer, the Ising model has been employed for theoretical description of the process. The B-A transition initiated by any external factor a is represented by:

$$\frac{1-2\vartheta}{\sqrt{(1-\vartheta)\vartheta}} = \frac{1-s}{\sqrt{s}\sqrt{\sigma_{AB}}} \tag{47}$$

where $\vartheta=f(a)$ is the dependence of part of A-form on –a factor, s-form is the equilibrium constant of transition, σ = (exp $-$ $\varepsilon_0 T$), ε_0 is the energy of junction, and T is the absolute temperature. Eq. (47) gives

$$\Delta a = \left|\frac{\partial \vartheta}{\partial a}\right|_{a=a_0}^{-1} = \frac{4Q}{\nu_0} \tag{48}$$

where $\nu_0 = \left(\sqrt{\sigma_{AB}}\right)^{-1}$ is the length of cooperativity and Q is a constant showing the steepness of free energy ΔG of A- and B-forms at the transition region. Knowing Q and Δa, the ΔG of A-B transition can be determined. It was shown that for pure water (100%) environment, ΔG_{AB} = 1 *kcal/mol* [31, 32]. The obtained data coincide with the experimental results of [33], where the junctions of A- and B-forms are considered as a tie, which stabilizes the duplex.

2.2.3. B-Z transition

Poly[d(G-C)] in a 55% ethanol solution exhibits the B-Z transition when the temperature increased [15, 33]. A polyamine, AEPDA, stabilizes Z-form and binds to it much stronger than to the B-form (**Figure 3**). Results show the temperature effect on the B-Z equilibrium without the polyamine (**Figure 3a**) and in its presence at a concentration of one molecule per 50 base pairs (**Figure 3b**). Obviously, the B-form of the polymer is stabilized by the rise of temperature in both cases. The pattern of CD spectra and the presence of a distinct isodichroic point at 301 nm show that only B- and Z-forms are involved in the equilibrium.

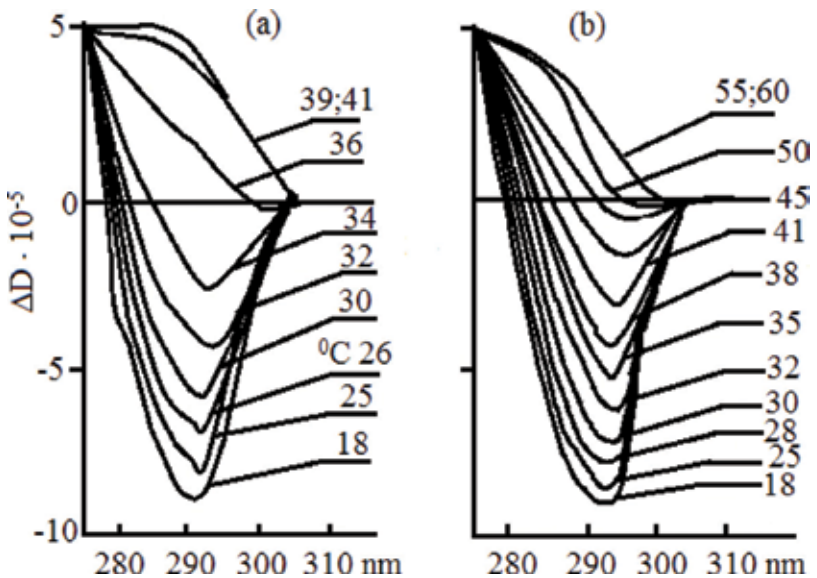

Figure 3. A family of equilibrium circular dichroism (CD) spectra of poly[d(G-C)] at different temperatures in the absence (a) and presence (b) of polyamine (1 molecule per 50 base pairs). Conditions: ethanol: 55% v/v, NaCl: 5–10^{-4} M, and EDTA: 5·10^{-5}M.

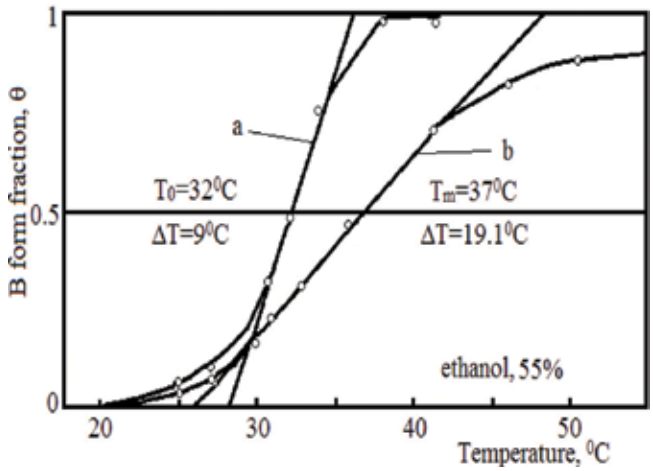

Figure 4. Profiles of the Z-B transition of free poly[d(G-C)] and its complex with polyamine (1 molecule per 50 base pairs). θ is for the B-form fraction from the CD data of **Figure 3**.

The transition profiles (**Figure 4**) show that, when the polyamine is added to the Z-form of poly[d(G-C)], the Z-form is stabilized and also the transition interval ΔT significantly widens. So, the polyamine is a "tie" for the Z-form. In this case, the transition enthalpy can be calculated by measuring the shift of the transition point (δT_0) and the widening of the transition curve $\delta\Delta T$ (see the Eqs. (36)–(38)).

Experiments showed that the ratio $\delta\Delta T/\delta T = 2$, which is independent on ionic strength [15, 34–36]. Thus, the ΔH value for the poly[d(G-C)] in 55% ethanol, ΔH_{BZ} = −1.4 kcal/mol, is independent on the ionic strength.

Eqs. (37) and (38) are restricted to the only condition of c→0. $K_Z >> 1$, $K_B >> 1$, and at this case, we obtain Eqs. (6) and (7), which show that if the widening of the transition curve is twice as great as the shift of the transition point, ΔH_{BZ} can be determined independently by each equation.

Figure 5 shows that for the polyamine, the ratio $\delta\Delta T/\delta T_0 = 2$; therefore, this ligand is perfect for thermodynamic investigations of a B-Z transition. **Table 2** presents the data on the polyamine action calculated within the range of ionic strength form of 0.5–2 mM NaCl. These data show that δT_0 and $\delta\Delta T$ values do not depend on NaCl concentration. Consequently, ΔH_{BZ} is independent of ionic strength under these conditions. **Figure 5** shows the $\delta\Delta T$ and δT_0 of a B-Z transition plotted as a function of c = 2D/P.

Since the slopes of the lines are related as 2:1, the enthalpy of the transition may be obtained using Eqs. (37) or (38):

$$\Delta H_{BZ} = -2\frac{RT_0^2}{\delta T_0}\cdot c = -(1.4 \pm 0.2)\,kcal/mol$$
$$\Delta H_{BZ} = -4\frac{RT_0^2}{\delta \Delta H}\cdot c = -(1.4 \pm 0.2)kcal/mol \quad (49)$$

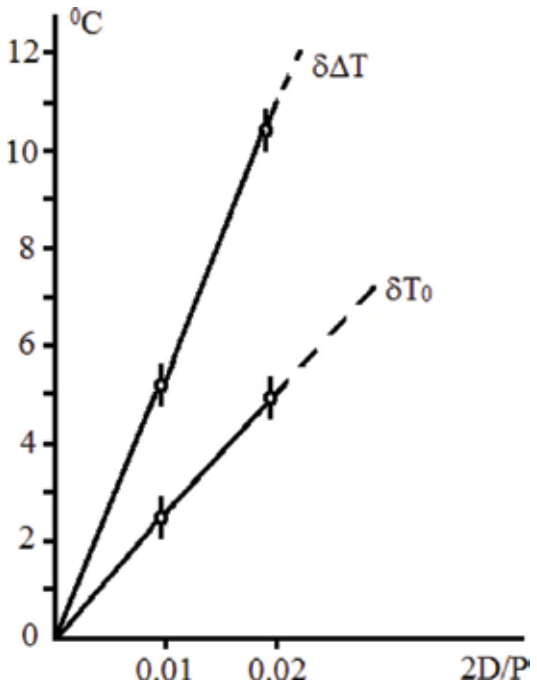

Figure 5. Dependents of widening $\delta\Delta T$ and shift δT_0 of the B-Z transition on "tie" centration.

c = 2D/P	**c = 0.01**		**c = 0.02**	
NaCl, M	δT_0	$\delta\Delta T$	δT_0	$\delta\Delta T$
5×10^{-4}	3.0	4.6	5.6	11.6
	2.7	5.2		
	2.0	4.6	5.0	10.1
	2.6	4.8	5.3	10.8
10^{-3}	2.1	5.0		
	2.6	4.4		
	2.0	6.0		
	2.2	5.1		
1.4×10^{-3}	2.7	6.6		
2×10^{-3}	3.0	5.6		
	3.0	5.0		
	3.0	5.3		

Table 2. Changes in the parameters of the Z to B transition induced by a temperature increase in the presence of the polyamine (AEPDA) at two c = 2D/P and different ionic strengths.

We consider the values of ΔH_{BZ} obtained in this work reliable, which is in good agreement with the recently obtained same value of ΔH_{BZ} using an independent method based on the polyelectrolyte theory of the B-Z transition [37].

2.2.4. Thermodynamic parameters of binding: binding constants (K and binding site size r, the number of DNA base pairs corresponding to a binding site)

A traditional method of obtaining the interaction thermodynamic parameters is the Scatchard's analysis of the ligands binding data, which consists of plotting the r/c_f value versus *r,* where *r* is the ratio of the bound ligand to DNA base pair concentration and c_f is the free ligand concentration [37]. This method has two major drawbacks. The first is the uncertainty in the c_f value [37, 38], and the second is the existence of two different models of interaction of the ligands with DNA in the case of nonlinear Scatchard plots. One model assumes the presence of more than one type of independent binding sites, and the other model suggests interaction between bound ligands [34].

Our theory suggests another method for obtaining the binding parameters of the ligands interacting with DNA [15].

The binding parameters *(K* and r) are the parameters of the theory. They can be evaluated from comparison of the theory with experiment. The shape of the curves of dependencies of the inverse melting temperature $\delta(1/T_m)$ and of the melting range width $\delta(\Delta T/T_m^2)$ on the concentration of ligands is very different and sensitive to different values of r*:* the binding site size and $p_q = K_q/K_1$, where K_1 is the binding constant for the first type (arbitrarily chosen) of interaction of the ligand with one of DNA forms, K_q is the binding constant for the q-th binding type (q = 2 …….m, m types of bending are considered). **Figure 6** shows that the effect of the value of p_q is very significant on the shape of the dependence of $\delta(\Delta T/T_m^2)$ on c**.** Therefore, the parameters may be determined, so as to provide the best fit between the theory and experiment. Major criteria for fitting are the position, the shape, and the size of maximum of the experimentally obtained $\delta(\Delta T/T_m^2)$ on ***c*** or $\delta(1/T_m)$.

We applied the conjugated gradient method for the theoretical analysis of the obtained experimental data of helix-coil transition of the complexes EtBr and AMD with DNA. The binding parameters were determined to provide the best fit between the calculated dependence of $\delta(\Delta T/T_m^2)$ on c and the observed one (**Figure 7**). The analysis of the obtained data shows that EtBr and AMD may form at least five types of complexes of which three types with helix DNA and two types with coiled DNA at 10^{-2} M Na^+ (**Table 3**). Another theoretical parameter is the ratio of the binding constants $p_q = K_j/K_t$ (q = 2,…,m). K_q values are readily calculated if one of the binding constant is known.

The calculated values of K_q for EtBr and AMD are presented in **Table 3**. The values of n and K_q obtained agree with the values determined from independent experiments [15].

Index "s" corresponds to the "strong" binding mode and "w" to the "weak" binding mode.

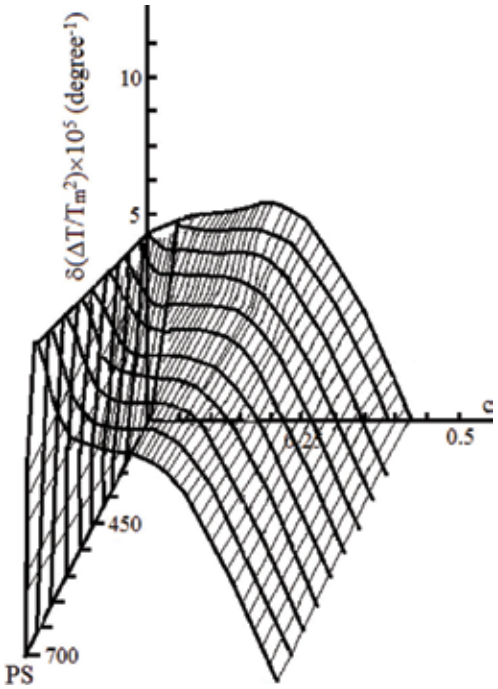

Figure 6. Dependence of $\delta(\Delta T/T_m)$ on the concentration of the ligand (c) and p_q [39]. Parameters of the theory are: m = 5; l = 3; $r_1 = 3$; $r_2 = 10$; $r_3 = 5$; $r_4 = 6.75$; $r_5 = 12$; $p_1 = l$; $p_2 = 4.2$; $p_3 = 5$; $p_4 = 5.5$; $p_5 = l5$; $p_6 = 120$.

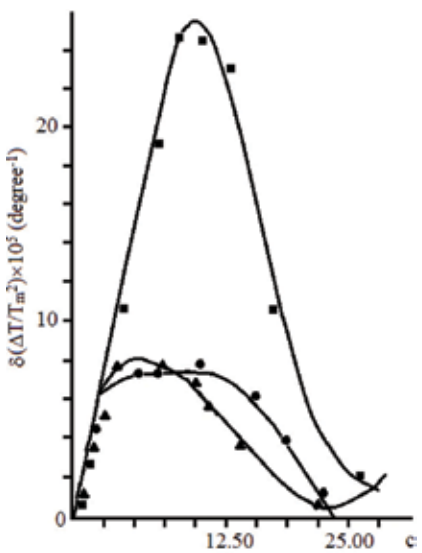

Figure 7. Dependence of $\delta(\Delta T/T_m^2)$ on c [39]. Parameters of the theory are: (■) EtBr at 2.2×10^{-3}M Na^+ m = 7; l = 4; ΔH = 7.6 kcal/mol and $r_1 = 3$; $r_2 = 10$; $r_3 = 2$; $r_4 = 6.75$; $r_5 = 12$; $p_1 = l$; $p_2 = 1.2$; $p_3 = 0.01$; $p_4 = 10$; $p_5 = 15$; $p_6 = 120$; $p_7 = 0.02$. (▲) AMD at 2.2×10^{-3}M Na^+ m = 6; l = 4; ΔH = 7.6 kcal/mol and $r_1 = 3.0$; $r_2 = 6.0$; $r_3 = 6$; $r_4 = 7$; $r_5 = 12$; $r_6 = 4$; $p_1 = l$; $p_2 = 1.5$; $p_3 = 4.2$; $p_4 = 5.5$; $p_5 = 160$; $p_6 = 0.1$. (●) EtBr at 2.2×10^{-2}M Na^+ m = 5; l = 3; ΔH = 8.5 kcal/mol and $r_1 = 3$; $r_2 = 10$; $r_3 = 5$; $r_4 = 6.75$; $r_5 = 12$; $p_1 = l$; $p_2 = 5$; $p_3 = 4.2$; $p_4 = 5.5$; $p_5 = 200$. Points stand for experimental values.

Experimental conditions	Ligand	Binding site size n					Binding constant $K_q \times 10^{-3}$				
		Helix			Coil		Helix			Coil	
		n_s	n_{w1}	n_{w2}	n_s	n_{w1}	K_s	K_{w1}	K_{w2}	K_s	K_{w1}
10^{-2} M Na^+	EtBr and AMD	6	3.3	2.5	5	1.5	2.7	0.07	0.06	0.07	0.013
2.2×10^{-3} M Na^+	EtBr	6	3.3	2.5	5	1.5	5.0	0.6	0.4	0.05	0.04

Table 3. Binding parameters of EtBr and AMD with helix and coil DNA as estimated by the theory-experiment comparison by conjugated gradient method.

3. Conclusion

In this work, it has been shown that "tie calorimetry" possesses a number of advantages. The measurements can be carried out in such concentrations that the intermolecular interactions and denaturation effect on medium pH are neglected. From the above mentioned, it is concluded that the helix-coil transition enthalpy can be calculated by the "tie calorimetry" according to the formula (32) and the only condition is that c << 1. On the other hand, determining the value of ΔH, the respective value of ΔS may be calculated by the formula (18). Calorimetry is a direct technique especially suitable when ΔH_{BZ} is high. By contrast, the "tie" calorimetry is most suitable at low ΔH_{BZ} values. It follows from Eqs. (33), (34) or (36), (37) that the low ΔH_{BZ} value results in a great change in the position of the transition point or in the transition width. Therefore, these methods are complementary.

Besides, it may be said that the "tie" calorimetric method is simple and very easy to be performed. It is absolute and no graduation is required for it. The method is based on the measuring of differential experimental values, which excluded systematic errors. Therefore, combination of both "area" and "tie" calorimetric methods makes it possible to establish the energetic parameters of phase transitions with very high accuracy.

Author details

Armen T. Karapetyan[1] and Poghos O. Vardevanyan[2]*

*Address all correspondence to: p.vardevanyan@ysu.am

1 Chair of Physics and Electrical Engineering, National University of Architecture and Construction of Armenia, Yerevan, Armenia

2 Department of Biophysics, Faculty of Biology, Yerevan State University, Yerevan, Armenia

References

[1] Schrodinger E. What Is Life? The Physical Aspect of the Living Cell. Dublin: Cambridge University Press; 1944. 194 p

[2] Landau LD, Lifshits EM. Statistic Physics. Moscow: Nauka; 1964

[3] Vedenov AM, Dichne AM, Frank-Kameneteskii MD. Helix-Coli transition of DNA. Uspechi physicheskich nauk (In Russian). 1971;**105**:479-519

[4] Saenger W. Principles of Nucleic Acids Structure. New York, Berlin, Heidelberg, Tokyo: Springer-Verlag; 1984. 515 p

[5] Dickerson RE. DNA structure from A to Z. Methods in Enzymology. 1992;**211**:67-111

[6] Vardevanyan PO. Structural Transitions in DNA and DNA-Protein Complexes at Different Functional States of Genome [Thesis]. Yerevan: Yerevan State University; 1990

[7] Crothers DM, Zimm BH. Theory of the melting transition of synthetic polynucleotides: Evaluation of the stacking free energy. Journal of Molecular Biology. 1964;**9**:1-9

[8] Vardevanyan PO, Antonyan AP, Parsadanyan MA, Davtyan HG, Karapetyan AT. The binding of ethidium bromide with DNA: Interaction with single- and double-stranded structures. Experimental and Molecular Medicine. 2003;**35**:527-533

[9] Vardevanyan PO, Antonyan AP, Hambardzumyan LA, Shahinyan MA, Karapetian AT. Thermodynamic analysis of DNA complexes with methylene blue, ethidium bromide and Hoechst 33258. Biopolymers and Cell. 2013;**29**:515-520

[10] Vardevanyan P, Antonyan A, Parsadanyan M, Shahinyan M, Melqonyan G. Behavior of ethidium bromide-Hoechst 33258-DNA and ethidium bromide-methylene blue-DNA triple systems by means of UV melting. International Journal of Spectroscopy. 2015;**2015**:1-5

[11] Chaires JB. Energetics of drug–DNA interactions. Biopolymers. 1997;**44**:201-215

[12] Permogorov VI, Frank-Kamenetskii MD, Serdyukova LA, Lazurkin YS. Determination of helix-coil transition heat from the melting curves of deoxyribonucleic acids containing additional bonds between chains. Highmol. Comp. (In Russian). 1965;**7**:362-369

[13] Wadkins RM, Jovin TM. Actinomycin D and 7-aminoactinomysin D binding to sigle-stranded DNA. The Biochemist. 1991;**30**:9469-9478

[14] Frank-Kamenetskii MD, Karapetyan AT. To the theory of melting od DNA complexes with low-molecular compounds. Journal of Molecular Biology (In Russian). 1972;**6**:621-627

[15] Karapetian AT, Mehrabian NM, Terzikian GA, Vardevanian PO, Antonian AP, Borisova OF, Frank-Kamenetskii MD. Theoretical treatment of melting of complexes of DNA with ligands having several types of binding sites on helical and single-stranded DNA. Journal of Biomolecular Structure & Dynamics. 1996;**14**:275-283

[16] Vardevanyan PO, Antonyan AP, Parsadanyan MA, Shahinyan MA, Hambardzumyan LA, Torosyan MA, Karapetian AT. The influence of GC/AT composition on intercalating and semi-intercalating binding of Ethidium bromide to DNA. Journal of the Brazilian Chemical Society. 2012;**23**:2016-2020

[17] Vardevanyan PO, Antonyan AP, Parsadanyan MA, Pirumyan KV, Muradyan AM, Karapetian AT. Influence of ionic strength on Hoechst 33258 binding with DNA. Journal of Biomolecular Structure and Dynamics. 2008;**25**:641-646

[18] Chaires JB. Calorimetry and thermodynamics in drug design. Annual Review of Biophysics. 2008;**37**:138-151

[19] Chaires JB. Drug-DNA interactions. Current Opinion in Structural Biology. 1998;**8**:314-320

[20] Herry CM. Structure-based drug design. Chemical & Engineering News. 2001;**79**:69-74

[21] Suh D, Chaires JB. Criteria for the mode of binding of DNA binding agents. Bioorganic & Medicinal Chemistry. 1995;**3**:723-728

[22] Delban F, Quadrifolio F, Giancotti V, Crescenzi V. Comparative microcalorimetric dilatometric analysis of the interactions of quinacrine, chloroquine and ethidium bromide with DNA. Biopolymers. 1982;**21**:331-341

[23] Babayan Y, Manzini G, Xodo LE, Quadrifolio F. Base specificity in the interaction of ethidium and synthetic polyribonucleotides. Nucleic Acids Research. 1987;**15**:5803-5812

[24] Vardevanyan PO, Antonyan AP, Parsadanyan MA, Davtyan HG, Boyajyan ZR, Karapetyan AT. Complex-formation of ethidium bromide with poly[D(A-T)]·poly[D(A-T)]. Journal of Biomolecular Structure and Dynamics 2005;**22**:465-470

[25] Lazurkin YS, Frank-Kamenetskii MD, Trifonov EN. Melting of DNA: Its study and application as a research method. Biopolymers. 1970;**9**:1253-1306

[26] Lazurkin YS. Physical Methods of Investigation of Proteins and Nucleic Acids. (in Russian). Moscow: Nauka; 1967

[27] Karapetyan AT, Vardevanyan PO, Terzikyan GA, Frank-Kameneteskii MD. Theory of helix-coil transition on DNA-ligand complexes: The effect to two types of interaction of ligand on the parameters of transition. Journal of Biomolecular Structure and Dynamics. 1990;**8**:123-130

[28] Karapetyan AT, Permogorov BU, Frank-Kameneteskii MD. In: Andronicashvili EH, editor. Conformational Changes of Biopolymers in Solutions. Moscow: Nauka; 1973. p. 43-49

[29] Karapetyan AT, Vardevanyan PO, Frank-Kameneteskii MD. Enthalpy of helix-coil transition of DNA: Dependence on Na^+ concentration and GC-content. Journal of Biomolecular Structure and Dynamics. 1990;**8**:131-138

[30] Klump H, Ackermann T. Influence of the base composition of DNA on the transition enthalpy. Biopolymers. 1971;**10**:513-522

[31] Ivanov VI, Minchenkova LE, Minyat EE, Frank-Kamenetskii MD, Schyolkina AK. The B to A transition of DNA in solution. Journal of Molecular Biology. 1974;**87**:817-833

[32] Ivanov VI, Krylov DU, Minyat EE, Minchenkova LE. B-A transition in DNA. Journal of Biomolecular Structure & Dynamics. 1983;**1**:453-460

[33] Ivanov VI, Karapetian AT, Minyat EE. Structure and expression. In: Sarma RH, Sarma MH, editors. DAN and its Drugs Complexes. Vol. 2. Guilderland, N.Y.: Adenine Press; 1987. p. 205-216

[34] Cantor CR, Schimmel PR. Biophysical Chemistry. Part II. The Behavior of Biological Macromolecules. N.Y: W.H. Freeman and company; 1980. 365 p

[35] Nechipurenko YD. Analysis of Binding of Biologically Active Compounds to Nucleic Acids. (in Russian). Ijevsk: Moscow; 2015. 188 p

[36] Nechipurenko YD. Analysis of binding of ligands to nucleic acids. Molecular Biophysics 2014;**59**:12-36

[37] Vardevanyan PO, Antonyan AP, Manukyan GA, Karapetian AT, Shchelkina AK. Borisova OF. Molecular Biology (Russia). 2000;**34**:310-315

[38] McGhee JD, von Hippel PH. Theoretical aspects of DNA-protein interactions: Co-operative and non-cooperative binding of large ligands to a one-dimensional homogeneous lattice. Journal of Molecular Biology. 1974;**86**:469-489

[39] Karapetian AT, Mehrabian NM, Terzikian GA, Antonian AP, Vardevanian PO, Frank-Kamenetskii MD. Journal of Biomolecular Structure & Dynamics. 1998;**14**:229-265

Chapter 4

Calorimetry Characterization of Carbonaceous Materials for Energy Applications: Review

Zulamita Zapata Benabithe

Additional information is available at the end of the chapter

http://dx.doi.org/10.5772/intechopen.71310

Abstract

Carbonaceous materials are of great interest for several applications in adsorption, catalysis, gases storage, and electrochemical energy storage devices because of the ability to modify their pore texture, specific surface area, and surface chemistry. Some of the most used precursors are carbon gels, biomass, carbon nanotubes, and coal. These materials can be doped or functionalized to modify their surface. Immersion calorimetry is one of the techniques used to determine the textural and chemical characterization of solids like carbonaceous materials. Immersion calorimetry provides information about the interactions that occur between solids and different immersion liquids. The measurement of heats of immersion into liquids with different molecular sizes allows for the assessment of their pore size distribution. When polar surfaces are analyzed, both the surface accessibility of the immersion liquid and the specific interactions between the solid surface and the liquid's molecules account for the total value of the heat of immersion. Zapata-Benabithe et al., Castillejos et al., Chen et al., and Centeno et al. prepared different materials and used immersion calorimetry into benzene, toluene, and/or water to correlate the external surface area of microporous solids with energy parameters such as specific capacitance or chemical surface (oxygen content, acid groups, or basic groups). This chapter will be compiling a review of the results founded about the calorimetry characterization of carbonaceous materials for energy area applications.

Keywords: immersion calorimetry, carbonaceous materials, energy applications

1. Introduction

Nowadays, the demand for electricity worldwide is supplied mainly by conventional energy sources (oil, natural gas, and coal); however, supply from renewable energy sources such as solar, wind, and others has been growing quickly since the end of the 2000's, from 18% (2000)

to 26% (2016) [1]. Although the consumption of these renewable energies has increased during the last decade, one of the main drawbacks with this type of energy is the reliability and assurance in the energy supply to the consumers, because the energy production fluctuates with the climatological conditions. For this reason, it is necessary to consider energy storage systems (ESSs) that attenuate fluctuations in power generation and can respond to variations in the demand for energy by consumers, facilitating the supply of power to the grid.

The production of electrical energy from unconventional sources coupled to an energy storage system can be more efficient because they contribute to the reduction of the environmental impact, reducing the carbon footprint and global warming and allow converting back into electrical energy when needed in different periods of time [2].

ESS can be categorized into mechanical (pumped hydroelectric storage, compressed air energy storage, and flywheels), electrochemical (conventional rechargeable batteries and flow batteries), electrical (capacitors, supercapacitors, and superconducting magnetic energy storage), thermochemical (solar fuels), chemical (hydrogen storage with fuel cells), and thermal energy storage (sensible heat storage and latent heat storage) [2]. These differ from each other on their properties, such as the type of primary energy they store, energy density and power density ranges, life cycle, application sector, and the cost of production [3].

In renewable energy–generating devices, such as wind turbines and solar panels, supercapacitors can be used for storing energy to accelerate the turbine after a period with little wind and prevent electrical dropouts in the solar panels. In the case of the transportation sector, batteries, hybrids, and hydrogen are considered as alternatives instead of fossil fuels. Supercapacitors are commonly used in cell phones and computers with backup power for the memory; besides, supercapacitors may also replace the battery in vehicles driven by internal combustion engines [4].

These devices are mainly composed by two electrodes (anode and cathode) and an electrolyte. Carbonaceous materials (carbon gels, biomass, carbon nanotubes, coal, etc.) are one of the most common materials used as electrodes due to their low cost and high superficial area (400–2000 m^2/g), low density (0.3–1 g/cm^3), and good conductivity (5–50 S/cm). The energy storage occurs on the surface of the electrodes, and it could be doped or functionalized to modify their superficial chemistry to improve the energy storage [5].

Nitrogen gas adsorption/desorption at 77 K, thermogravimetric analysis (TGA), differential scanning calorimetry (DSC), immersion calorimetry, X-ray diffraction (XRD), X-ray photoelectron spectra (XPS), scanning electron microscope (SEM), and Fourier-transform infrared (FT-IR) spectroscopy are the most techniques used to characterize porous materials, because they give information about textural, porous and morphology surface, and physical-chemical composition.

Immersion calorimetry is one of the techniques used to determine the textural and chemical characterization of solids like carbonaceous materials. This technique provides information about the interactions that occur between solids and different immersion liquids [6]. The measurement of heats of immersion into liquids with different molecular sizes allows for the assessment of their pore size distribution by measuring the enthalpy of immersion of the samples

into liquids of different critical dimensions. When polar surfaces are analyzed, both the surface accessibility of the immersion liquid and the specific interactions between the solid surface and the molecules of the liquid account for the total value of the heat of immersion [7].

Otherwise, DSC is a thermo-analytical technique in which the difference between the amount of heat required to increase the temperature of a sample and a reference is measured as a function of temperature [8]. DSC profiles provide information about thermal stability and thermal phase transition (transition temperature (T_g), crystalline melting temperature (T_m), and crystallization temperature (T_c) from heating curves (enthalpy; ΔH)). DSC analysis can be used to understand the solid–liquid phase transition of room temperature ionic liquids (RTILs) used in energy storage devices.

In this chapter, the research results founded that the immersion calorimetry and differential scanning calorimetry as characterization techniques of carbonaceous materials for ESS such as supercapacitors will be compiling.

2. Immersion calorimetry of different liquid technique in supercapacitors application

The calorimetric technique is one of the most used techniques to perform the characterization of systems that generate or absorb thermal energy. Isothermal calorimeters exhibit a large heat exchange between the system and the environment. The system in this case is considered as a steel cell in which the liquid adsorbate and the porous material are introduced. Immersion enthalpy is a measure of the amount of heat released when a known mass of a degassed solid is completely immersed in a given liquid; the magnitude of enthalpy depends on the nature of liquid-solid interactions and the extent of available surface.

Alonso et al. [9] activated from the pitch was pyrolysis with KOH at different amount of activating agent. The activated carbons obtained were used as electrodes of supercapacitors. The activated carbons were mainly microporous, while the mesopores increased at higher amount of activating agent. The microporosity of the activated carbons was characterized by measuring the enthalpy of immersion of the samples into liquids with different size. Measurements were carried out at 20°C using dichloromethane (CH_2Cl_2, L = 0.33 nm), benzene (C_6H_6, L = 0.41 nm), cyclohexane (C_6H_{12}), carbon tetrachloride (CCl_4, L = 0.63 nm), and tri-2,4-xylylphosphate (TXP, L = 1.5 nm). The increase of the amount of activating agent caused the immersion enthalpy in the liquid of the smallest size (CH_2Cl_2) to increase from 140 to 281 J/g, which is in agreement with the higher surface developed in the carbons, according to N_2 adsorption isotherm data. In the case of the sample with the lowest activating agent ratio (1/1), the immersion enthalpy in TXP were significantly lower than that obtained for the other liquids (8 J/g, respect to 109–177 J/g), indicating that the TXP molecule is not accessible to the pores developed in this sample ($d_p < 1.5$ nm). In the case of the sample with activating agent/carbon ratio of 2/1, the enthalpy of immersion in TXP was also lower than the rest of the liquids. This indicated that only a small proportion of the pores present in this sample are larger than 1.5 nm. Samples activated with a higher proportion of KOH (3/1 and 5/1) showed very

high values of immersion enthalpy into TXP, which indicated that most of the pores present in these samples are larger than 1.5 nm. The sample activated at activating agent/carbon ratio of 3/1 showed the highest specific capacitances (300–425 F/g) at different current densities (<1–90 mA/cm^2) in H_2SO_4 2 M. This behavior could be associated with the easy diffusion of the electrolyte due to a heterogeneous porous distribution, in accordance with the highest immersion enthalpies values into liquids of different sizes.

Mora et al. [10] obtained activated carbons from mesophase pitch with KOH using different proportions of the activating agent (1:1 to 5:1 KOH to carbon mass ratio) and activation temperatures (600 and 800°C) to study the effect on the textural characteristics of the resultant activated carbons and how these characteristics influenced their behavior as electrodes in supercapacitors. The textural properties of the activated carbons were studied by gas adsorption of N_2 at 77 K and CO_2 at 273 K and immersion calorimetry. Enthalpy of immersion of the samples into liquids of different critical dimensions was used to characterize the microporosity of the activated carbons. Immersion calorimetry measurements were carried out at 20°C using dichloromethane (CH_2Cl_2, L = 0.33 nm), benzene (C_6H_6, L = 0.41 nm), carbon tetrachloride (CCl_4, L = 0.63 nm), tetraisopropyl-o-titanate (TIPOT, L = 1.05 nm), and tetrabutyl-o-titanate (TBOT, L = 1.3 nm). Immersion calorimetry into water was used to estimate the number of hydrophilic sites ($[O+HCl]_{\Delta iH}$) of the carbon surface according to Eq. (1) [11]:

$$[O+HCl]_{\Delta_i H} = \left[0.21\,\Delta_i H_{C_6H_6} - \Delta_i H_{H_2O}\right]/10\ J/mmol \tag{1}$$

The oxygen content is linked with hydrophilic character; samples with high oxygen content showed an increase of hydrophilic sites. Samples were mainly microporous (pore size ~0.9 nm). These samples showed the highest capacitances (200–400 F/g) at low current densities (0.75 mA/cm^2) in 2-M H_2SO_4. However, the sample obtained at 3 of KOH:mesofase ratio and 600°C showed the highest total oxygen content (13.94 wt.%), but it did not show the highest capacity due to an increase of the equivalent series resistance (ESR). The sample activated at 5 of KOH:mesofase ratio and 700°C showed the highest capacitance at low and high current (0.75 and 75 mA/cm^2, respectively). This sample also showed high values of immersion enthalpies into liquids with different size, which suggests the easy access of the electrolyte into the micropores.

Centeno et al. [12] characterized 12 activated carbons with different superficial (378–1270 m^2/g) and porous characteristics (micropore widths between 0.7 and 2 nm). The highest specific capacitance value obtained was 320 F/g using 2-M H_2SO_4 as electrolyte. Eq. (2) shows an empirical correlation obtained between Co, the capacitance C (F/g) at 1 mA/cm^2, and the enthalpy of immersion $\Delta_i H_{C6H6}$ (J/g) at 293 K for 20 microporous carbons.

$$C_o = -k\Delta_i H_{C_6H_6} \tag{2}$$

The deviation of the correlation, with $k = 1.15 \pm 0.1$ (F/J), could be related with specific chemical reactions of the acid with surface groups and to the relatively strong physical interaction between water and the surface oxygen atoms. The enthalpy of immersion of benzene also depends on the

structural parameters such as microporous (S_{mi}) and external (S_e) surface areas and volume (W). Eq. (2) can be used to evaluate empirically the performance of a given carbon as a capacitor.

Sevilla et al. [13] prepared templated mesoporous carbons (TMCs) to be used as supercapacitors. The double layer capacity formed on their surface corresponds to 0.14 F/m^2 in aqueous electrolytes, such as H_2SO_4 and KOH, and 0.06 F/m^2 for the aprotic medium $(C_2H_5)_4NBF_4$/CH_3CN. The effective surface area was determined by independent techniques from Eq. (3): analysis of the nitrogen isotherms by the comparison plot (S_{comp}) and DFT (S_{DFT}) and based on the enthalpy of immersion into dilute aqueous solution of phenol (S_{phenol}) and benzene ($S_{benzene}$).

$$S_{av} = \left(S_{comp} + S_{phenol} + S_{benzene} + S_{DR}\right)/4 \quad (3)$$

The total surface area can be as high as 1500–1600 m^2/g. The relatively low amount of surface oxygen in the present TMCs, as opposed to activated carbons, reduces the contribution of pseudo-capacitance effects and limits the gravimetric capacitance to 200–220 F/g for aqueous electrolytes. In the case of nonaqueous electrolyte, it rarely exceeds 100 F/g. The ionic mobility did not improved due to the mesoporous presence of these TMCs compared with activated carbons of pore widths above 1.0–1.3 nm.

Fernández et al. [14] obtained mesoporous materials from mixtures of poly(vinyl alcohol) with magnesium citrate carbonized and evaluated their performance as electrodes in supercapacitors. The highest specific capacitance (C_o) at low current density (1 mA/cm^2) values was 180 F/g in 2 M H_2SO_4 electrolyte and around 100 F/g in 1 M $(C_2H_5)_4NBF_4$ in acetonitrile. The specific surface area (S_{av}) was calculated as an average of the several specific surface area values; they were estimated by employing different procedures such as comparison plot (S_{comp}) and based on the enthalpy of immersion into phenol (S_{phenol}) and benzene ($S_{benzene}$), according to Eq. (4).

$$S_{av} = \left(S_{comp} + S_{phenol} + S_{benzene}\right)/3 \quad (4)$$

The addition up to approximately 40% of MgO to the raw mixture gradually increased the average specific surface area of the resulting carbons up to approximately 1300 m^2/g. C_o of different mesoporous carbons obtained in aqueous 2-M H_2SO_4 solution and aprotic electrolyte 1-M $(C_2H_5)_4NBF_4/CH_3CN$ were correlated with S_{av}. The relationship of C_o vs. S_{av} showed a linear increase of the limit specified both in an acid medium and aprotic. The lines through the origin correspond to 0.14 F/m^2 in aqueous solution and of 0.07 F/m^2 in the aprotic electrolyte.

Ruiz et al. [15] prepared carbonaceous materials from naphthalene-derived mesophase pitch. These were chemically activated using (3:1) KOH to carbon mass ratio at 700°C for 1 h under nitrogen flow. The activated carbon was thermally treated at 600 and 1000°C under nitrogen flow. The microporosity of the electrodes was characterized by measuring the enthalpy of immersion of the samples into liquids of different critical dimensions. Measurements were carried out at 20°C using dichloromethane (0.33 nm) and tri-2,4-xylylphosphate, TXP (1.5 nm). In the thermal treatment at 600°C, a slight reduction in the capacity to adsorb the nitrogen was showed. The total pore volume was reduced from 0.85 to 0.80 cm^3/g, and microporous surface

area was reduced, S_{mic}, from 1531 to 1407 m^2/g (8% reduction compared to original activated carbon). The thermal treatment at 1000°C generated a decrease of the total pore volume up to 0.66 cm^3/g, and the S_{mic} decreased up to 1318 m^2/g (14%). The average pore size reduced considerably. After thermal treatment, the heat of immersion obtained for CH_2Cl_2 and TXP diminished respect to the original activated carbon for both temperatures, at 600°C from 197 to 206 J/g with CH_2Cl_2 and at 1000°C from 82 to 43 J/g with TXP. These could be related with the presence of constrictions and secondly due to the reduction in the average pore size. The specific capacitance of the original activated carbon was 309 F/g in 1 M H_2SO_4, while the specific capacitance for the activated carbons treated thermally diminished up to 85 F/g for 600°C and 196 F/g for 1000°C. The reason could be the formation of physical constrictions at the entrance of the porous network which makes it more difficult for the electrolyte to gain access.

Olivares-Marín et al. [16] produced activated carbon with KOH from cherry stones wastes for electrode material in supercapacitors. The chemical activation of cherry stones was carried out by different agents such as H_3PO_4, $ZnCl_2$, and KOH. The activated carbons prepared with KOH showed the highest total specific surface area TSA ($S_{mi} + S_e$) (1100–1300 m^2/g) and also the conductivities 1 and 2 S/cm. The materials obtained by carbonization of a mixture of KOH and cherry stones with a ratio 3:1 at 800 and 900°C (carbons K3–800 and K3–900) consists mainly of micropores (width < 2 nm). Their surface areas are respectively 1244 m^2/g and 1039 m^2/g. The carbonaceous material obtained with KOH/cherry stones ratio of 1:1 and 3:1 at 800°C (K1–800 and K3–800) showed similar porosity. However, immersion calorimetry with different molecular probes indicated significant differences in the micropore size distribution. The comparison of the immersion enthalpies into water $\Delta_i H(H_2O)$ and into benzene $\Delta_i H(C_6H_6)$ suggested that the surface oxygen density for cherry stones–based materials varied between 1.2 and 3.0 μmol/m^2. The specific enthalpy of immersion into water, $h_{i[H2O]}$ Eq. (5), was around −0.04 to −0.06 J/m^2.

$$h_{i[H_2O]} = \frac{\Delta_i H_{[H_2O]}}{TSA}[=]\frac{J/g}{m^2/g}[=]\frac{J}{m^2} \tag{5}$$

The specific capacitances values (C) at low current density as high as 230 F/g in aqueous electrolyte 2-M H_2SO_4 and 120 F/g in the aprotic medium 1-M $(C_2H_5)_4NBF_4$/acetonitrile. The correlation between C and TSA showed a specific surface-related capacitance [C (F/g)/TSA (m^2/g)] around 0.17 F/m^2 in H_2SO_4 electrolyte and 0.09 F/m^2 in $(C_2H_5)_4NBF_4$/acetonitrile medium. The highest value in the acidic electrolyte showed an extra contribution from certain functional surface complexes (containing mainly oxygen and nitrogen) in the form of quick oxidation/reduction reactions that promoted the pseudo-capacitance effects to be added to the purely double layer capacitance associated with the surface area. In the case of the aprotic electrolyte, the contribution did practically not depend on the chemistry of the carbon surface.

Garcia-Gomez et al. [17] prepared cylindrical carbon monoliths, and they studied their behavior as electrodes for supercapacitors. The porosity of the carbon monoliths was characterized by N_2 adsorption at 77 K and by immersion calorimetry at 293 K. The total surface area was calculated from the average values of comparison method (S_{comp}), immersion calorimetry into aqueous solution of phenol (S_{phenol}), and the Dubinin-Radushkevich approach (S_{DR}), from Eq. (6) instead of surface area estimated from the BET equation (S_{BET}).

$$S_{av} = \left(S_{comp} + S_{phenol} + S_{DR}\right)/3 \quad (6)$$

S_{BET} underestimates the total surface area for carbons with average micropore size below 0.8–0.9 nm. The interfacial capacitance was 14 μF/cm², obtained in KOH electrolyte, for a specific capacitance of 150 F/g at low current densities (1 mA/cm² or 10 mA/g) and the specific surface area, S_{total} = 1086 m²/g. According to Ref. [18], the double layer capacitance per unit of micropore surface area was found to be very close to that of carbon basal plane (about 15–20 μF/cm²). Moreover, the chemical nature of carbon surface could be estimated from the specific enthalpy of immersion into water $-\Delta_i H_{H2O}$ (J/g). The low value of the $-\Delta_i H_{H2O}/S_{total}$ ratio (−0.023 J/m²) suggests that the monolith surface has nonoxygenated functionalities.

Sánchez-González et al. [19] selected a commercial activated carbon (Norit® C-Granular) and treated it under N_2 at 700, 800, and 900°C during 2 h. The activated carbons were evaluated electrochemically as electrodes of supercapacitors in aqueous (2 M H_2SO_4) and organic (1 M $(C_2H_5)_4NBF_4/CH_3CN$) electrolytes. The microporosity characterization was based on Dubinin's theory, micropore volume (W_o), the average width (L_o) of the locally slit-shaped micropores and the surface area of the micropore walls (S_{mi}), the total pore volume (V_p), and the external surface (S_e) from N_2 adsorption at 77 K isotherm. Other methods such as the comparison plot (S_{comp}) and the density functional theory (S_{DFT}) were used. The average surface area was calculated from Eq. (7).

$$S_{av} = \left(S_{totDR} + S_{comp} + S_{DFT}\right)/3 \quad (7)$$

The density of surface oxygenated functionalities was estimated by the enthalpies of immersion into water and into benzene at 293 K. After heat treatment did not change significantly the pore structure of carbons, the surface oxygen density, presence of carboxylic acid groups, diminished (9.6 to 4.5–5.6 μmol/m²). The commercial activated carbon showed relatively high surface area (727 m²/g) but a poor electrochemical performance in both aqueous and aprotic media. The cyclic voltammograms based on carbons C700–C900 showed a regular box-like behavior of an ideal capacitor. The rectangular shape was well preserved over a wide range of scan rates (1–50 mV/s), which indicates a quick charge propagation. High gravimetric capacitances were obtained from galvanostatic charge–discharge cycling at 1 mA/cm² from 124 to 173 F/g in the aqueous H_2SO_4 electrolyte and around 74–80 F/g in the aprotic medium.

Figure 1 shows a relationship between the surface-related capacitances (C_o/S_{av}) with electric conductivity (S/m). The sample C900 showed the lowest C_o/S_{av} with the highest electric conductivity, and this behavior could be related to the enhancement in the structural order by thermal annealing of the pseudographitic carbonaceous layers. In aqueous and aprotic electrolytes, the sample C900 showed a limited effect on the capacitor capacity for energy storage, but results in power density was almost four times higher than C700.

Zapata-Benabithe et al. [20] obtained carbon aerogels by carbonizing organic aerogels prepared by polycondensation reaction of resorcinol or pyrocatechol with formaldehyde. They are KOH activated at two KOH/carbon ratios to increase pore volume and surface area, and selected samples were surface treated to introduce oxygen and nitrogen functionalities.

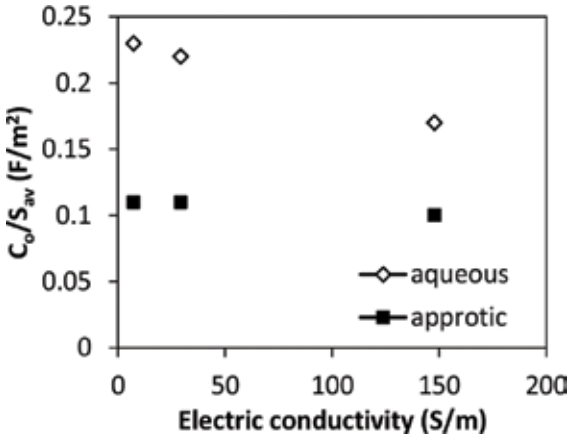

Figure 1. Relationship between the surface-related capacitances and electric conductivity.

The samples were evaluated as electrodes for supercapacitors in 1-M H_2SO_4. The samples were characterized by N_2 and CO_2 adsorption at −196 and 0°C, respectively, immersion calorimetry, temperature-programmed desorption, and X-ray photoelectron spectroscopy in order to determine their surface area, porosity, and surface chemistry. Two series of samples were obtained: one micro-mesoporous and another basically microporous. After KOH activation, the specific surface area (from BET equation) showed values up to 1935 m^2/g. Immersion enthalpies into benzene, $-\Delta H_{benz}$, water, and $-\Delta H_{water}$, were used to determine the hydrophobicity (HF) of the samples according to Eq. (8).

$$HF = 1 - \left(\Delta H_{water}/\Delta H_{benz}\right) \tag{8}$$

The hydrophobicity factor varied between −0.12 and 0.75 for the activated and functionalized carbon aerogels. The relationship between the hydrophobicity and the surface (O_{XPS}) and total (O_{TPD}) oxygen content of the samples diminished linearly with an increase in the oxygen content. The increase of the oxygen content improved the wettability of the carbon surface by the electrolyte, facilitating the EDL formation. However, this advantage can be offset by the binding of oxygen polar groups (mainly carboxyl groups) with water molecules, hindering and retarding the migration of the electrolyte into the pores and thereby increasing the ohmic resistance. One of the samples with the highest gravimetric capacitance in 1-M H_2SO_4, 221 F/g at 0.125 A/g, was obtained with micro-mesoporous characteristics and the highest oxygen functionalities.

Elmouwahidi et al. [21] prepared activated carbons by KOH activation of argan seed shells (ASS), and the activated carbon with the largest surface area was superficially treated to introduce oxygen and nitrogen functionalities. Samples were characterized by N_2 and CO_2 adsorption at −196 and 0°C and immersion calorimetry into benzene and water. Immersion enthalpies into benzene, ΔH_{benz}, were used to determine the surface area of the activated carbons, S_{benz}. Benzene molecule has no specific interactions with surface groups, considering the immersion enthalpy into benzene of a nonporous graphitized carbon black to be 0.114 J/m^2 [22]. The hydrophobicity of samples was determined from Eq. (8). The Dubinin-Radushkevich (DR)

equation was applied to the N_2 and CO_2 isotherms to obtain the micropore volume, $W_0(N_2)$ and $W_0(CO_2)$, respectively. All samples showed $W_0(N_2) > W_0(CO_2)$, indicating an absence of constrictions at micropore entrances and hence complete accessibility to N_2 molecules at −196°C. The apparent surface area (S_{BET}) and S_{benz} values were similar, due to the dimensions of N_2 (0.36 nm) and benzene (0.37 nm) are almost identical, and the micropore width allowed the accommodation of one N_2 monolayer on each micropore wall. The hydrophobicity varied between −0.21 and 0.53 and decreased as a consequence of the fixation of oxygen functionalities with large polarity like carboxyl groups. Activated carbon aerogel superficially treated with oxygen functional groups showed the lowest specific capacitance at 0.125 and 1 A/g and 259 and 135 F/g, respectively, in 1-M H_2SO_4. This behavior could be expressed by the presence of surface carboxyl groups hindering electrolyte diffusion into the highly polar pores.

Zapata-Benabithe et al. [23] studied the effect of the Boron dopant (boric and phenyl boronic acids) and drying method (supercritical, freeze, microwave oven, and vacuum drying) on the surface physics and chemistry of B-doped resorcinol-formaldehyde gels and their electrochemical behavior. The surface characteristics were studied by N_2 and CO_2 adsorption at −196 and 0°C, respectively, and immersion calorimetry into benzene and water. The N_2 adsorption–desorption isotherms at −196°C were type IV and showed a type H2 hysteresis cycle for all B-doped carbon gels obtained. The micropore volume ($W_0(N_2)$) and specific surface area (S_{BET}) values were similar for all samples (~0.23 cm^3/g and 560–590 m^2/g, respectively), except the samples with phenyl boronic acids dried in freeze and vacuum drying oven. This behavior suggests that the drying method has practically no influence on porous characteristics. The surface area from enthalpy of immersion into benzene was determined (S_{imm}) from Eq. (9) and compared with S_{BET} values.

$$S_{C_6H_6} = \frac{\Delta H_{i,C_6H_6}}{\Delta h_{C_6H_6}} \tag{9}$$

The results showed that the $S_{imm} > S_{BET}$ in all samples. The S_{BET} can underestimate with respect to the S_{imm}, because of the restricted diffusion of N_2 at −196°C in very narrow micropores or in those with constrictions at their entrance, whereas benzene molecules can access all micropores because of the much higher temperature (30°C) at which immersion took place.

The gravimetric capacitances (C_{CP}) from chronopotentiometry technique were obtained in aqueous media 1-M H_2SO_4. The interfacial or areal capacitance, IC_{CP}, was calculated from C_{CP} and S_{imm} values. The selection of S_{imm} was due to it gave a more realistic value of the surface area of the B-doped carbon gels. Most of these values are in fairly good agreement with the interfacial capacitance of a clean graphite surface, 20 $\mu F/cm^2$, and with the value range between 20 and 30 $\mu F/cm^2$ reported for different carbons, indicating a good accessibility to the microporosity of the carbon gels.

The relationship between IC_{CP} and S_{imm} for B-doped carbon gels showed a good linear agreement (correlation coefficient of 0.927). The decrease in IC_{CP} with a larger surface area could be explained by the lower EDL capacitance on graphite basal planes versus edges [24]. A rise in the S_{imm} increases the proportion of surface sites on basal planes on the walls

of the slit-shaped micropores versus edge sites mainly on the external surface, reducing the interfacial capacitance. IC_{CP} tends to increase with a higher areal oxygen concentration (O_{XPS}), because of the increase in pseudocapacitance effects produced by the surface oxygen functionalities, enhancing the total capacitance.

3. Differential scanning calorimetry technique in supercapacitors application

Electrochemical energy storage devices operate at room temperature and environment conditions; therefore, differential scanning calorimetry has used to characterize the thermal decomposition behavior of solid polymer electrolytes and electrodes (metal oxides, polymer and carbon) used in supercapacitors applications.

Ghaemi et al. [25] prepared MnO_2 materials (γ and layered types) by a novel ultrasonic aided procedure and studied the charge storage mechanism of the prepared samples as a function of the physisorbed water. The water content of manganese dioxide is considered as one of the key factors in the electrochemical performance of MnO_2. The hydrous regions in the electrode provide the kinetically facile sites needed for the charge-transfer reaction and cation diffusion. To prepare hydrous manganese oxide with different amount of water contents, the samples were thermal treated at 70, 100, and 150°C for 2 h in air. Thermal gravimetric analysis (TGA) and differential scanning calorimetry (DSC) were employed to characterize the water content of the samples. TGA and DSC plots were carried out in air atmosphere with a heating rate of 10°C/min. The DSC analysis showed a wide and steep endothermic peak around 100°C for γ25. The peak was stronger for L25 than γ25 and also shifts toward higher temperature (~125°C) which indicated that the physically adsorbed water is strongly bonded to the porous surface of L25. The heat-treatment temperature decreases the physisorbed water. The cyclic voltammograms (CV) in aqueous 0.5-M Na_2SO_4 electrolyte within a potential window of 0.0 to +1.0 V versus Ag/AgCl, for both samples, showed almost rectangular and symmetric shape characteristics of a supercapacitor. The specific capacitances values from CV, at a scan rate of 5 mV/s in 0.5 M Na_2SO_4 at pH 3.3 and 6, were ranged between 100 and 350 F/g. The specific capacitances values decayed gradually through both increasing solution pH and heat-treatment temperatures. The pseudocapacitance diminished due to a reduction of the amount of physisorbed water, which is associated with a decline of electrochemical active sites within the electrode. The L25 series showed higher specific capacitances values in comparison with γ25, which could be related to the higher amount of the physisorbed water.

Zeng et al. [26] prepared a sheet of Vanadium oxides (V_6O_{13}) from NH_4VO_3 powders to further use it as electrodes of supercapacitors. Vanadium oxides have been widely used as cathode materials for lithium ion battery because of their high-specific capacitance and good cyclability. V_6O_{13} has a blended valence of V(IV) and V(IV) which is favorable for increasing the electronic conductivity of the material and a promising material in supercapacitors because of its lower cost compared to RuO_2. Thermogravimetric and differential scanning calorimeter (TGA–DSC) were used to study the thermal behavior of NH_4VO_3 powders. From TGA

curve, there were two weight losses in the ranges of 185–235°C and 290–320°C, which corresponding to endothermic peaks showed on the DSC curve. An extra endothermic peak centered at 670°C was observed on DSC curve. The melt temperature for V_6O_{13} was considered at 800°C. Electrochemical properties of the prepared samples were determined by cyclic voltammetry (CV) and charge–discharge tests in aqueous electrolyte (1 M $NaNO_3$, KNO_3, Na_2SO_4, and $LiNO_3$). The CV curves showed a relatively like rectangular and symmetrical shape thus indicating ideal capacitive property for V_6O_{13}. The $NaNO_3$ electrolyte exhibited better specific capacitance, 285 F/g (50 mA/g) and 215 F/g (200 mA/g).

Fan et al. [27] developed a novel hierarchical porous carbon membranes using as the source of carbon polyacrylonitrile (PAN), polyvinylpyrrolidone (PVP) as an additive, and N,N-dimethylformamide (DMF) as a solvent. The membranes were prepared with the casting solutions by spin coating coupled with a liquid–liquid phase separation technique at room temperature. The morphology and nanostructure of the membranes were tuned by adjusting the additive concentrations in the casting solutions (0–5 wt.%). Later, the membranes were pre-oxidized, carbonized, and finally modified with nitric acid. Thermogravimetric analysis (TGA) and differential scanning calorimetry (DSC) of the samples were performed in a nitrogen atmosphere with a heating rate of 10°C/min in the temperature range of 25–900°C. The DSC data showed that there were two broad exothermic peaks in ~270 and ~700°C. The significant weight loss stage below ~270°C is mainly due to the loss of crystal water and partial dehydrogenation and cross-linking. The weight loss in the temperature range of 270–470°C can be attributed to the decomposition of PVP in the membrane. At temperature exceeding ~470°C, the weight loss can be assigned to the carbonization of PAN accompanying with further dehydrogenation and partial denitrogenation. The sample prepared with 0.3 wt.% of PVP showed the most reasonable hierarchical pore structure (2–5, 5–50, and >100 nm), high BET surface area (332.9 m^2/g), big total pore volume (0.233 m^3/g), and the best electrochemical performance in 2-M KOH aqueous solution. The specific capacitance was 278 and 206 F/g at 5 and 50 mA/cm^2, respectively, indicating the suitability of the material as electrode materials for supercapacitors.

The desirable properties of polymer electrolytes are high ionic conductivity, good temperature, and environmental stability, as well as thin film processability. However, its conductivity is lower than liquid electrolytes and high sensitivity to water are limitation to become viable materials for electrochemical energy conversion and storage devices [28].

Gao and Lian [28] characterized the structural and thermal behavior of solid polymer electrolyte using poly(vinyl alcohol) (PVA) and studied the factors contributing to the proton conductivity. Two solid polymer electrolytes were prepared mixing a 15 wt.% PVA solution with a heteropoly acid solution at 32.5 wt.%, one with $H_4SiW_{12}O_{40}{\cdot}xH_2O$ (PVA-SWA) and the other one with $H_3PW_{12}O_{40}{\cdot}xH_2O$ (PVA-PWA) and 66 wt.% de-ionized water. The PVA-PWA and PVA-SiWA precursors were combined in equal volumes for a mixed polymer electrolyte (PVA–Mix). Differential scanning calorimetry (DSC) analyses were performed with a scan rate of 10°C/min in nitrogen purged cell over a temperature range from 10 to 150°C. The DSC thermograms for PVA–Mix as well as for its individual components (PVA, PWA, and SiWA) showed that the glass transition temperature (T_g) of pure PVA was found around

84°C. At higher temperatures, there was one endothermic peak for PWA but a split peak for SiWA. In the case of PVA–Mix, two clear endothermic peaks were observed. The water content decreased in the early phase of the temperature scan for all samples. The endothermic peaks could be interpreted as a phase transition or as the escape of certain form of water. The crystallized water in the PVA matrix is more stable than PWA or SiWA, due to the complete release of crystallized protonated water required a higher temperature (122°C for PVA–Mix, respect to 78°C for PVA and 106°C for SiWA). The solid polymer PVA–Mix has been used as an electrolyte with RuO_2/TiO_2 electrodes [29], due to its very good proton conductivity (0.013 S/cm) and stability at environment temperature and relative humidity, forming a solid cell with a thickness of 0.2 mm. At a voltage scan rate of 500 mV/s, the CV profiles were still quite rectangular and showed a capacitance of 50 mF/cm^2 in the cell, which suggests that the electrolyte is viable for high rate capacitive devices. The polymer electrolyte not only acted as proton conductor but also facilitated the oxidation and reduction reactions of the electrodes.

Liew et al. [30] investigated the effect of ionic liquid on the PVA-CH_3COONH_4 polymer electrolytes in supercapacitor application. Ionic liquid-based poly(vinyl alcohol) polymer electrolytes were prepared by means of solution casting. PVA was initially dissolved in distilled water. The weight ratio of PVA:CH_3COONH_4 was kept at 70:30, and different weight ratio of BmImCl (0–60 wt.%) was thus added into the PVA-CH_3COONH_4 mixture to prepare ionic liquid-based polymer electrolyte. The increment of BmImCl enhances the ionic conductivity, due to strong plasticizing effect of ionic liquid. The glass transition temperature (T_g) of the electrolytes was determined from DSC analysis. This study indicated the phase transition of a polymer matrix in the amorphous region, from a hard glassy phase into a flexible and soft rubbery characteristic. The T_g decreased further with addition of ionic liquid. This behavior denoted that the plasticizing effect of CH_3COONH_4 dominates the temporary interactive coordination. This plasticizing effect softens the polymer backbone and thus produces flexible polymer backbone. Polymer electrolyte containing 50 wt.% of BmImCl offered the maximum ionic conductivity of (7.31 ± 0.01) mS/cm at 120°C. The EDLC containing the most conducting polymer electrolyte was assembled and could be charged up to 4.8 V. The specific capacitance of 28.36 F/g was achieved with better electrochemical characteristic in cyclic voltammogram. The higher ion concentration favors the ion migration within the polymer electrolyte (known as separator in EDLC) and promotes the charge accumulation at the electrolyte-electrode boundary. The inclusion of ionic liquid not only improved the interfacial contact between electrode and electrolyte but also increases the electrochemical property of supercapacitors.

Yang et al. [31] obtained a promising ionic liquid-gelled polymer electrolyte (GPE) based on semi-crystal polyvinylidene fluoride (PVDF), amorphous polyvinyl acetate (PVAc), and ionic conductive 1-butyl-3-methylimidazolium tetrafluoroborate (BMIMBF4) via solution-casting method. The thermal stability of the GPEs was measured by thermogravimetric/differential scanning calorimetry (TG/DSC). The PVDF/PVAc/IL (IL, 50 wt.%) GPE film presents good thermal stability (~300°C), wide electrochemical window (>4.0 V), and acceptable ionic conductivity (2.42×10^{-3} S/cm at room temperature) as well. The electrodes were prepared from commercial-activated carbon blended with acetylene black and PTFE at the mass

ratio of 85:10:5 wt.%. The solid-state capacitor was assembled with one piece of electrolyte film was placed on one activated carbon electrode surface, and the other symmetrical electrode was placed over the gel film to form a "Sandwich Structure", subsequently sealed into a commercial CR1016 coin cell mold. A 3.0-V C/C solid-state capacitor cell using this GPE film showed a specific capacitance of 93.3 F/g at the current density of 200 mA/g and could retain more than 90% of the initial capacitance after 5000 charge–discharge cycles.

Peng et al. [32] prepared gel electrolytes from zwitterionic nature of poly (propylsulfonate dimethylammonium propylmethacrylamide) (PPDP) for solid-state supercapacitors. An ideal gel electrolyte should allow a high ion migration rate, reasonable mechanical strength, and robust water retention ability at the solid state for ensuring excellent work durability. The differential scanning calorimetry (DSC) showed PPDP has high water retention ability. No endothermic peak could be observed in the thermogram during the heating of PPDP without water and samples with mole ratio of H_2O to PDP of 6:1 and 7:1 from −35 to 60°C, suggesting that the polyzwitterion itself does not contribute to the thermal transition behavior. However, an endothermic peak is observed as the mole ratio of H_2O to PDP increases to 8:1, which means that the freezable water can be detected in the system when all binding sites of the polyzwitterion are saturated by water molecules. The zwitterionic gel electrolyte were assembled with graphene-based solid-state supercapacitor and reached a volume capacitance of 300.8 F/cm^3 at 0.8 A/cm^3 with a rate capacity of only 14.9% capacitance loss as the current density increases from 0.8 to 20 A/cm^3.

Author details

Zulamita Zapata Benabithe

Address all correspondence to: zulamita.zapata@upb.edu.co

Grupo de Energía y Termodinámica, Facultad de Ingeniería Química, Escuela de Ingeniería, Universidad Pontificia Bolivariana, Antioquia, Colombia

References

[1] Enerdata, Global Energy Statistical Yearbook 2017, France, 2011. https://yearbook.enerdata.net/renewables/renewable-in-electricity-production-share.html

[2] Luo X, Wang J, Dooner M, Clarke J. Overview of current development in electrical energy storage technologies and the application potential in power system operation. Applied Energy. 2015;**137**:511-536. DOI: 10.1016/j.apenergy.2014.09.081

[3] Kötz R, Hahn M, Gallay R. Temperature behavior and impedance fundamentals of supercapacitors. Journal of Power Sources. 2006;**154**:550-555. DOI: 10.1016/j.jpowsour.2005.10.048

[4] Hauge HH, Presser V, Burheim O. In-situ and ex-situ measurements of thermal conductivity of supercapacitors. Energy. 2014;**78**:373-383. DOI: 10.1016/j.energy.2014.10.022

[5] Lota G, Centeno T, Frackowiak E, Stoeckli F. Improvement of the structural and chemical properties of a commercial activated carbon for its application in electrochemical capacitors. Electrochimica Acta. 2008;**53**:2210-2216. DOI: 10.1016/j.electacta.2007.09.028

[6] Vargas DP, Giraldo L, Moreno-Piraján JC. Calorimetric study of functionalized carbonaceous materials. Thermochimica Acta. 2015;**611**:20-25

[7] Silvestre-Albero J, Gómez de Salazar C, Sepúlveda-Escribano A, Rodríguez-Reinoso F. Characterization of microporous solids by immersion calorimetry. Colloids and Surfaces A: Physicochemical and Engineering Aspects. 2001;**187-188**:151-165. DOI: 10.1016/S0927-7757(01)00620-3

[8] Höhne G, Hemminger W, Flammersheim H-J. Differential Scanning Calorimetry. 2nd ed. Berlin: Springer; 2003

[9] Alonso A, Ruiz V, Blanco C, Santamaría R, Granda M, Menéndez R, et al. Activated carbon produced from Sasol-Lurgi gasifier pitch and its application as electrodes in supercapacitors. Carbon New York. 2006;**44**:441-446. DOI: 10.1016/j.carbon.2005.09.008

[10] Mora E, Ruiz V, Santamaría R, Blanco C, Granda M, Menéndez R, et al. Influence of mesophase activation conditions on the specific capacitance of the resulting carbons. Journal of Power Sources. 2006;**156**:719-724. DOI: 10.1016/j.jpowsour.2005.06.025

[11] Stoeckli F. Water adsorption in activated carbons of various degrees of oxidation described by the Dubinin equation. Carbon New York. 2002;**40**:969-971. DOI: 10.1016/S0008-6223(02)00087-8

[12] Centeno TAT, Stoeckli F. On the specific double-layer capacitance of activated carbons, in relation to their structural and chemical properties. Journal of Power Sources. 2006;**154**:314-320. DOI: 10.1016/j.jpowsour.2005.04.007

[13] Sevilla M, Álvarez S, Centeno TA, Fuertes AB, Stoeckli F. Performance of templated mesoporous carbons in supercapacitors. Electrochimica Acta. 2007;**52**:3207-3215. DOI: 10.1016/j.electacta.2006.09.063

[14] Fernández JA, Morishita T, Toyoda M, Inagaki M, Stoeckli F, Centeno TA. Performance of mesoporous carbons derived from poly(vinyl alcohol) in electrochemical capacitors. Journal of Power Sources. 2008;**175**:675-679. DOI: 10.1016/j.jpowsour.2007.09.042

[15] Ruiz V, Blanco C, Granda M, Menéndez R, Santamaría R. Effect of the thermal treatment of carbon-based electrodes on the electrochemical performance of supercapacitors. Journal of Electroanalytical Chemistry. 2008;**618**:17-23. DOI: 10.1016/j.jelechem.2008.02.016

[16] Olivares-Marín M, Fernández JA, Lázaro MJ, Fernández-González C, Macías-García A, Gómez-Serrano V, et al. Cherry stones as precursor of activated carbons for supercapacitors. Materials Chemistry and Physics. 2009;**114**:323-327. DOI: 10.1016/j.matchemphys.2008.09.010

[17] Garcia-Gomez A, Miles P, Centeno TA, Rojo JM. Uniaxially oriented carbon monoliths as supercapacitor electrodes. Electrochimica Acta. 2010;**55**:8539-8544. DOI: 10.1016/j.electacta.2010.07.072

[18] Shi H. Activated carbons and double layer capacitance. Electrochimica Acta. 1996;**41**: 1633-1639. DOI: 10.1016/0013-4686(95)00416-5

[19] Sánchez-González J, Stoeckli F, Centeno TA. The role of the electric conductivity of carbons in the electrochemical capacitor performance. Journal of Electroanalytical Chemistry. 2011;**657**:176-180. DOI: 10.1016/j.jelechem.2011.03.025

[20] Zapata-Benabithe Z, Carrasco-Marín F, Moreno-Castilla C. Preparation, surface characteristics, and electrochemical double-layer capacitance of KOH-activated carbon aerogels and their O- and N-doped derivatives. Journal of Power Sources. 2012;**219**:80-88. DOI: 10.1016/j.jpowsour.2012.07.0

[21] Elmouwahidi A, Zapata-Benabithe Z, Carrasco-Marín F, Moreno-Castilla C. Activated carbons from KOH-activation of argan (Argania spinosa) seed shells as supercapacitor electrodes. Bioresource Technology. 2012;**111**:185-190. DOI: 10.1016/j.biortech.2012.02.010

[22] Denoyel R, Fernandez-Colinas J, Grillet Y, Rouquerol J. Assessment of the surface area and microporosity of activated charcoals from immersion calorimetry and nitrogen adsorption data. Langmuir. 1993;**9**:515-518. DOI: 10.1021/la00026a025

[23] Zapata-Benabithe Z, Moreno-Castilla C, Carrasco-Marín F. Influence of the boron precursor and drying method on surface properties and electrochemical behavior of boron-doped carbon gels. Langmuir. 2014;**30**:1716-1722. DOI: 10.1021/la404667y

[24] Kinoshita K. Carbon, Electrochemical and Physicochemical Properties. Canada: John Wiley & Sons, Inc; 1988

[25] Ghaemi M, Ataherian F, Zolfaghari A, Jafari SM. Charge storage mechanism of sonochemically prepared MnO2 as supercapacitor electrode: Effects of physisorbed water and proton conduction. Electrochimica Acta. 2008;**53**:4607-4614. DOI: 10.1016/j.electacta.2007.12.040

[26] Zeng HM, Zhao Y, Hao YJ, Lai QY, Huang JH, Ji XY. Preparation and capacitive properties of sheet V6O13 for electrochemical supercapacitor. Journal of Alloys and Compounds. 2009;**477**:800-804. DOI: 10.1016/j.jallcom.2008.10.100

[27] Fan H, Ran F, Zhang X, Song H, Jing W, Shen K, et al. A hierarchical porous carbon membrane from polyacrylonitrile/polyvinylpyrrolidone blending membranes: Preparation, characterization and electrochemical capacitive performance. Journal of Energy Chemistry. 2014;**23**:684-693. DOI: 10.1016/S2095-4956(14)60200-X

[28] Gao H, Lian K. Characterizations of proton conducting polymer electrolytes for electrochemical capacitors. Electrochimica Acta. 2010;**56**:122-127. DOI: 10.1016/j.electacta.2010.09.036

[29] Gao H, Tian Q, Lian K. Polyvinyl alcohol-heteropoly acid polymer electrolytes and their applications in electrochemical capacitors. Solid State Ionics. 2010;**181**:874-876. DOI: 10.1016/j.ssi.2010.05.006

[30] Liew CW, Ramesh S, Arof AK. Good prospect of ionic liquid based-poly(vinyl alcohol) polymer electrolytes for supercapacitors with excellent electrical, electrochemical and thermal properties. International Journal of Hydrogen Energy. 2014;**39**:2953-2963. DOI: 10.1016/j.ijhydene.2013.06.061

[31] Yang L, Hu J, Lei G, Liu H. Ionic liquid-gelled polyvinylidene fluoride/polyvinyl acetate polymer electrolyte for solid supercapacitor. Chemical Engineering Journal. 2014;**258**:320-326. DOI: 10.1016/j.cej.2014.05.149

[32] Peng X, Liu H, Yin Q, Wu J, Chen P, Zhang G, et al. A zwitterionic gel electrolyte for efficient solid-state supercapacitors. Nature Communications. 2016;**7**:11782. DOI: 10.1038/ncomms11782

Chapter 5

Battery Efficiency Measurement for Electrical Vehicle and Smart Grid Applications Using Isothermal Calorimeter: Method, Design, Theory and Results

Mohammad Rezwan Khan

Additional information is available at the end of the chapter

http://dx.doi.org/10.5772/intechopen.75896

Abstract

The chapter primarily explores the likelihood of heat measurement by means of the calorimeter in the lithium-ion battery cells for different applications. The presented focus applications are electrical vehicle and smart grid application. The efficiency parameter for battery cell is established using state of the art isothermal calorimeter by taking the consideration of heat related measurement. The calorimeter is principally used for the determination of the heat flux of the battery cell. The main target is to achieve the precision and accuracy of measurement of battery cell thermal performance. In this chapter, the assessment of battery efficiency parameter is proposed. A newly devised efficiency calculation methodology is projected and illustrated. The procedure ensures the precision an accurate measurement of heat flux measurement and turns into more comparable efficiency parameter. In addition, the issue is to investigate thermal sensitivity to factors that influence the energy storage system performance, i.e., current rate and temperature requirements. The results provide insight into the establishment of new key performance indicator (KPI) efficiency specification of the battery system. The usage of the calorimetric experiments is presented to predict the temperature distribution over a battery cell and an array of cells.

Keywords: battery systems, calorimeter, isothermal calorimeter, heat flux, efficiency, key performance indicator, electrical vehicle, smart grid, battery thermal management, heat generation, performance and battery behavior, key performance indicator (KPI)

1. Literature study

Sustainable low-carbon economy yet resource-efficient and competitive is a top-priority in the international community. Focusing on emissions, transport sectors, are some of the largest and

fastest-growing contributors to greenhouse gas (GHG). This is omnipresent in the whole world, where significant emissions reductions in transport and grid sectors, are needed to meet long-standing climate goals. Scientific studies have often directed to renewable energies coupled with batteries for cuts in GHG emissions [1, 2]. There is no doubt of the fact that adopting electric technologies in the transport industry, therefore, makes the highest potential since it is an achievable option in current status quo. There are however more technological as well as structural challenges to overcome [3].

There is no denying of the fact that battery technology, for instance, Lithium-ion battery technology offers great benefits in current energy scenario. However, an essential challenge is to safeguard working safety, reliability and cost, etc. State of the art lithium-ion batteries is prone to temperature related problems. In order for EVs like PHEVs, BEVs technologies to succeed in the marketplace, the strict requirement is placed on being very safe and reliable. Therefore, either the consequences of a heat-related hazard, for instance, thermal runaway or the severity of a thermal runaway reaction must be minimized under both normal operations and abusive conditions [4–6]. Undoubtedly, battery thermal management system (BTMS) is critical to the life and performance of electric-drive vehicles (EDVs) hybrids (HEVs), plug-in hybrids (PHEVs), and all-electric vehicles (EVs). The lithium-ion (Li-ion) batteries found in most of today's electric-drive vehicles are smaller and more lightweight than previous nickel-metal hydride (NiMH) technology, but they are also more sensitive to overheating, overcharging, and extreme spikes in temperature known as thermal runaway [7, 8]. A comparison is presented in **Table 1**.

In extreme instances, battery overheating can pose safety hazards, including fires. The important performance assessments factors are management system, the thermal behavior of the cell, battery lifespan, and safety of the energy storage system, as well as full integration into an application. While designing the thermal system EV and HEV performance and life-cycle cost are seriously affected by battery pack performance, i.e., the pack's operating temperature profile. The effect is mainly uneven temperature distribution [7, 9]. It may direct unbalanced modules and reduced performance in a battery pack [10]. Therefore, it is no surprise that manufacturers seek battery cells with a safe thermal profile so that modules operate within the desired range. Another important goal is that HEVs, PHEVs, and BEVs batteries need to operate at maximum efficiency to attain ultimate market penetration [4, 11, 12]. Though the performance is influenced by a wide range of driving conditions and climates, and through numerous charging cycles, high temperatures decrease battery life [13]. So, it increases battery replacement costs, while low temperatures diminish battery power and capacity, all of which impact required applications operational range, performance, and affordability. So, it is imperative to conduct the thermal management research and development (R&D) to optimize battery performance and extend the life of battery [14, 15]. Undeniably to become a recognized leader in battery research and development, thermal analysis and characterization specifically with calorimeter is necessary. Through calorimetric testing, it is necessary to evaluate the thermal performance of battery cells. Then the result is extending further to modules and packs by strict inspection [7, 16, 17].

Current battery breakthrough research is focused on reducing thermal barriers to achieve more uniform temperatures. One of the important attributes is being capable of precise thermal measurements with great accuracy. It should enable battery developers to predict thermal

http://dx.doi.org/10.5772/intechopen.75896

Specifications	Non- lithium Batteries			Lithium Based Cells		
	Lead Acid (PbAc)	Nickel–cadmium (Ni Cd)	Nickel–metal hydride (NiMH)	Lithium cobalt oxide (LCO)	Lithium manganese oxide (LMO)	Lithium phosphate (LFP)
Specific energy (Wh/kg)	30-50	45-80	60-120	150-190	100-135	90-120
Internal resistance (mΩ)	<100	100-200	200-300	150-300	25-75	25-50
Cycle life' (80% DoD)	200-300	1000	300-500	500-1000	500-1000	1000-2000
Fast-charge time	8-16h	1h	2-4h	2-4h	1h or less	1h or less
Overcharge tolerance	High	Moderate	Low	Low	Low	Low
Self-discharge/ month (room temp)	5%	20%	30%	5-10%	2-10%	1-10%
Cell voltage (nominal)	2V	1.2V	1.2V	3.6V	3.8V	3.3V
Charge temperature	-20°C to 50°C	0°C to 45°C	0°C to 45°C	0°C to 45°C	0°C to 45°C	0°C to 45°C
Discharge temperature	-20°C to 50°C	0°C to 45°C	0°C to 45°C	0°C to 45°C	0°C to 45°C	0°C to 45°C
Commercialization year Since	Late 1800s	1950	1990	1991	1996	1999

Table 1. Common batteries used in electric vehicle and smart grid applications.

performance before installing batteries in vehicles [18]. Manufacturers use these metrics to compare battery performance to industry averages, troubleshoot thermal issues, and fine-tune their designs in successive iterations. The measuring principles might rely on precise measurement of energy storage devices' heat generation and efficiency under different states of charge, power profiles, and temperatures [19, 20]. In general, Calorimetry means the measurement of heat. Only one single energy (the internal energy) stored in the battery, which—only during an exchange—appears in a variety of energy forms such as heat energy. Accordingly, the form of energy known as heat can only be conceived as coupled with a change of energy. In other words, heat is the amount of energy exchanged within a given time interval in the form of heat flow from a battery specimen as measured by the calorimeter. The precise measurement of battery's heat capacity, the heat of fusion, the heat of reaction, and other caloric quantities is the foundations for progress in battery research and development. As a result, there is now an increasing interest in calorimetry as a very easy and powerful method for different kinds of investigation. Heat and temperature uniformity affect the battery application performance, lifecycle, and security [12, 21, 22].

Calorimeters are used for measuring the heat of chemical reactions or physical changes inside a battery cell or a module. The underlying techniques are based on measuring heat generated from the exothermic process, consumed from the endothermic process or simply dissipated by

a battery cell or module at controlled temperatures with a controlled environment. It provides an accurate assessment of heat-evolution and thermal foot-print of the battery cell or the pack [23–25]. A variety of calorimetry techniques are found to characterize energy storage systems. Accelerating rate calorimetry (ARC) is used to quantify calorific output and heating rates for runaway reactions in lithium-ion cells. It is used to evaluate materials and strategies to minimize the severity of these reactions. In addition, it is possible to understand better the degradation products, mechanisms, and potential hazards associated with degrading battery materials. Another technique is isothermal calorimetry used to measure cell or battery heat capacity and heat generation during charge/discharge profiles [26, 27]. This information retrieved from the calorimeter can be used to model, design, and test the performance of a battery's thermal management system. Through calorimetry, it is possible to determine the temperature at which lithium-ion cells, the quantity of energy released during the operation of the battery, the associated reaction speed. Isothermal battery calorimeters (IBCs) are capable of providing the precise thermal measurements needed for safer, longer-lasting, and more cost-effective electric vehicle (EV) batteries [28].

Development of precisely calibrated battery systems relies on accurate calorimetric measurements of heat generated by battery cell or modules during the full range of charge/discharge cycles. Moreover, it is important of the determination of whether the heat is generated electrochemically or resistively. The calorimeter must determine the heat levels and battery energy efficiency with greater accuracy. Additionally, it should provide precise measurements through complete thermal isolation to ensure the heat measured is entirely from the battery cell. Besides, it is needed to analyze heat loads generated by complete battery systems [24, 25, 29, 30]. Three typical calorimeter configurations are presented in **Table 2**.

The evolution of surface temperature distribution and the heat flux of the battery cell is measured at the same time. Temperatures on the surface of the cell are measured using contact thermocouples, whereas, the heat flux is measured simultaneously by the isothermal calorimeter. This heat flux measurement is used for determining the heat generation inside the cell.

Specifications	Units	IBC 284 (Cell)	Module IBC	Large-Volume IBC (Pack)
Maximum Voltage	Volts (V)	50	500	600
Sustained Maximum Current	Amps (A)	250	250	450
Excursion Currents	Amps (A)	300	300	1,000
Volume	Litre (L)	9.4	14.7	96
Maximum Dimensions	(cm)	20.3 x 20.3 x 15.2	35 x 21 x 20	60 x 40 x 40
Operating Temperature	(°C)	-30 to 60	-30 to 60	-40 to 100
Maximum Constant Heat Generation	Watt (W)	50	150	4,000

Table 2. Commercial calorimeter configurations used for EV and smart grid application.

Consequently, using the heat generation result, the important performance constituent, i.e., key performance indicator (KPI) of the battery cell—efficiency is calculated. Those are accomplished at different temperature levels (−5°C, 10°C, 25°C and 40°C) of continuous charge and discharge constant current rate (1°C, 2°C, 4°C, 8°C). There is a significant change in heat generation level in both charge and discharge events on decreasing temperature and increasing C-rate. The heat flux magnitude level change is non-linear at different temperature and current rate. This nonlinear heat flux is responsible for the corresponding nonlinear change of efficiency in different C-rate at a particular temperature. The results lead to a deeper understanding of the efficiency and heat generation behavior of the specific battery cell. Additionally, the result of the research can be incorporated in constructing a precise datasheet of a specific type of battery cell which can assist the researchers, engineers, and different stakeholders to enhance diverse aspects of battery research [29, 31]. Inevitably identifying and understanding those behaviors and performance indicators are critical to ensuring the proper operation of the battery [29, 31]. The knowledge of the individual cell heat generation can give a good indication of the behavior inside a pack.

Therefore, it is evident that understanding the temperature gradients, its evolution and finding key performance indicator (KPI), i.e., efficiency of the battery is very important. It assists in choosing the required efficient battery cell for a specific application. This can provide very valuable information on the characteristics of the battery. Furthermore, the results can be used to build a thermal model. Moreover, the research can assist in the process of design selection from different cooling options. Additionally, it can lead to choosing the optimal battery cell for desired application from diverse options to choose the optimum battery. The specific method and the use of the method are presented in the subsequent sections of this chapter.

2. Underlying physics and methodology development

2.1. Physics behind isothermal battery calorimetry

The term isothermal refers to a fixed temperature in equilibrium thermodynamics. Strictly speaking, the temperature of isothermal calorimeters must be kept constant in every part and every moment. But in such a case, no heat transport would occur since heat only can flow when a temperature gradient (difference) exists. Therefore, at least the battery sample temperature must be dissimilar from the (isothermal) calorimeter temperature. Hence, it is more quasi-isothermal rather than only isothermal. Furthermore, the heat produced during a reaction inside a battery cell in such a calorimeter must be compensated for immediately in one way or the other. There are two possibilities to compensate for the heat produced by the battery sample [26, 27, 32]. The heat released from a battery sample during a process flows into the calorimeter and would cause a temperature change of the latter as a measuring effect; this thermal effect is continuously suppressed by compensating the respective heat flow. The methods of compensation include the use of "latent heat" caused by a phase transition, thermoelectric effects, heats of chemical reactions, a change in the pressure of an ideal gas [33], and heat exchange with a liquid [34].

2.1.1. Summary of measuring principles

Measurement of the heat exchanged while a battery in operation by compensation, that is, suppression of any temperature change of the calorimeter caused by the thermal effect of the battery sample. The underlying compensation principle is:

- By endothermic effect
- By exothermic effect
- Phase transition (solid-liquid; liquid–gaseous, liquid-solid, gaseous–liquid, etc.
- Electric cooling (Peltier effect)
- Electric heating (Joule effect)

2.1.2. The isothermal condition

In calorimeters operating isothermally, the surroundings and the measuring system always have the same constant temperature. Consequently, isothermal operation necessitates a compensation of the heat flow released from the battery sample. This can be achieved by a phase transition (passive measuring system) or by thermoelectric effects (active measuring system). There are no truly isothermal conditions in the measuring system of a compensation calorimeter, least of all in the battery sample. Constant temperature in time and space cannot be expected because any heat transport from the battery sample to the substance undergoing transition would be impossible in the absence of temperature differences. Similar considerations apply to calorimeters involving electric compensation about the heat transport between the battery sample, the temperature sensor, and the heater or the cooler. The magnitude of the temperature difference depends on the quantity of heat delivered per time unit by the battery sample surface, the thermal conductivities of the substances that surround the battery sample (vessel materials), and their geometry. In calorimeters involving electric compensation, the insulation of the temperature sensors and of the heating or cooling elements causes additional local temperature differences. Despite these limitations, the designation "isothermal" is commonly used with regard to calorimeters. Calorimetric measurement and data processing (evaluation), as well as calorimeter control, are nowadays carried out electronically and with the help of a computer. In most cases, the computer ultimately presents the result of the measurement graphically for the sake of clarity and in order to make any change of test values readily visible [23, 35, 36]. The heat produced (or consumed) brings about a change of temperature, which in turn causes a heat flow and other effects. A sensor (thermometer) located within or outside the reaction vessel detects a temperature change that occurs with some time lag relative to the reaction proper and can be only loosely correlated with the course of the chemical reaction because of the uncontrollable character of such phenomena as diffusion, convection, and heat conduction in the liquid. However, if sufficient time is allowed for all equalization processes to go to completion, it becomes evident that the overall temperature change is closely related to the overall heat of reaction [23–26, 30].

http://dx.doi.org/10.5772/intechopen.75896

2.2. The methodology

The research associates with the determination of heat generation and efficiency of a battery cell using an experimental approach. It is accomplished through applying a full charge and discharge current at different rates in diverse temperatures. During the experiment, the principal thermal features of the battery cell are measured simultaneously. Those are battery cell raw heat flux (measured using isothermal calorimeter) and surface temperature (measured using contact thermocouples) at different spots. Those are simultaneously measured to track the thermal gradients on the surface of the battery as well as to track the heat generation rate. Calorimetric measurement represents the global heat generation inside the cell at the given current profile. By using this calorimetric raw heat flux data, the quantity of the battery heat generation is determined. To accomplish this, a suitable range of raw heat flux is carefully chosen. The next procedure is to select the best baseline type. It is needed for finding the enclosed heat flux area. Then using computational software, the actual heat generation is determined. Afterwards, using the electrical energy input (area enclosed by electric power versus time curve) and calorimetric heat dissipation data (area enclosed by heat flux versus time curve), the efficiency of the battery cell is calculated at the corresponding operating condition. Simultaneously, the maximal increase in the battery temperature inside cell surface is measured for different current rates on the battery cell surface [5, 6]. The calorimetric data is used to model the cooling effect inside a battery cell and an array of cells inside a pack.

2.3. Calorimetric experimental steps

Obtaining reliable experimental results needs painstaking preparation stages. Those are discussed in the subsequent subsection.

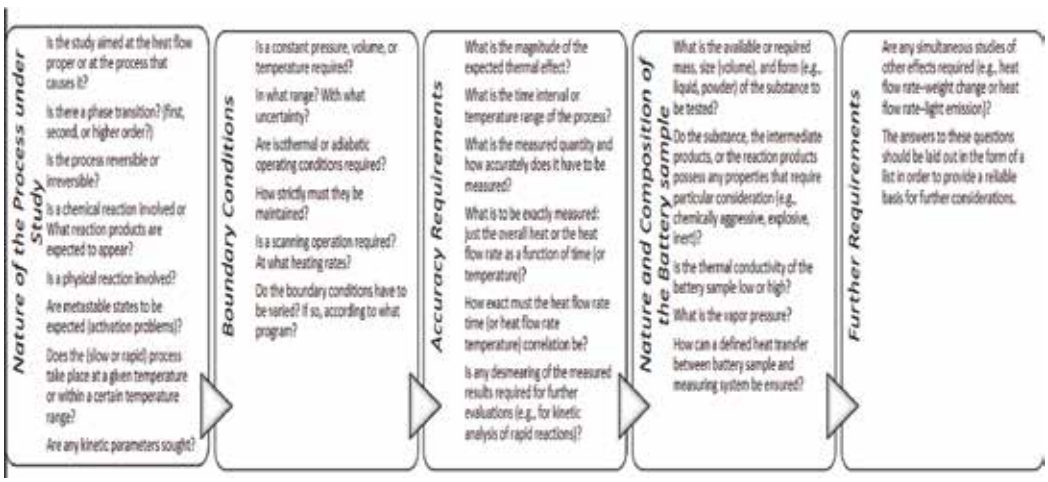

Figure 1. Selection of a suitable calorimeter using the queries.

2.3.1. Definition of the problem to be investigated

Calorimetric procedures provide valuable information toward an understanding of processes where the enthalpy remains constant (i.e., there is no exchange of heat), but one of the derivatives of enthalpy with regard to temperature (e.g., the first derivative—the heat capacity) undergoes a change during the process. The answers to these questions should be laid out in the form of a list in order to provide a reliable basis for further considerations as presented in **Figure 1**.

2.3.2. Calorimeter requirements

The requirements with regard to a calorimeter can be derived on the basis of the analysis of the measuring problem.

- Find the necessary operating conditions: isothermal, adiabatic
- Define the temperature range
- Find the required heating rate
- Determine boundary conditions: a constant pressure, constant volume, gas flow rate, and so on
- Find the required noise and accuracy level
- Determine the safety and security risk level

3. Calorimetric measurement

3.1. Calibration and setup of the experiment

Before starting an experiment, the calorimeter must be carefully calibrated. The calibration should be verified from time to time (depending on the stability of the instrument). In case of higher accuracy demands, such verification is to be recommended before and after every experiment to be on the safe side regarding the reliability of the calorimetric results. After the insertion of the battery sample into the calorimeter, enough time must be given to the instrument to come to a stable state and thermal equilibrium before the measurement can be started. Proper measurement parameters must be chosen: in the case of calorimetry, the initial temperature and the heat flux measurements have come to steady-state conditions (by putting the machine in idle condition for sufficient time) before the event to be investigated starts. The quantities temperature, time, and heat flow rate, must be measured and stored for later analysis. Additionally, the analog-to-digital converter must have the proper resolution and precision to fulfill the uncertainty demands of the measurement [28]. The battery cell temperature measurement system is made of five type K thermocouples. The Isothermal Battery Calorimeter Netzsch™ IBC 284 is a robust instrument designed for the accurate measurement of heat flux generated by batteries while in operation. It has an operating span of −30°C to +60°C.

http://dx.doi.org/10.5772/intechopen.75896

A mixture of 50% ethylene glycol and 50% deionized water (EG/W) is used inside the bath. It ensures the isothermal environment inside the bath. The following **Table 3** lists the specification of the calorimeter.

The instrument is semi-automated. Most of the operations are controlled manually from the front panel of LabVIEW-based data acquisition system. It has a heat sensing range from 100 mW to 50 W. It should be noted that the calorimeter has high thermal inertia. It limits the calorimeter's heating or cooling rate. A maximum of 5 K per hour rate can be reached. For instance, when starting from 25°C, for an experiment to be run at 40°C, so it may take minimum 3 h to reach temperature equilibrium. Image of the calorimeter are shown in **Figure 2** [29, 31].

Attribute	Limit	Attribute	Limit
Temperature range	-30°C to +60°C	Maximum battery size	305 [mm] x 203.2 [mm] x 152.4 [mm]
Isothermal bath stability	±0.01°C	Baseline noise	5 mW
Heating / Cooling rate	5°C / hour	Baseline stability	30 mW
Refrigerated Recirculation	Built-in to unit	Maximum power	50 W
Thermal fluid	Ethylene glycol / deionized water	Maximum current	250A
Operational mode	Isothermal for measurement of battery enthalpic and entropic changes, efficiency, lifetime and performance	Maximum voltage	50V

Table 3. Netzsch™ IBC 284 calorimeter specification.

Figure 2. Netzsch™ IBC 284 isothermal calorimeter used in the chapter for measuring the thermal behavior of battery cells.

The calibration factor for heat or heat flow rate must be determined or verified. The measured temperature is checked in a variety of ways depending on the calorimeter, and the same applies to the information on temperature fluctuations. Heat flows are invariably associated with a temperature gradient whose magnitude must be taken into account in order to be able to analyze the accuracy of temperature measurement. The determination or checking of the calibration factor usually takes place through the release of a definite amount of heat in an electric heater (resistor). The test measurements are made to find the repeatability and the accuracy of the calorimeter [28]. The specific calibration is carried out using the precision resistance. It is provided with the calorimeter instrument. It is accomplished by applying three different Joule effect pulses. The goal of this particular calibration is to calibrate the heat flux measurement as closely as possible to the known amount of heat flux generation. Joule effect calibration is found in **Figure 3** [29, 31].

In the current experimental condition, a particular precision resistance is used. It generates a 50 mV voltage for 300 A current and having a resistance value of 0.167 mΩ. Calibration of the calorimeter is accomplished by applying a controlled electrical current to this accurate resistance located inside the calorimeter chamber. The power of the different Joule effect pulses, applied in the precision resistance placed inside calorimeter chamber, is adapted for the measuring range of the instrument (100 mW to 50 W). The calibration is also performed at many different temperatures (−30°C, 0°C, +30°C or +60°C) [29, 31].The standard calibration is comprised of three successive Joule effect pulses at different levels of power 100 mW, 1 W, and 10 W. The goal of this particular calibration would be to obtain the exact calibration coefficient for the specific temperature of the experiment. From different calibration points, various calibration coefficients are calculated. Consequently, a calibration polynomial can be generated as shown in **Figure 4**.

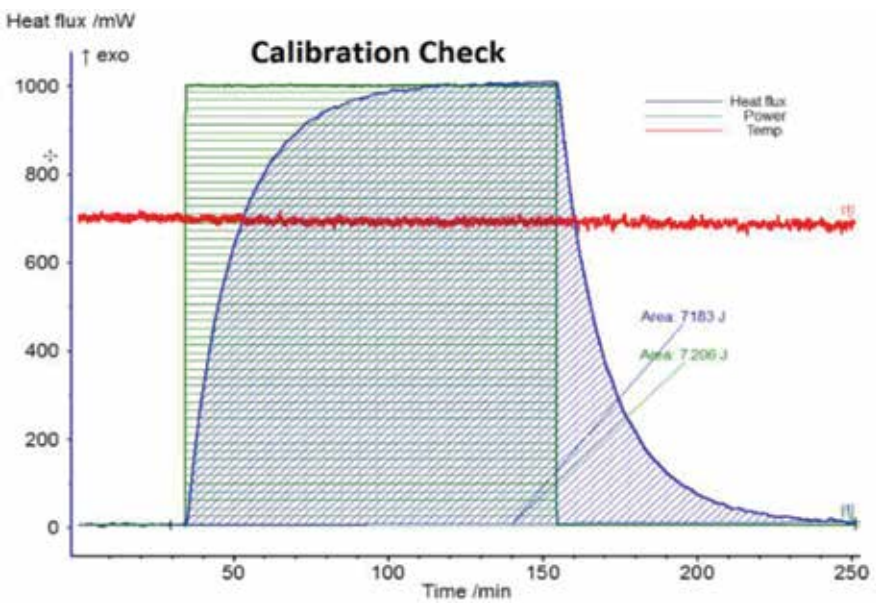

Figure 3. Joule effect calibration graphs [29, 31].

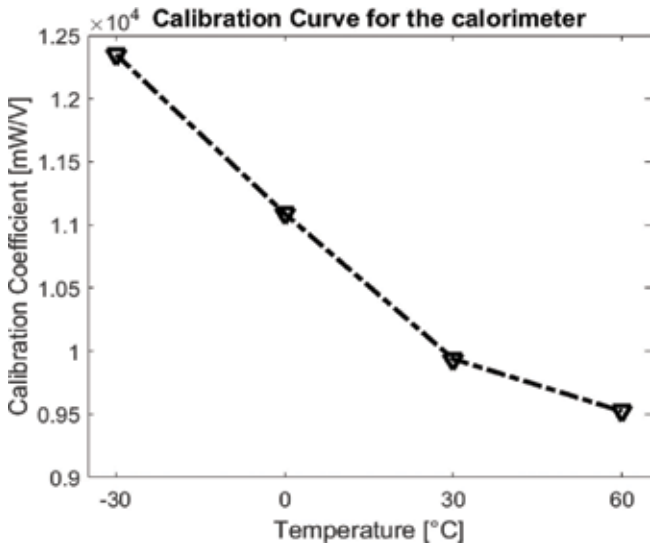

Figure 4. Calibration curve of the calorimeter [29, 31].

Most of the experiments need to be run at temperatures other than the temperatures (−30°C, 0°C, +30°C or +60°C) that the calorimeter was calibrated. In that case, to obtain a good accuracy, a calibration polynomial is used. The polynomial is used for interpolating the coefficient on the intermediate temperature levels. It should be noted that using the calibration polynomial for calculating the calibration coefficient at the particular temperature may lead to an error of less than 1. The resulting calibration polynomial equation expresses the calibration coefficient as a function of temperature (in °C) as shown in Eq. (1):

$$\text{Calibration coefficient } (T) = 0.0039T^3 + 0.0594T^2 - 43.709T + 11090 \quad (1)$$

3.2. Battery calorimetric experiment

The inert gas atmosphere is maintained inside the calorimeter chamber. To achieve excellent temperature homogeneity (inside the isothermal bath), constant stirring is needed in the experimental condition. Before electrically connecting the battery sample inside the calorimeter, the battery cell sample needs to be prepared. To be tested, the battery sample needs to be equipped with two wires for powering purpose and two wires for sensing. The thermal contact between the battery sample and the calorimeter is the most important factor for obtaining the accurate data. This ensures efficient heat transfer between the battery itself and the bottom plate of the calorimeter. It is to be noted that the thermoelectric sensors are located underneath of the battery chamber. After performing the calibration and experimental conditioning, the battery sample is electrically connected with battery cycler. The experiment is repeated at different temperature at the different current rate. After acquiring the data, Netzsch™ Proteus® Software and hand optimized Matlab® script is used for the thermal analysis. After selecting the proper baseline and the range, using the computational software, the enclosed area is found (refer to **Figure 5**) which represents the heat flux area [29, 31].

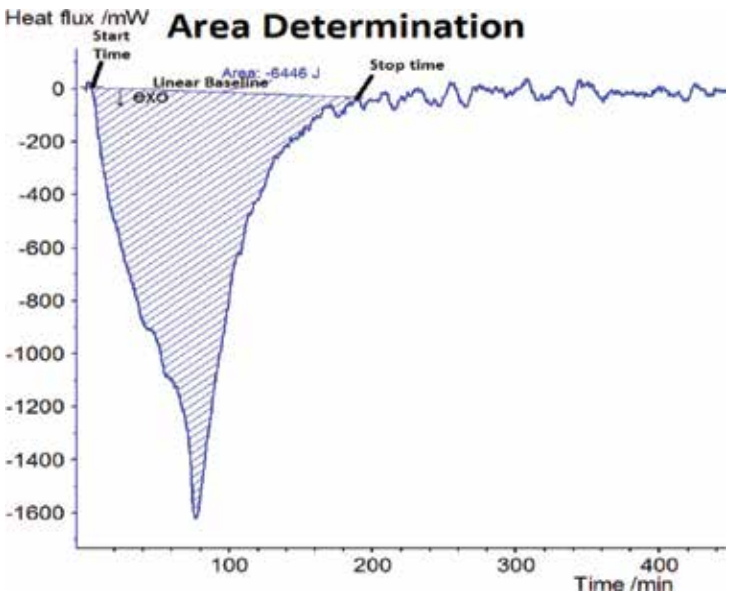

Figure 5. The determination area of the heat flux [29, 31].

The amount of heat generation is determined by the enclosed area by heat flux divided by the of total experiment time (the difference between End time, t_f and Start time, t_s). Within this procedure, average heat generation over the event (charge or discharge) is accomplished [29, 31]. The value is used to determine the total heat loss by the battery cell on the defined operation. The heat generation can be found by Eq. (2):

$$\text{Heat generation} = \frac{\text{Heat Flux} - \text{Area}}{t_f - t_s} \tag{2}$$

The next step is to calculate battery efficiency. It is achieved by determining the absolute power area, i.e., input absorbed power during discharge or extracted output power while in experimental (i.e., charge or discharge) operation. Heat flux area is subtracted from the absolute electrical power area and normalized by the absolute power area to find the battery efficiency. It should be noted that efficiency is given by the difference between electrical input and the loss incurred inside the battery normalized by the electrical input [29, 31]. More specifically, Eq. (3) is used for determining the efficiency:

$$\eta = \frac{\text{Absolute Power Area} - \text{Heat Flux Area}}{\text{Absolute Power Area}} \tag{3}$$

3.3. Evaluation of the measurement

Data analysis from the measured calorimetric data has multiple facets and approaches, encompassing diverse techniques under a variety of names in battery domain. The crucial point is to distinguish between real effects coming from the battery sample itself and artifacts produced

http://dx.doi.org/10.5772/intechopen.75896

Attribute	Test at 0°C				Test at 25°C			
	Discharge	Charge	Discharge	Charge	Discharge	Charge	Discharge	Charge
Heat Generation (mW)	3961.415	1423.189	4005.315	1489.725	1498.498	1069.493	1521.143	1071.65
Total energy Loss (J)	14898.213	10664.569	14810.35	11201.158	6437	4721	6501	4734
Efficiency (%)	88.71	92.85	88.59	92.48	94.25	96.25	94.5	96.01
Maximum temperature increase (°C)	3.9	3.7	2.2	2.04	2.3	2.1	1.9	1.8

Table 4. The complete calorimetric analysis at different temperatures and different operating conditions [29].

by the apparatus or by the environment (temperature and line voltage fluctuations, electronic and computer problems). Real battery sample effects such as transitions and reactions are, as a rule, repeatable, whereas artifacts caused by environmental influences occur almost accidentally. It is helpful to decrease the noise by averaging several measurements; this will improve the signal-to-noise ratio. It should be mentioned that changes in the heat transfer condition between the battery sample and the calorimeter (e.g., by vibrations or bumps of the calorimeter or surroundings) produce peaks in the heat flux signal. The same is true if the battery sample moves inside the calorimeter chamber. The summary of analysis is tabulated in **Table 4**,

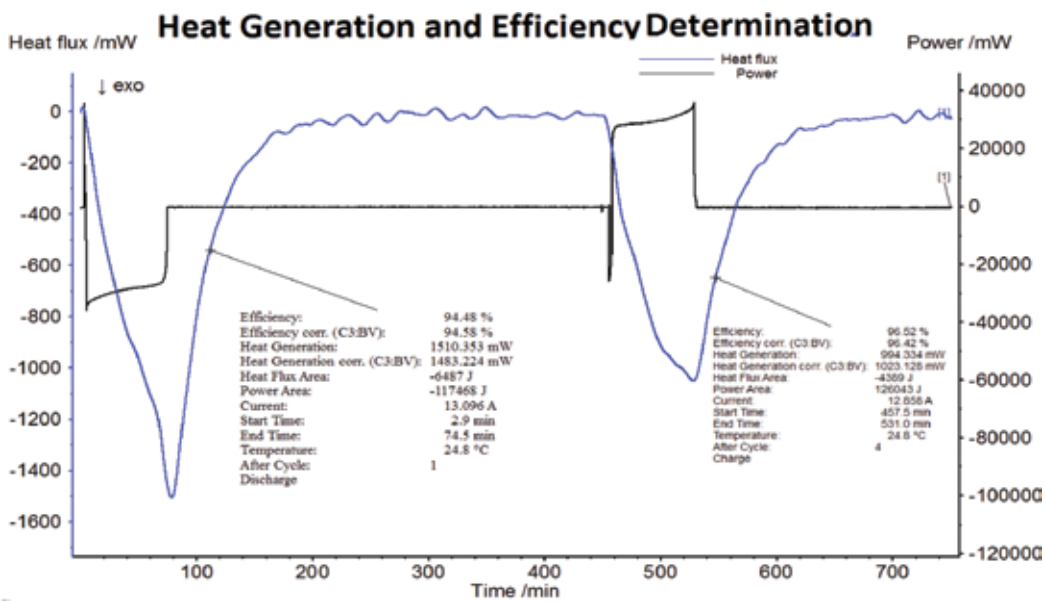

Figure 6. A complete analysis of LTO battery cell heat generation using isothermal calorimeter [29].

and complete analysis is shown in **Figure 6**. To show the variability among the same experiments, two results are presented [29, 31].

The above procedures are repeated at different temperature levels by applying a diverse current charge and discharge pulses. The associated calibration factors for the specific temperatures corresponding to the research are shown in the following **Figure 7**.

The effect of charge-discharge events in different temperature at the different current rate is tabulated in **Table 5**.

The heat flux change level is non-linear. This nonlinear heat flux is responsible for the non-linear change of efficiency in different C-rate in particular. Battery cell efficiency is a key performance indicator. It can assist to choose the best design parameter efficiency among

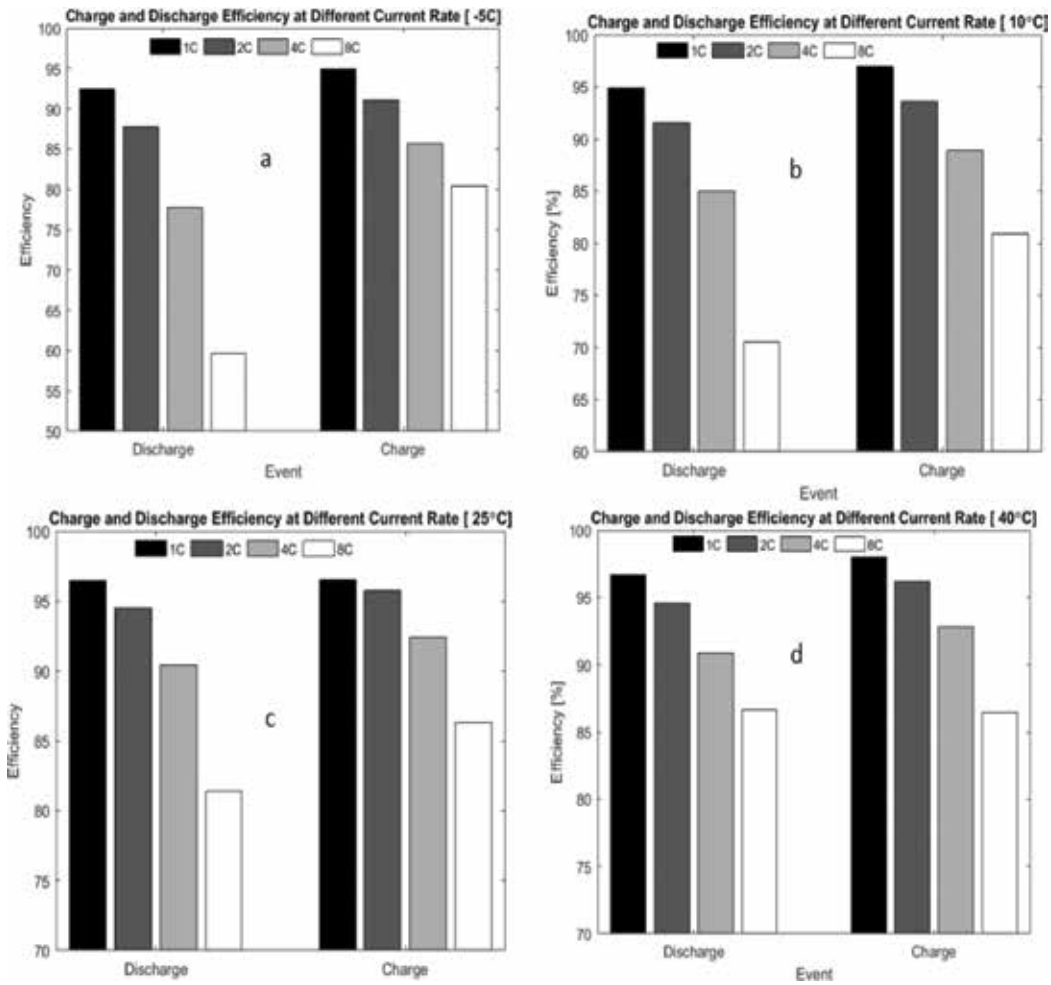

Figure 7. Comparison of charge and discharge efficiency at different temperature: [a] 5°C charge, [b] 10°C discharge, [c] 25°C discharge, and [d] 40°C charge [37, 38].

Temperature	Event	Discharge				Charge			
-5°C	Current Rate	1C	2C	4C	8C	1C	2C	4C	8C
	Heat Generation (mW)	1739	5000	15601	26333	4364	4463	12600	25134
	Total energy Loss (J)	6408	9331	14041	10902	4348	8543	13684	17795
	Efficiency (%)	92.42	87.75	78.26	59.83	95.01	91.23	85.64	79.98
10°C	Heat Generation (mW)	1352	3669	11825	38402	870	3270	10609	25461
	Total energy Loss (J)	5202	7883	12488	16129	2424	6908	11967	20318
	Efficiency (%)	94.82	91.55	85.30	80.86	96.90	93.74	88.89	81.16
25°C	Heat Generation (mW)	939	2666	8066	21427	994.34	2068	3449	18721
	Total energy Loss (J)	4007	5840	9389	15623	5027	5043	8888	16063
	Efficiency (%)	96.42	94.46	90.43	81.45	95.79	92.32	92.43	86.29
40°C	Heat Generation (mW)	839	2510	7192	19148	574	1825	6330	23247
	Total energy Loss (J)	3918	6116	10098	17923	2261	4831	9078	17157
	Efficiency (%)	96.39	94.67	90.77	82.22	97.98	96.12	92.73	86.27

Table 5. Battery calorimetric result summary [37, 38].

different battery cell options. It helps to attain the optimal design of a specific application. This is particularly critical for designing a pack that is made up of the same type of battery cells since a battery user (for instance EV manufacturers) has to buy a bulk amount of batteries for the specific application. Choosing the appropriate battery cell with a right efficiency can aid to avoid different uncertainties for instance: application failure and non-efficient sub-standard performance [29, 31].

4. Model development using calorimeter data

The calorimetric data can be used for battery cell and pack model development—using physical, mathematical relationships to represent logically. As such, the model can facilitate understanding a battery system's behavior without actually testing the system in the real world. A good paradigm is the temperature development inside a battery cell and the heat condition inside an array of battery cells. Useful insights about different decisions in the design could be derived without actually building the system. The model can be used to train personnel using a virtual environment that would otherwise be difficult or expensive to produce the battery thermal management system.

4.1. Cell model

A computationally efficient electro-thermal li-ion model can be developed using the calorimetric data. The model assimilates the main design parameters of the battery cell (sizes, materials, and parameters, etc.) and relevant physics (heat transfer and computational fluid dynamics (CFD)). The battery geometry is generated suitably for further analysis. The numerical problem

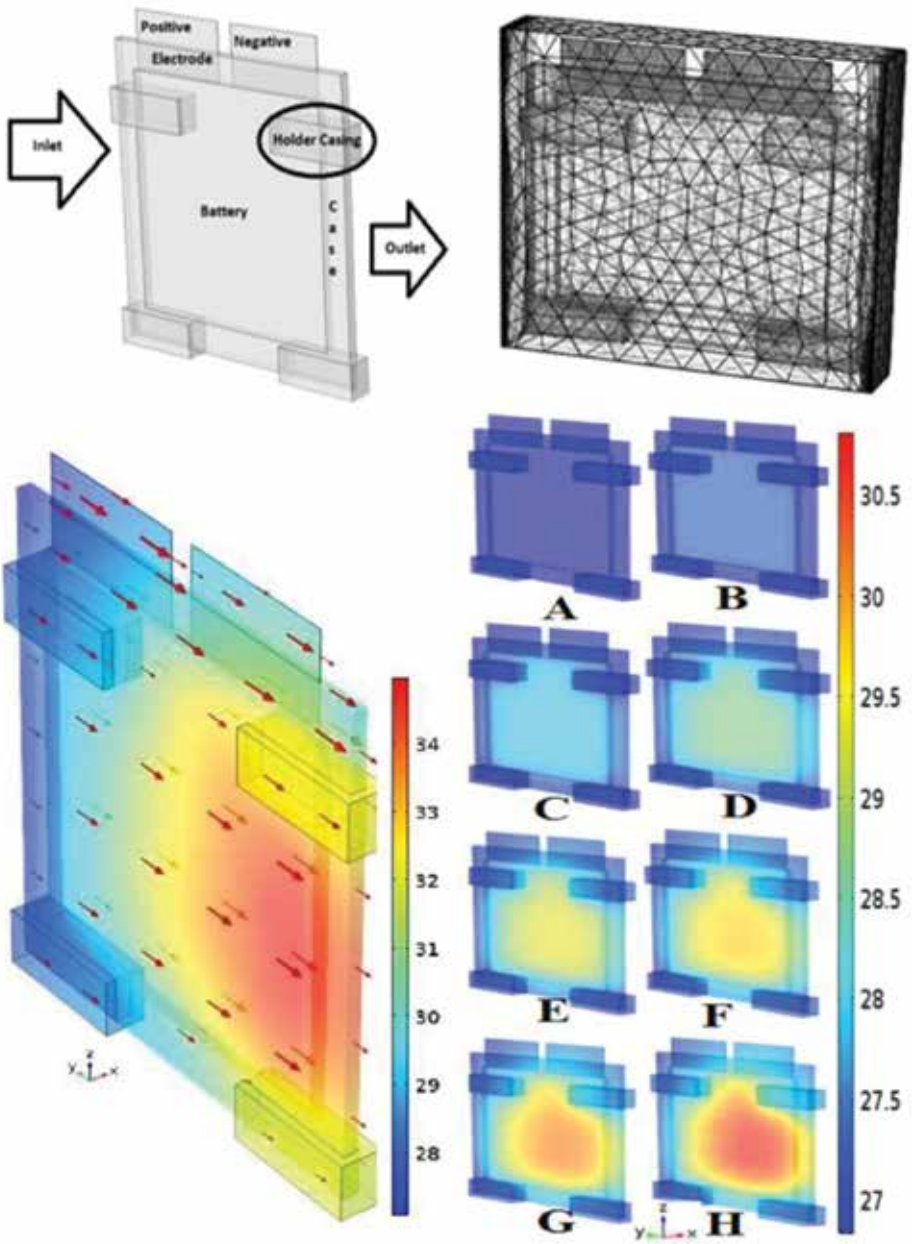

Figure 8. Battery cell modeling using the calorimeter data [39]. Transient simulation results of the battery pack with a cell with 1C discharge with 1m/s air flux and 27°C initial temperature in alphabetic caption order. There is significant temeperature gradient with the time evolution. (A) 0 sec (B) 7 min 30 Sec (C) 15 min (D) 22 min 30 Sec (E) 30 min (F) 37 min 30 Sec (G) 45 min 30 Sec (H) 60 min.

http://dx.doi.org/10.5772/intechopen.75896

of the thermal steady state problem with cooling is solved by considering the heat generation as measured by a calorimeter. The method of cooling is through an air medium. The amount of heat source generation is measured by an isothermal calorimeter. When the battery is functioning, it releases a finite, uniform and constant quantity of heat energy. There is an unhindered circulation of the heat in 3d (longitudinal (x), lateral (y) and normal (z) directions). The outcome of the model simulation is the determination of temperature distribution [39]. The model details are explained in [39] and the results are presented on **Figure 8**.

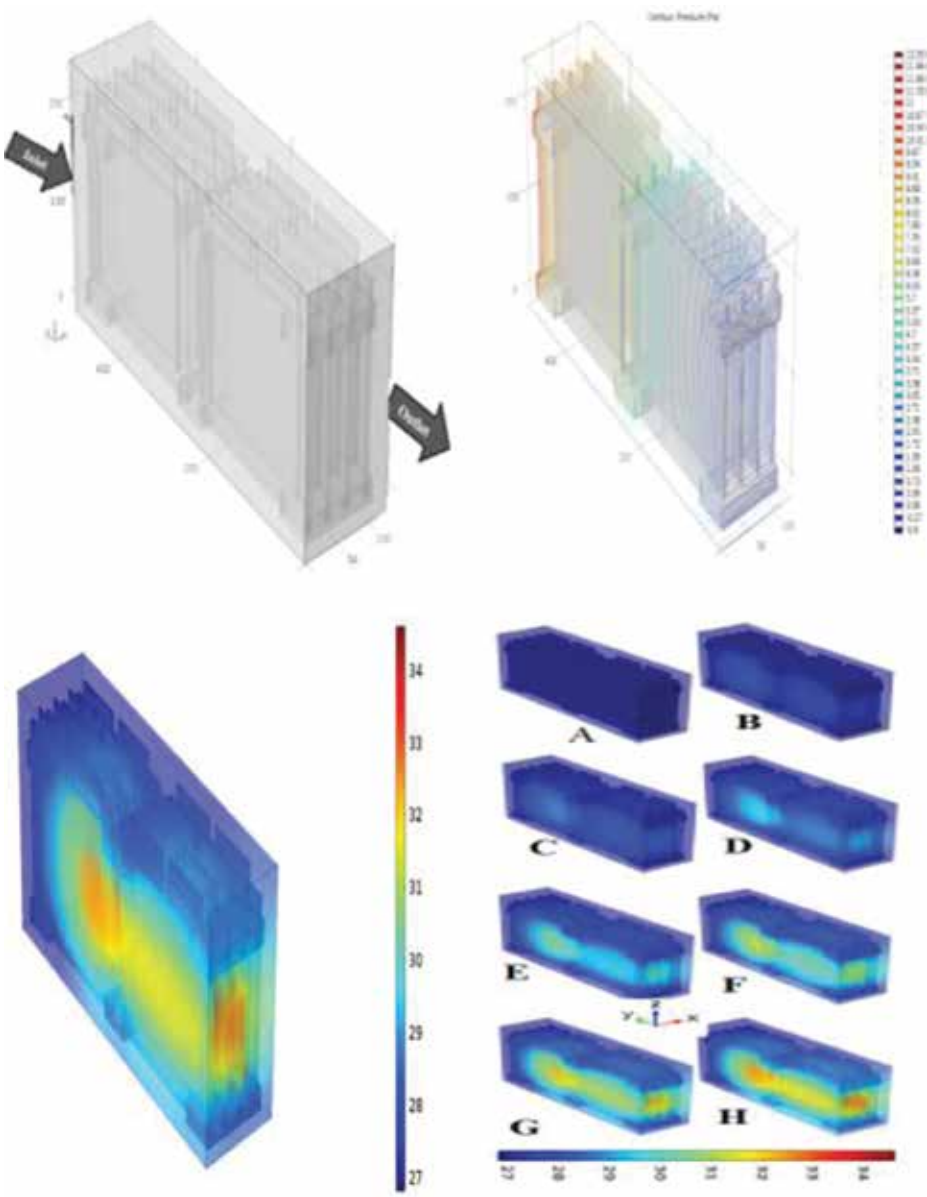

Figure 9. Battery pack model development using calorimeter data [40]. Transient simulation results of the battery pack with a cell with 4C discharge in alphabetic caption order. There is a significant temperature gradient with the time evolution. (A) 0 sec (B) 1 min 52 Sec (C) 3 min 44 Sec (D) 5 min 36 Sec (E) 7 min 28 Sec (F) 9 min 20 Sec (G) 11 min 20 Sec (H) 15 min.

4.2. Pack model

The battery pack made of eight large-size is studied having the 13 Ah nominal capacity. The model integrates the necessary parameters of the battery pack (cell dimensions, configurations, and orientations, associated materials, pack dimensions and configurations) and relevant physics (heat transfer (HT) and (CFD)). The battery cell and pack geometry are analyzed extensively and generated for further investigation using computer-aided design(CAD) tools. The input parameters are provided. The steady state and the time-dependent thermal problem of the battery pack are solved. The numerical solution considers the heat generation in the battery cell. The amount of heat generation is found by an isothermal calorimeter. The battery cells in the pack have direct exposure to cooling medium air. When the battery is operational, it suddenly releases a finite, consistent and constant quantity of heat energy in the homogeneous carrier fluid air. There is an unobstructed propagation of the heat energy in the longitudinal (x), lateral (y) and normal (z) directions. It is combined with the laminar fluid flow of the system to integrate the fluid flow with the current heat transfer phenomena [40]. The effect is the determination of temperature distribution as presented in **Figure 9**. The model details are explained in [40].

5. Conclusions

The calorimetric experiments are used to determine efficiency and heat generation of the battery cell. The key performance indicators (KPI) is found in the battery cell. It is found that the magnitude of heat generation is associated with the corresponding current rate (charge or discharge). This fact is used for thermal modeling. The heat generation in function of battery current rate can be used as input (heat source) of the model. Using the developed methodology, large battery cells can be tested safely and efficiently. The experimental platform has a direct impact on the lifetime profiling of a battery cell. Utilizing the developed methodology, the extensive full lifetime profile of a battery cell (e.g., efficiency, heat generation, temperatures and different state of charge level, etc.) in different lifecycle states, i.e., aging levels (new or old battery cell) can be found. The increasing heat loss is responsible for the decrease in efficiency. The effect of charge-discharge events on heat generation and efficiency has nonlinear effects in different temperature. The experimental technique is a very precise determination to profile the battery cell characteristics. The developed data can be used to predict the thermal behavior of the battery cell and pack by using corresponding cell and pack level.

Author details

Mohammad Rezwan Khan

Address all correspondence to: rezwankhn@gmail.com

Department of Energy Technology, Aalborg University, Aalborg, Denmark

http://dx.doi.org/10.5772/intechopen.75896

References

[1] IEA. Harnessing Variable Renewables: A Guide to the Balancing Challenge. Paris Cedex, France: International Energy Agency (IEA); 2011

[2] Inage S. Modelling Load Shifting Using Electric Vehicles in a Smart Grid Environment. Paris Cedex, France: International Energy Agency (IEA); 2010

[3] EPRI. Electricity Energy Storage Technology Options A White Paper Primer on Applications, Costs, and Benefits, USA: Electric Power Research Institute (EPRI); 2010

[4] Khan M, Swierczynski M, Kær S. Towards an ultimate battery thermal management system: A review. Batteries. 2017;**3**(1):9

[5] Khan MR, Mulder G, Van Mierlo J. An online framework for state of charge determination of battery systems using combined system identification approach. Journal of Power Sources. 2014;**246**:629-641

[6] Khan MR et al. The integration and control of multifunctional stationary PV-battery systems in smart distribution grid. In: EU PVSEC The 28th European Photovoltaic Solar Energy Conference and Exhibition. Paris, Germany: WIP Wirtschaft und Infrastruktur GmbH & Co Planungs KG; 2013

[7] Bandhauer TM, Garimella S, Fuller TF. A critical review of thermal issues in lithium-ion batteries. Journal of the Electrochemical Society. 2011;**158**(3):R1-R25

[8] Culpin B. Thermal runaway in valve-regulated lead-acid cells and the effect of separator structure. Journal of Power Sources. 2004;**133**(1):79-86

[9] Rao ZH, Wang SF. A review of power battery thermal energy management. Renewable & Sustainable Energy Reviews. 2011;**15**(9):4554-4571

[10] Deng F et al. Fault detection and localization method for modular multilevel converters. IEEE Transactions on Power Electronics. 2015;**30**(5):2721-2732

[11] Khan MR, Andreasen SJ, Kær SK. Novel battery thermal management system for greater lifetime ratifying current quality and safety standard. In: Battery Connections. UK, USA: Don Cleary Publishing, Institute of Electrical and Electronics Engineers (IEEE); 2014. pp. 6-10

[12] Khan MR, Nielsen MP, Kær SK. Feasibility study and techno-economic optimization model for battery thermal management system. In: Proceedings of the 55th Conference on Simulation and Modelling (SIMS 55), Modelling, Simulation and Optimization. Aalborg: Linköping University Library; 2014. Sweden

[13] Khan MR et al. Behavior patterns, origin of problems and solutions regarding hysteresis phenomena in complex battery systems. In: Dias JC, editor. Hysteresis: Types, Applications and Behavior Patterns in Complex Systems. Nova Science Publishers; 2014. pp. 215-226

[14] Alaoui C. Solid-state thermal management for lithium-ion EV batteries. IEEE Transactions on Vehicular Technology. 2013;**62**(1):98-107

[15] Newman J et al. Modeling of lithium-ion batteries. Journal of Power Sources. 2003;**119**: 838-843

[16] Committee, SBSS. SAE J 2929 Safety Standard for Electric and Hybrid Vehicle Propulsion Battery Systems Utilizing Lithium-Based Rechargeable Cells. 2013

[17] Kim GH et al. Multi-domain modeling of lithium-ion batteries encompassing multi-physics in varied length scales. Journal of the Electrochemical Society. 2011;**158**(8):A955-A969

[18] Swierczynski M et al. Investigation of multidimensional electrothermal impedance spectroscopy measurement on lithium ion battery cell. ECS Transactions. 2015;**70**(1):305-310

[19] Gi-Heon K, Pesaran A, Spotnitz R. A three-dimensional thermal abuse model for lithium-ion cells. Journal of Power Sources. 2007;**170**(2):476-489

[20] Pesaran AA, Keyser K. Thermal characteristics of selected EV and HEV batteries. In: 16th Annual Battery Conference: Applications and Advances. Long Beach, USA: IEEE; 2001

[21] Hémery C-V et al. Experimental performances of a battery thermal management system using a phase change material. Journal of Power Sources. 2014;**270**:349-358

[22] Yu K et al. Thermal analysis and two-directional air flow thermal management for lithium-ion battery pack. Journal of Power Sources. 2014;**270**:193-200

[23] Downie LE et al. The impact of electrolyte additives determined using isothermal microcalorimetry. ECS Electrochemistry Letters. 2013;**2**(10):A106-A109

[24] Krause LJ, Jensen LD, Dahn JR. Measurement of parasitic reactions in li ion cells by electrochemical calorimetry. Journal of the Electrochemical Society. 2012;**159**(7):A937-A943

[25] Schmidt AP et al. Experiment-driven electrochemical modeling and systematic parameterization for a lithium-ion battery cell. Journal of Power Sources. 2010;**195**(15):5071-5080

[26] Kobayashi Y et al. Precise electrochemical calorimetry of LiCoO2/graphite lithium-ion cell: Understanding thermal behavior and estimation of degradation mechanism. Journal of the Electrochemical Society. 2002;**149**(8):A978-A982

[27] Guldbæk Karlsen L, Villadsen J. Isothermal reaction calorimeters—I. A literature review. Chemical Engineering Science. 1987;**42**(5):1153-1164

[28] Stefan Mathias Sarge GWHH, Hemminger W. Calorimetry: Fundamentals, Instrumentation and Applications. USA: Wiley; 2014

[29] Khan MR, Swierczynski MJ, Kær SK. Determination of the behavior and performance of commercial Li-Ion pouch cells by means of isothermal calorimeter. In: 2016 Eleventh International Conference on Ecological Vehicles and Renewable Energies (EVER), USA: Institute of Electrical and Electronics Engineers (IEEE); 2016

[30] Subramanian VR, Boovaragavan V, Diwakar VD. Toward real-time simulation of physics based lithium-ion battery models. Electrochemical and Solid State Letters. 2007; **10**(11):A255-A260

[31] Khan MR, Kaer SK. Investigation of battery heat generation and key performance indicator efficiency using isothermal calorimeter. In: 2016 IEEE Vehicle Power and Propulsion Conference (VPPC), USA: IEEE; 2016

[32] Pals CR, Newman J. Thermal modeling of the lithium/polymer battery. 2. Temperature profiles in a cell stack. Journal of the Electrochemical Society. 1995;**142**(10):3282-3288

[33] Minassian LT, Milliou F. An isothermal calorimeter with pneumatic compensation-principles and application. Journal of Physics E: Scientific Instruments. 1983;**16**(5):450

[34] Regenass W. Thermoanalytische methoden in der chemischen verfahrensentwicklung. Thermochimica Acta. 1977;**20**(1):65-79

[35] Thomas KE, Newman J. Thermal modeling of porous insertion electrodes. Journal of the Electrochemical Society. 2003;**150**(2):A176-A192

[36] Pals CR, Newman J. Thermal modeling of the lithium/polymer battery. 1. Discharge behavior of a single-cell. Journal of the Electrochemical Society. 1995;**142**(10):3274-3281

[37] Khan MR. Thermal Management of Battery Systems in EV and Smart Grid Application. LAP Lambert Academic Publishing; 2017. p. 84

[38] Khan MR. Thermal management of battery systems in electric vehicle and smart grid application. In: Department of Energy Technology. Aalborg University: Aalborg Universitetsforlag; 2016

[39] Khan MR, Kær SK. Multiphysics based thermal modeling of a pouch lithium-ion battery cell for the development of pack level thermal management system. In: 2016 Eleventh International Conference on Ecological Vehicles and Renewable Energies (EVER), USA: Institute of Electrical and Electronics Engineers (IEEE); 2016

[40] Khan MR, Kaer SK. Three dimensional thermal modeling of li-ion battery pack based on multiphysics and calorimetric measurement. In: 2016 IEEE Vehicle Power and Propulsion Conference (VPPC), USA: Institute of Electrical and Electronics Engineers (IEEE); 2016

Edited by Juan Carlos Moreno-Piraján

Today, calorimetry is considered an art (although some consider it a tool) that studies the energy changes that occur during a change of state. This allows physicochemical analysis to study in detail the thermodynamic systems and to evaluate the different variables that establish the characteristics of the system itself. This book illustrates how the reader can use this technique in a wide spectrum of applications.

Published in London, UK

IntechOpen

ISBN 978-1-83881-294-2
9 781838 812942